Development of Damage Detection Techniques Using Guided Waves for Engineering Materials

By

Jinhang Wu

B.Eng. (Honours)

Thesis submitted in fulfilment of the requirements for the degree of Doctor of Philosophy

The University of Adelaide

Faculty of Science, Engineering and Technology

School of Architecture and Civil Engineering

Abstract

Guided waves (GWs) based damage detection techniques are vital for ensuring structural safety and are extensively applied in aerospace, mechanical, and civil engineering due to their high sensitivity and long-range scanning capabilities. However, two common challenges frequently arise in GWs damage detection for plate structures. The first challenge involves inspecting structural members that contain structural features like weld joints and edges, where defects commonly occur due to high stress concentration. These structural features have complex cross-sections, adding complexity to wave analysis and making damage detection a challenging task.

The second challenge arises from inspecting structural elements made from anisotropic materials, such as timber and composite laminates. GW propagates in anisotropic materials can exhibit complex characteristics and require further investigation. The overarching aim of this thesis is to address these challenges by gaining insights into wave propagation characteristics influenced by irregular structural features such as welded joints and edges, as well as the presence of material anisotropy, as observed in timbers and composite laminates.

The main body of the thesis comprises three journal papers, spanning from Chapter 2 to Chapter 4. Chapter 2 investigates on GW in a steel T-welded joint. A Rayleigh-like feature guided wave (FGW) has been identified propagating along the T-welded joint. This wave exhibits concentrated energy around the joint areas, enabling it to travel extensively along the joint with minimal attenuation. This characteristic makes it potentially valuable for inspecting common weld defects, such as cracks, along T-welded joints. Towards the end of this chapter, the defect's location is predicted using a time-of-flight method.

Chapter 3 and Chapter 4 investigate GWs in anisotropic structural elements, including those with structural features. Chapter 3 investigates the propagation characteristics of GWs in timbers. The targeted damage is internal damages, which can be hardly visible from the timber surface. Both numerical and experimental studies are conducted to explore the interaction between GWs and timber internal damages. Chapter 4 delves into the anisotropy effect of edge waves concentrating at the edges of fiber-reinforced composite laminates. This chapter examines the dispersion relations of these edge waves on composite laminates with different stacking sequences. Numerical results are utilized to compare the displacement fields and mode shapes between the edge waves at the edges of composite laminates and those in isotropic materials. The findings reveal significant disparities in the displacement field and energy concentration of edge waves in comparison to their isotropic counterparts. These identified edge wave modes are then applied to detect edge delamination, using numerical simulations and experimental approaches.

Declaration

I certify that this work contains no material which has been accepted for the award of any other degree or diploma in my name, in any university or other tertiary institution and, to the best of my knowledge and belief, contains no material previously published or written by another person, except where due reference has been made in the text. In addition, I certify that no part of this work will, in the future, be used in a submission in my name, for any other degree or diploma in any university or other tertiary institution without the prior approval of the University of Adelaide and where applicable, any partner institution responsible for the joint award of this degree.

I give permission for the digital version of my thesis to be made available on the web, via the University's digital research repository, the Library Search and also through web search engines, unless permission has been granted by the University to restrict access for a period of time.

I acknowledge the support I have received for my research through the provision of an Australian Government Research Training Program Scholarship.

Signed: Date: 02/11/2023

Acknowledgements

I would like to express my heartfelt thanks to my supervisor, Prof Ching Tai (Alex) Ng, for his guidance throughout my Ph.D. journey. Alex is a patient and friendly supervisor. He always spreads positivity and has greatly enriched my experience working alongside him. Deep appreciation also goes to my co-supervisor, Dr Han Fang, for her unwavering encouragement and support. While a Ph.D. journey culminates in a thesis, the lessons and inspiration imparted by my supervisors will continue to benefit me.

I would like to thank my colleagues Hankai Zhu, Frankie Jiang, Alvin Hu, Tina Yin, Wayne Liang, Juan Allen, Ahmed Aseem for their friendship and fostering a proactive research atmosphere. In particular, I would like to thank Hankai Zhu. He is a man of actions in executing tasks, always punctual and precise; having him as a friend assists me in conquering my procrastination. I would also like to acknowledge Frankie Jiang. His sharp intellect always contributes valuable insights to our research. Furthermore, I would like to acknowledge the support of Mr. Gary Bowman, my laboratory technician.

I would like to thank my parents, Jiehua Lin and Huaming Wu, for their unconditional love and support and great indomitable spirit they have instilled in me. I would also like to thank my partner, Wanyi (Chloe) Li, for nurturing a healthy relationship with me. She is a caring, gifted individual, always full of delightful surprises. I must also acknowledge the wonderful dinners she prepared after my long workday. These relationships are undoubtedly foundational to everything I do.

Lastly, I would like to thank Adelaide Graduate Research School and the University of Adelaide for the financial support during my candidature.

List of Publications

This thesis following peer-reviewed journal paper and unpublished manuscripts are the major outcomes of this research and they form the main body of this thesis.

Journal papers in the main research included in this thesis

1. Wu, J., et al., *Damage detection in the T-welded joint using Rayleigh-like feature guided wave*. NDT & E International, 2023. **135**: p. 102806. https://doi.org/10.1016/j.ndteint.2023.102806

2. Wu, J., C.T. Ng, and H. Fang, *Internal damages detection for structural timber members using low-frequency anti-symmetric guided wave.* Construction and Building Materials, 2022. **322**: p. 126355. https://doi.org/10.1016/j.conbuildmat.2022.126355

3. Wu, J., et al., *Detection of edge delamination in composite laminate using edge wave*. 2023. (Under preparation)

Relevant conference paper in the main research topic excluded in this thesis

4. Wu, J., C.T. Ng, and H. Fang, *Experimental study of the reflection characteristic of the fundamental anti-symmetric Lamb wave from internal defects in structural timber members*. in *ACAM10: 10th Australasian Congress on Applied Mechanics*. 2021. Engineers Australia. p.680-685.

This page is intentionally blank.

Table of Contents

List of Tables

List of Figures

1. Introduction

1.1. Background

Monitoring structural integrity of engineering structures in civil, aerospace, and marine industries has garnered substantial attention in recent decades. Finding effective damage inspection methods is crucial to uphold the integrity of these structures and can provide valuable insights about the damages [1]. This notion has given rise to the concept of Structural Health Monitoring (SHM) [2], typically involving non-destructive testing (NDT) techniques for damage detection. Conventional ultrasonic NDT techniques relied on the bulk wave inspection method, where waves traverse the entire object's bulk, mainly suitable for thick structures [3]. The main drawback of this method lies in its limited coverage, as only areas directly beneath the transducer can be inspected. In contrast, Ultrasonic guided-wave (GW) techniques offer high sensitivity and extensive scanning capabilities compared to conventional bulk waves, making them widely adopted in damage inspection of thin-walled structures.

In many engineering applications, structural features such as welded joints and stiffeners are presented in plate structures. Creating these features often involves additional manufacturing steps, like welding to form joints or adhesive bonding to attach stiffeners to plates. Defects might arise during manufacturing or over the structure's fatigue life. For example, welding processes can introduce defects in the weld metal, fusion zone, or heat-affected zone [4]. Additionally, debonding can occur at the bonded interfaces between stiffeners and attached plates under fatigue loads [5]. Identifying damage in structures containing these features using GWs is crucial yet challenging due to their complex cross-sections. This complexity can pose challenges when calculating the modal properties of GWs in these structures. Another challenge

arises from the fact that the locations of these features are usually difficult to access. For instance, inspecting weld defects along weld lines of a T-weld joint, a common feature in ship hall structures (as shown in **Fig. 1.1**), presents a notable challenge due to limited accessibility. Another prevalent feature in plate structures is the presence of edges. Near-edge defects can occur in some plate structures due to high stress concentrations at the edges under loading, leading to material failures such as edge delamination in composite laminates. Detecting these near-edge damages using GWs can be challenging. The edges of the plate can serve as sources of reflection waves, which might interfere with the scattering waves generated from damages. Consequently, detecting damage on plate structures often requires a large wave propagation area to distinguish scattered waves from the damage and edge reflection waves. However, this task becomes challenging when attempting to detect near-edge damages, as separating these two waves may not be feasible in such cases.

Fig. 1.1. T-welded joints in ship hall structures [6]

Additionally, challenges in damage detection using GWs arise in anisotropic materials such as timber and composite laminates. Timber is a naturally grown and renewable material and is extensively used in infrastructure construction due to its affordability and ease of fabrication [7]. Advancements in GW-based SHM have generated significant interest in applying these techniques to timber members for quality control purposes [8]. Timber

members find applications in various civil constructions: round members are employed in telecommunication and power distribution poles, while sawn members and engineering timber products are utilized as structural beams in house frames, furniture, and flooring, among other uses. Due to broad applications of timber, developing effective damage detection techniques is crucial for maintaining high safety standards. Around $50 million is spent annually on maintenance and assessment fees for timber utility poles to prevent structural failures [9]. The primary challenge in detecting damage in timber using GWs arises from the material's anisotropic, inhomogeneous, and moisture-related behaviour [10], which can make the analysis of wave modes complex. Besides its complexity in material properties, another challenge arises from the wide range of damages that can occur in timbers, such as delamination in timber composites, biological degradation, decay due to high moisture content, and internal cavities due to insect attacks. This diversity in damages complicates the task of generalizing damage detection in timber.

In summary, challenges arise from damage detection using GWs in structural elements with irregular features and in structural elements made from anisotropic materials. The primary objective of this thesis is to address these challenges by gaining insights into wave propagation characteristics influenced by irregular structural features like welded joints and edges, or the presence of material anisotropy as seen in timbers and composite laminates. This involves exploring dispersion relations, modeshapes, and frequency selections tailored to specific needs of damage detection. The study includes a comprehensive examination of existing modes and their sensitivity to detect common damages within these structures. The author hopes that the findings from this thesis can enhance the understanding of GWs in these structures and expand their potential applications in SHM.

1.2. Literature Review

1.2.1. Guided waves in plate structures

GWs are stress waves guided by the boundaries of the structures. Within plate structures, Lamb waves, a category of GWs, consist of two fundamental modes: the fundamental anti-symmetric modes (A_0) and symmetric modes (S_0). A_0 exhibits an anti-symmetric displacement field with respect to the mid-plane, whereas S_0 displays a symmetric displacement field concerning the mid-plane. To minimize the propagating modes, low-frequency fundamental Lamb waves (i.e., below the first-order cut-off frequency) are of great interest in damage detection studies. GW techniques offer broad coverage in scanning areas and rapid inspection and have been widely applied in different materials, including metals [11], concrete [12, 13], composite laminates [14], and timber [15, 16]. In GW-based damage detection techniques, two common sending and receiving approaches are typically employed: pulse-echo and pitch-catch schemes [17]. The pulse-echo approach collects signals reflected from the damage (i.e., echoes), whereas in pitch-catch schemes, the wave signal is obtained from the transmitted side of the damage. The difference between the two schemes is shown in **Fig. 1.2.** Besides onboard sensors such as piezoelectric transducers (PZT), wave signals can also be acquired using a laser acquisition system. Linear GW techniques primarily rely on scattered waves from damage and has been widely applied to structures with regular cross-sections such as plate and cylindrical structures. Typical wave parameters such as wave amplitude, velocity, and phase information are used in signal processing. Depending on the damage type and the excitation frequency, the linear GW method is generally sensitive to the damage sizes comparable to one wavelength of the incident wave, usually around a few millimetres. Scattering studies of GWs have been conducted for different materials [18-20]. Time-domain data

collected in these studies provide insights into the propagation characteristics of GWs and their scattering patterns when interacting with damages.

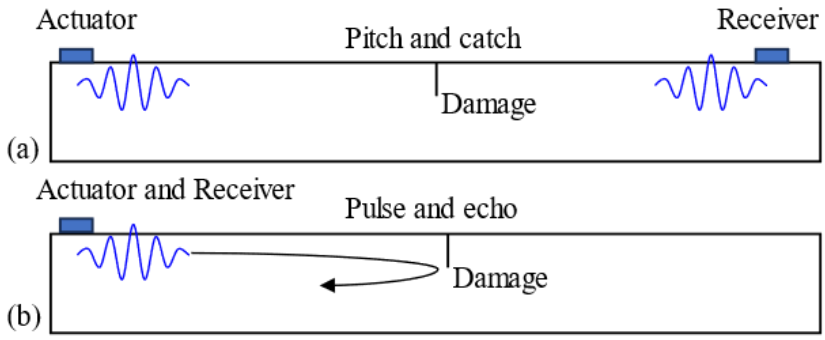

Fig. 1.2. Schematic diagrams of (a) pitch and catch and (b) pulse and echo scheme.

The propagation characteristics of GWs in anisotropic materials such as timbers and composite laminates can exhibit different phenomena compared to those in isotropic materials. This includes directional-dependent phase velocity and steering effects, which are detailed in [3]. Anisotropic materials applied in civil industries often feature unidirectional fiber, as seen in timber and composite laminates. In such cases, the in-plane power flow of plate waves can be influenced by the fiber direction. This phenomenon is demonstrated in an example shown in **Fig. 1.3**. The figure shows the magnitude of power flow density across the thickness of a 1.6mm $[(0/90)_2]_s$ T300/M14 composite laminate for A_0 and S_0 at 300 kHz propagated along 0° direction. The power flow density is a measure of the average power flow per meter. The magnitude of in-plane power flow for S_0 in the 0° laminae is substantially larger than that in the 90° laminae. In contrast, for A_0, little difference in power flow magnitude can be observed across the thickness directions. The propagation characteristics of GWs on composite laminates are investigated, including the scattering directivity pattern of GWs at the damages [19, 21]. Wave phenomena brought

by the contact acoustic nonlinearity effect were employed for delamination detection in composite materials [22, 23].

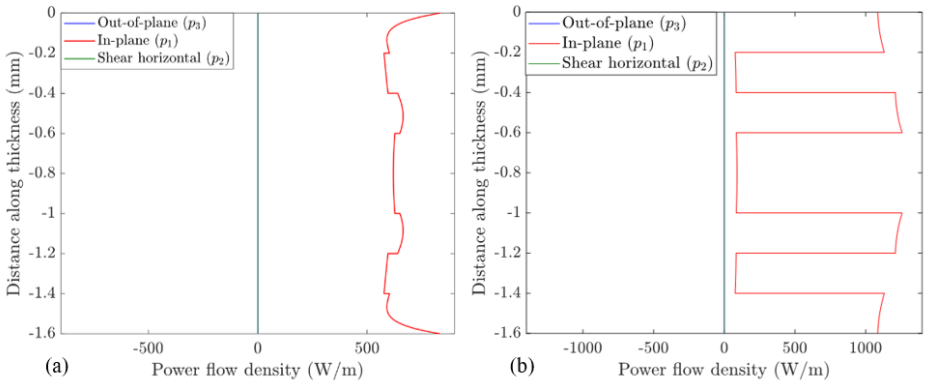

Fig. 1.3. Power flow distribution across the thickness of a 1.6mm $[(0/90)_2]_s$ T300/M14 composite laminate for (a) A_0 mode at 300 kHz and (b) S_0 mode at 300kHz in propagated along 0° direction.

Damage detection in timber using GWs has received comparatively less attention than fiber-reinforced composite materials [6]. Timber composed of cellulosic elements and can contain natural malformations such as annual growth rings, knots, cracks, and holes. These features can complicate wave analysis as they act as sources of wave reflection. Additionally, the elastic properties of timber are directional and moisture-dependent, necessitating additional material parameters for describing wave motions in timber materials compared to isotropic materials. Furthermore, wood properties such as Young's modulus, shear modulus, and attenuation can vary widely across different species [24]. GWs-based techniques applied in timber have been explored in a limited manner. Recent studies have shown that the Lamb wave propagation method has higher sensitivity in detecting the modulus of elasticity under different moisture contents compared to traditional bulk wave methods [25, 26]. GW-based methods have also been combined with machine learning approaches to monitor the mechanical properties of timber [16, 27]. Parameters

such as moisture content, resistance, and deformations ratio are among the most used for monitoring the conditions of timber [8].

1.2.2. Guided waves trapped in structural features

It has been observed that certain structural elements within plate-like structures can function as waveguides, enabling wave modes to propagate along these features [28]. Examples of such features include edges [29], stiffeners [30], weld joints [31, 32], and bends [33, 34]. In the literature, these wave modes are referred to as feature guided waves (FGWs). Typically, these features manifest as changes in thickness (e.g., welded joints, stiffeners) or radius (e.g., bends) within the cross-section of the structures. The creation of these features often necessitates additional manufacturing processes, such as welding to form weld joints or adhesive bonding to attach stiffeners to plates. Defects can emerge either during the manufacturing process or throughout the structure's fatigue life. Welding processes, for instance, can introduce defects in the weld metal, fusion zone, or heat-affected zone [4]. Debonding can take place at the bonded surfaces between the stiffener and the attached plate under fatigue loads [5]. **Fig. 1.4** illustrates schematic diagrams of these structural features, with the inspection areas of interest outlined by dotted lines. Hence, FGWs, with most of their energy concentrating in these specific regions, hold significant importance for non-destructive testing in these structures. The dispersion curves of wave modes within these structures can be calculated using the Semi-Analytical Finite Element (SAFE) method [35]. This method offers solutions that include displacement components in all three directions while applying discretization only to a two-dimensional cross-section. SAFE is commonly integrated with a Perfectly Matched Layer (PML) to simulate an unbounded waveguide [36]. PML functions as absorbing layers and can greatly reduce the model size. The theoretical formulations of the SAFE-PML method can be found in the literatures [35, 36].

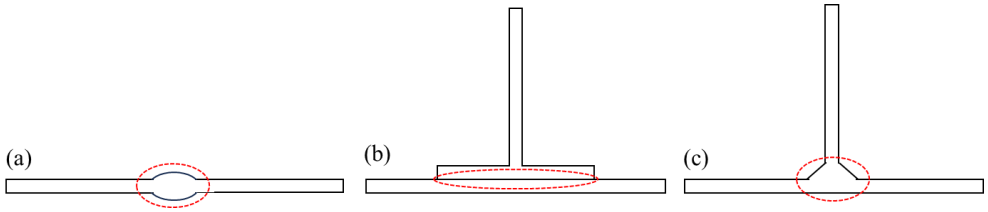

Fig. 1.4. Schematic diagrams of structural features: (a) welded joint, (b) stiffener, and (c) T-welded joint. Red circles represent the interested inspection areas within these structures.

Leaky wave phenomena have been observed in several studies on FGWs [33, 37, 38]. This occurrence can be explained by Snell-Descartes law [39], where feature GWs trapped in structural features can radiate (or leak) waves to the attached plate. The radiating waves in the attached plate must possess a slower phase velocity than that of the FGWs. However, it is worth noting that not all wave modes with slower phase velocities in the attached plate can be launched. For instance, a compression welded guided wave is found to only radiate the fundamental horizontal wave (SH_0) to the plate, while the fundamental anti-symmetric wave (A_0) is not launched [37]. This can be attributed to the displacement field of compression welded guided wave and SH_0 are symmetrical with respect to the mid-plane, while A_0 exhibits the opposite characteristic. The attenuation due to leakage is represented by the imaginary part of the wavenumber solution using the SAFE-PML method, provided that no material damping is considered [33].

1.2.3. Edge waves

Edge waves [40] are a special type of FGWs because they exist at the edges of a plate, rather than within structural features that result from changes in thickness or radius within the cross-section of the structures. They are akin to Rayleigh surface waves, except their propagation is confined by the edges of plates [41]. In isotropic materials, two fundamental edge waves have been

identified: the fundamental symmetric edge mode (ES_0) and the fundamental anti-symmetric mode (EA_0). ES_0, also referred to as extensional edge waves [21], exhibits a displacement field predominantly in the out-of-plane direction, perpendicular to the edges (i.e., shear direction to the plate).

Unlike Lamb waves, which can be generated by a point source and propagate in all directions across a plate, edge waves conserve their energy specifically at the edges. They propagate exclusively along the edges, leading to one-dimensional propagation. Consequently, edge waves can travel long distances with minimal attenuation. They have been effectively utilized in inspecting defects near edges in plate and I-beam structures, demonstrating considerable sensitivity to these defects [29, 42, 43]. Theoretical description of edge waves is derived using 2D plate theories and are further developed to 3D edge waves problem using 3D equations of elasticity [44]. It is widely acknowledged that 3D edge waves theory provides more accurate solutions or the dispersion relations of edge waves in the high-frequency range [45, 46]. Alternatively, SAFE-PML methods are also applied to calculate the dispersion relations of edge waves, see for example in [28]; both fundamental and high-order edge modes are obtained. Additionally, using the SAFE method, important parameters such as the in-plane power flow of a wave mode at specific regions within the cross-section can be calculated. This parameter can be used for filtering out the desired FGWs modes from the rest of the modal solutions. It also aids in comparing the level of energy concentration across different wave modes and frequencies. **Fig. 1.5** shows an example of the edge waves dispersion curve results for a 1.6mm aluminium plate obtained using SAFE methods. Edge waves are plotted using scatter plots, while plate waves are plotted using line plots. The color bar represents the ratio of the power flow in the edge region to the power flow of the entire cross-section. Consequently, the brighter the color, the higher the wave energy concentration at the edge.

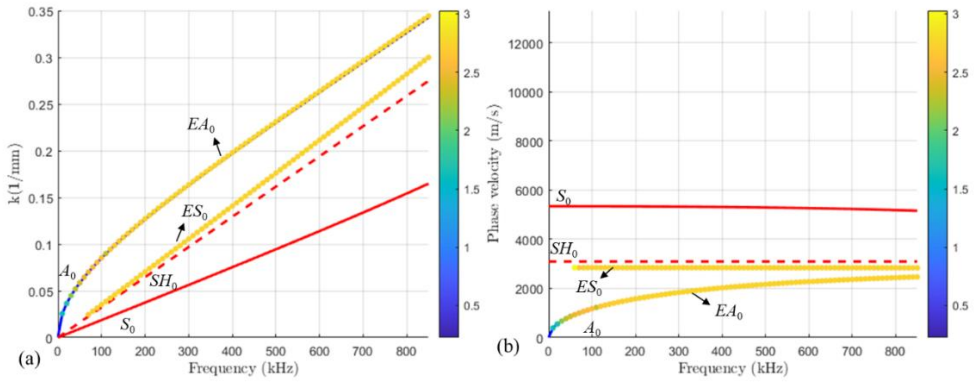

Fig. 1.5. Dispersion curves of edge waves in a 1.6mm aluminium plate; (a) wavenumber plot (b) phase velocity plot.

1.3. Research Aims

The primary objective of this PhD project is to investigate the damage detection capabilities of GWs in structural elements possess irregular structural features and material anisotropy. This involves analysing the modal properties and the propagation characteristics of existing wave modes and their sensitivity to detecting common damages within these elements. The project starts by focusing on FGWs trapped in an isotropic steel T-welded joint. Subsequently, it broadens its focus to FGW in anisotropic materials. Initially, the project investigates GWs in a transversely isotropic structural timber member, specifically exploring the influence of fibres on the propagation of GWs. The project then extends to FGW trapped at the edges of composite laminates. The project's objectives can be outlined as follows:

Objective 1. To detect weld defects in a T-welded joint using GWs

Objective 1.1. To calculate the dispersion curves of a steel T-welded joint using the Semi-analytical finite element (SAFE) method and identify FGW modes.

Objective 1.2. To assess the modal properties of FGWs and determine the modes and frequencies best suited for damage detection purposes.

Objective 1.3. To assess the sensitivity of the selected feature guide wave in detecting weld defects in a T-welded joint, considering different sizes and orientation of the defects, using FE and experimental analysis.

Objective 2. To detect internal damages in a structural timber member using GWs

Objective 2.1. To investigate the dispersion relations of GWs in a structural timber member.

Objective 2.2. To assess propagation characteristics of GWs in timber using FE analysis.

Objective 2.3. To assess the sensitivity of GWs in detecting internal timber damages using FE and experimental analysis.

Objective 3. To detect edge delamination in a composite plate using GWs

Objective 3.1. To identify the existing edge waves in the composite edge using SAFE method.

Objective 3.2. To investigate the modal properties of the existing modes and compared their characterises to edge waves in elastic materials.

Objective 3.3. To compare the sensitivity of the identified edge modes in detecting edge delamination.

Objective 3.4. To provide an experimental study for detecting edge delamination using edge waves.

1.4. Thesis Outlines

Chapter 1 provides an overview of the background and significance of GWs applications in SHM. The chapter emphasizes the advantages of GWs-based techniques and delves into the challenges of detecting damage in structural elements with irregular features. It includes literature reviews on GWs in plate structures, highlighting the key difference of GWs behaviour between anisotropic plates and isotropic plates. Additionally, discussion of wave modes guided by structural features are also provided. Subsequently, the chapter outlines the objectives of the thesis.

Chapter 2 (paper 1) explores the modal properties of wave modes within a steel T-welded joint, a component commonly used in civil and marine industries. The chapter first discusses the method used to derive the dispersion curves of the T-welded joint. A Rayleigh T-welded wave (RTW) is identified as having most of its energy concentrated at the joint region. Subsequently, the chapter investigates the sensitivity of RTW in detecting typical weld defects using numerical and experimental methods. The results indicate that RTW exhibits good sensitivity in detecting weld defects. Moreover, the location of the defect can be accurately predicted based on a time-of-flight method.

Chapter 3 (paper 2) investigates the propagation characteristics of GWs in a structural timber member. The chapter commences with a theoretical background of GWs propagating in transversely isotropic materials. The effects of fiber on the energy concentration of GWs are demonstrated using a three-dimensional (3D) finite element (FE) method. The focus of the damage investigation in this chapter is internal damage, which is hardly visible from the timber surface and poses a significant concern in structural timber, often caused by termites. Both numerical and experimental studies are conducted to explore the interaction between GWs and this internal timber damage.

Chapter 4 (paper 3) builds upon the studies conducted in Chapter 3 and delves into wave modes concentrating at the edges of fiber-reinforced composite laminates. This chapter explores the modal characteristics of edge wave in composite laminates, comparing them with those in isotropic materials. The results reveal substantial disparities in the displacement field and energy concentration of edge waves in comparison to their isotropic counterparts. Similar to the findings in Chapter 3, It is found that the fibre orientation substantially affects the energy concentration of in-plane dominated wave modes but has relatively minor effects on out-of-plane dominated wave modes. The edge modes identified in this chapter are then employed in the detection of edge delamination, through numerical and experimental studies.

Chapter 5 provides the overall summery and contributions made by this thesis and offers recommendations for future studies.

1.5. References

1. Rose, J.L., *A baseline and vision of ultrasonic guided wave inspection potential.* Journal of Pressure Vessel Technology-Transactions of the ASME, 2002. **124**(3): p. 273-282.
2. Raghavan, A., *Guided-wave structural health monitoring*. 2007.

3. Rose, J.L., *Ultrasonic guided waves in solid media*. 2014: Cambridge university press.
4. Wu, J., et al., *Damage detection in the T-welded joint using Rayleigh-like feature guided wave.* NDT & E International, 2023. **135**: p. 102806.
5. Fan, Z., et al., *Feature-guided waves for monitoring adhesive shear modulus in bonded stiffeners.* NDT & E International, 2013. **54**: p. 96-102.
6. Kozak, J. and J. Kowalski, *The influence of manufacturing oversizing on postwelding distortions of the fillet welded joint.* Polish Maritime Research, 2015(4): p. 59-63.
7. Ross, R.J., *Nondestructive evaluation of wood*. Vol. 238. 2015: Government Printing Office.
8. Palma, P. and R. Steiger, *Structural health monitoring of timber structures - Review of available methods and case studies.* Construction and Building Materials, 2020. **248**: p. 118528.
9. Subhani, M., J.C. Li, and B. Samali, *A comparative study of guided wave propagation in timber poles with isotropic and transversely isotropic material models.* Journal of Civil Structural Health Monitoring, 2013. **3**(2): p. 65-79.
10. Dietsch, P., et al., *Methods to determine wood moisture content and their applicability in monitoring concepts.* Journal of Civil Structural Health Monitoring, 2015. **5**(2): p. 115-127.
11. Zhu, H., C.T. Ng, and A. Kotousov, *Low-frequency Lamb wave mixing for fatigue damage evaluation using phase-reversal approach.* Ultrasonics, 2022. **124**: p. 106768.
12. Cao, Y., C.T. Ng, and S.T. Smith, *Debonding detection in FRP-strengthened concrete structures utilising nonlinear Rayleigh wave mixing.* Measurement, 2023. **214**: p. 112736.
13. Aseem, A. and C.T. Ng, *Collinear nonlinear guided wave mixing for debonding detection in reinforced concrete beam using longitudinal and torsional wave modes.* Construction and Building Materials, 2023. **401**: p. 132876.
14. Jiang, C., et al., *Assessment of damage in composites using static component generation of ultrasonic guided waves.* Smart Materials and Structures, 2022. **31**(4): p. 045025.
15. Wu, J., C.T. Ng, and H. Fang, *Internal damages detection for structural timber members using low-frequency anti-symmetric guided wave.* Construction and Building Materials, 2022. **322**: p. 126355.
16. Nasir, V., H. Fathi, and S. Kazemirad, *Combined machine learning–wave propagation approach for monitoring timber mechanical properties under UV aging.* Structural Health Monitoring, 2021: p. 1475921721995987.
17. Su, Z. and L. Ye, *Fundamentals and analysis of lamb waves*, in *Identification of Damage Using Lamb Waves*. 2009, Springer. p. 15-58.

18. Hu, X., C.T. Ng, and A. Kotousov, *Scattering characteristics of quasi-Scholte waves at blind holes in metallic plates with one side exposed to water.* Ndt & E International, 2021. **117**: p. 102379.
19. Hervin, F., L. Maio, and P. Fromme, *Guided wave scattering at a delamination in a quasi-isotropic composite laminate: Experiment and simulation.* Composite Structures, 2021. **275**: p. 114406.
20. Yeung, C. and C.T. Ng, *Time-domain spectral finite element method for analysis of torsional guided waves scattering and mode conversion by cracks in pipes.* Mechanical Systems and Signal Processing, 2019. **128**: p. 305-317.
21. Veidt, M. and C.-T. Ng, *Influence of stacking sequence on scattering characteristics of the fundamental anti-symmetric Lamb wave at through holes in composite laminates.* The Journal of the Acoustical Society of America, 2011. **129**(3): p. 1280-1287.
22. Allen, J.C.P. and C.T. Ng, *Damage detection in composite laminates using nonlinear guided wave mixing.* Composite Structures, 2023. **311**: p. 116805.
23. Soleimanpour, R. and C.-T. Ng, *Locating delaminations in laminated composite beams using nonlinear guided waves.* Engineering Structures, 2017. **131**: p. 207-219.
24. Green, D.W., J.E. Winandy, and D.E. Kretschmann, *Mechanical properties of wood.* Wood handbook: wood as an engineering material. Madison, WI: USDA Forest Service, Forest Products Laboratory, 1999. General technical report FPL; GTR-113: Pages 4.1-4.45, 1999. **113**.
25. Fathi, H., S. Kazemirad, and V. Nasir, *A nondestructive guided wave propagation method for the characterization of moisture-dependent viscoelastic properties of wood materials.* Materials and Structures, 2020. **53**(6): p. 1-14.
26. Fathi, H., S. Kazemirad, and V. Nasir, *Lamb wave propagation method for nondestructive characterization of the elastic properties of wood.* Applied Acoustics. **171**: p. 107565.
27. Fathi, H., V. Nasir, and S. Kazemirad, *Prediction of the mechanical properties of wood using guided wave propagation and machine learning.* Construction and Building Materials, 2020. **262**: p. 120848.
28. Yu, X., R. Qin, and M. Deng, *New insights into topographically feature guided waves (FGW) propagation in non-uniform elastic waveguides.* Wave Motion, 2022. **109**: p. 102866.
29. Zhu, H., C.T. Ng, and A. Kotousov, *Fatigue crack detection in edges of thin-walled structures with corners using the fundamental mode of edge waves.* Ultrasonics, 2023. **132**: p. 106995.
30. Yu, X., et al., *Feature guided wave inspection of bond line defects between a stiffener and a composite plate.* NDT & E International, 2017. **89**: p. 44-55.
31. Lan, Z., et al., *Combined harmonic generation of feature guided waves mixing in a welded joint.* Wave Motion, 2023. **117**: p. 103103.

32. Li, W., et al., *Theoretical and numerical investigations of the nonlinear acoustic response of feature guided waves in a welded joint.* Wave Motion, 2021. **101**: p. 102696.
33. Yu, X., et al., *Shear horizontal feature guided ultrasonic waves in plate structures with 90 transverse bends.* Ultrasonics, 2016. **65**: p. 370-379.
34. Ramdhas, A., et al., *Symmetric low-frequency feature-guided ultrasonic waves in thin plates with transverse bends.* Ultrasonics, 2015. **56**: p. 232-242.
35. Zuo, P., X. Yu, and Z. Fan, *Numerical modeling of embedded solid waveguides using SAFE-PML approach using a commercially available finite element package.* NDT & E International, 2017. **90**: p. 11-23.
36. Zuo, P. and Z. Fan, *SAFE-PML approach for modal study of waveguides with arbitrary cross sections immersed in inviscid fluid.* Journal of Sound and Vibration, 2017. **406**: p. 181-196.
37. Fan, Z. and M.J. Lowe, *Elastic waves guided by a welded joint in a plate.* Proceedings of the Royal Society A: Mathematical, Physical and Engineering Sciences, 2009. **465**(2107): p. 2053-2068.
38. Juluri, N., M. Lowe, and P. Cawley. *The guiding of ultrasound by a welded joint in a plate*. in *AIP Conference Proceedings*. 2007. American Institute of Physics.
39. Postnova, J. and R.V. Craster, *Trapped modes in topographically varying elastic waveguides.* Wave Motion, 2007. **44**(3): p. 205-221.
40. Hughes, J.M., A. Kotousov, and C.-T. Ng, *Generation of higher harmonics with the fundamental edge wave mode.* Applied Physics Letters, 2020. **116**(10).
41. Lawrie, J.B. and J. Kaplunov, *Edge waves and resonance on elastic structures: An overview.* Mathematics and Mechanics of solids, 2012. **17**(1): p. 4-16.
42. Hughes, J.M., et al., *The fundamental ultrasonic edge wave mode: Propagation characteristics and potential for distant damage detection.* Ultrasonics, 2021. **114**: p. 106369.
43. Hughes, J.M., et al., *Damage detection with the fundamental mode of edge waves.* Structural Health Monitoring, 2021. **20**(1): p. 74-83.
44. Feng, F., Z. Shen, and J. Shen, *Edge waves in a 3D plate: Two solutions based on plate mode matching.* Mathematics and Mechanics of Solids, 2017. **22**(11): p. 2065-2074.
45. Krushynska, A., *Flexural edge waves in semi-infinite elastic plates.* Journal of Sound and Vibration, 2011. **330**(9): p. 1964-1976.
46. Zernov, V. and J. Kaplunov, *Three-dimensional edge waves in plates.* Proceedings of the Royal Society A: Mathematical, Physical and Engineering Sciences, 2008. **464**(2090): p. 301-318.

2. Damage Detection in the T-welded Joint using Rayleigh-like Feature Guided Wave

Jinhang Wu [a], Chang Jiang [a,**] ,Han Fang [b], Ching-Tai Ng [a,*]

[a] *School of Architecture and Civil, Environmental, University of Adelaide, Adelaide, South Australia, 5000, Australia*

[b] *School of Civil Engineering, University of Leeds, Leeds, 00000, United Kingdom*

Publication: Wu, J., et al., *Damage detection in the T-welded joint using Rayleigh-like feature guided wave.* NDT & E International, 2023. **135**: p. 102806.

https://doi.org/10.1016/j.ndteint.2023.102806

Statement of Authorship

Title of Paper	Damage detection in the T-welded joint using Rayleigh-like feature guided wave.
Publication Status	☑ Published ☐ Accepted for Publication ☐ Submitted for Publication ☐ Unpublished and Unsubmitted work written in manuscript style
Publication Details	Wu, J., et al., Damage detection in the T-welded joint using Rayleigh-like feature guided wave. NDT & E International, 2023. 135: p. 102806.

Principal Author

Name of Principal Author (Candidate)	Jinhang Wu		
Contribution to the Paper	Conceptualization, Methodology, Writing – original draft.		
Overall percentage (%)	80%		
Certification:	This paper reports on original research I conducted during the period of my Higher Degree by Research candidature and is not subject to any obligations or contractual agreements with a third party that would constrain its inclusion in this thesis. I am the primary author of this paper.		
Signature		Date	20/10/2023

Co-Author Contributions

By signing the Statement of Authorship, each author certifies that:

i. the candidate's stated contribution to the publication is accurate (as detailed above);
ii. permission is granted for the candidate in include the publication in the thesis; and
iii. the sum of all co-author contributions is equal to 100% less the candidate's stated contribution.

Name of Co-Author	Chang Jiang		
Contribution to the Paper	Conceptualization, Methodology, Writing – original draft.		
Signature		Date	10/20/2023

Name of Co-Author	Han fang		
Contribution to the Paper	Supervision, Advising, Writing – review & editing.		
Signature	Han Fang	Date	20/10/2023

Please cut and paste additional co-author panels here as required.

Name of Co-Author	Ching Tai Ng		
Contribution to the Paper	Conceptualization, Supervision, Advising, Writing – review & editing.		
Signature		Date	23/10/2023

Abstract

Steel T-welded joint structures have been largely applied in aerospace and marine infrastructures. The weld length in T-weld joint structures is usually long, and it is difficult to access the weld conditions for damage detection purposes. This is due to the T-welded joint structure possessing a more complex cross-section than the conventional welded plate-like structures. Rather than formed by two plates and joined with a butt weld, the joint regions in the T-welded joint structure are connected to the sides of three plates to form a T-welded joint, and hence cannot be considered as plate-like structures. This makes guided wave modes difficult to be identified and exploited. This paper assesses the feasibility to detect weld defects on a steel T-welded joint structure using the feature guided wave (FGW) technique. FGW technique can provide a fast and long-range inspection for local topographical features, such as welded joints, offering great potential for effective screening of damages. Semi-Analytical Finite Element (SAFE) method is applied to acquire modal solutions in the waveguide. A new algorithm is developed to obtain FGW modes with both high energy concentration and low attenuation from the solutions of SAFE eigenvalue problem. One particular FGW mode with similar mode shape as the Rayleigh surface wave is identified, of which the propagation occurs only in the joint region with small attenuation. This FGW, labelled Rayleigh T-welded wave (RTW), is explored in comprehensive experimental and numerical studies to investigate the propagation and backward scattering characteristics regarding optimal excitation frequency and different sizes of weld defect. The numerical and experimental results are in good agreement. The outcome of the study confirms the capability and robustness of RTW in detecting small weld defects, which allows a long-distance and sensitive screening for the small weld defects at the joint region in the T-welded joint structure.

Keywords:

Feature guided wave, Ultrasound, T-welded joint, Weld inspection, Crack detection

2.1. Introduction

Steel T-welded joint structures, which are usually composed of two steel plates and jointed by welding, have been widely used in aerospace and ship hull structures [1-3]. The "T shape" of the structure is manufactured by placing one vertically oriented plate to the middle of one horizontally oriented plate, where the welding process is conducted at the intersection of the two plates. During the welding process, heat was introduced to the material, which leads to thermal-related mechanisms to the weld and the parent materials such as hot cracking, material shrinkage and distortion of the T-welded joint [1, 2]. Consequently, weld defects are initiated in the weld metal, fusion zone or heat affect zone (HAZ) of the material [3]. On the other hand, welding flaws can also be produced during the process, such as slag inclusions, porosity, under-fill, and a lack of fusion between metals [4, 5]. For example, on a weld with multi-run layers, a lack of fusion can occur between weld layers. These defects can propagate through the material and result in an extensive reduction in fatigue life and structural strength. Thus, identification of early-stage defects in the long T-welded joint region is critical to ensure structural integrity.

Ultrasonic guided wave technique is a non-destructive testing technique allowing a sensitive, fast, and long-range inspection, which has been widely applied to inspect structures with simple waveguides, such as plates and pipes [6-8]. Recent studies showed that some local topographical features in the plate-like structures, such as an increase or decrease of plate thickness [9, 10], bends [11, 12], or a stiffener bonded to the plate [13], feature guided wave (FGW) exists and can propagation in the structure, for which the wave energy can be

trapped in the waveguides. This phenomenon enables most of the wave energy to be retained in the feature waveguide with minimal energy leakage, achieving a long propagation distance inspection. Therefore, if there exists FGWs, such that the energy can be trapped in the T-welded joint region with minimal energy leakage, they can offer great potential for inspecting the weld conditions in a long T-welded joint.

The nature of energy trapping was well explained in past studies [14-16]. For a FGW to exist in a geometry feature, a wave mode with similar mode shapes should exist in the adjacent plates [11]. The similar wave mode that exists in the adjacent plates should also have a higher phase velocity than the FGW at the same frequency, therefore restraining the propagation of FGW in the geometry feature. The modal properties of the propagating wave modes in the waveguide can be obtained by the Semi-analytical finite element (SAFE) method with a Perfectly Matched Layer (PML) modelling technique [17]. Through the modal studies, leaky mode phenomena of FGW were discovered in different waveguides. Shear-type FGW on a butt-weld joint joining two plates was found to be non-leaky due to its phase velocity is the slowest among all wave modes at all frequencies, while the compression-type FGW only becomes non-leaky at the low-frequency range [9, 10, 18, 19]. Similar leakage phenomena were also reported for the FGW in other waveguides, such as bend-guided wave modes [11, 12, 20] or stiffener-guided wave modes [13, 21]. Although non-leaky wave modes are ideal to preserve the most energy in the feature geometry, mode selections are also based on the displacement fields and power flow of the mode for different types of damage detection, and therefore some leaky modes were also found to be attractive candidates in wave scattering studies [4, 9, 19]. Three-dimensional (3D) finite element (FE) models were used to provide a visualization of the propagating wave modes and scattering phenomena at the damages in these studies. These studies confirmed the capability and robustness of detecting defects in plate-like structures with local topographic features using FGWs. Recent studies explored the existence of

FGW in more complex anisotropic materials with local topographical features, such as composite bend plates [22, 23] and composite plates with a stiffener [21]. Yu et al [4] identified different high order FGW families in welded joint and confirmed the feasibility of damage detection using a high order shear type FGW. Li et al [24] conducted a theoretical and numerical investigation on the material nonlinearity effects of FGWs at a welded joint. The results showed the generation of the second harmonic of FGW and also demonstrated the cumulative effect of the nonlinear FGW, which can be used for detecting the early-stage defect.

Limited studies have focused on weld defect detection in T-welded joint structures using FGWs. The existence of FGWs in a welded joint connecting two plates was confirmed by the previous studies [4, 14, 18]. The geometry of weld material was regarded as a local topographical feature, which may constrain the propagation of several FGWs. The same principle can be applied to develop the FGW technique for welded steel T-joints. However, the welding process for T-welded structures was conducted at the corners between the vertical plate and the horizontal plate, which consequently make the weld region of the T-welded structure connect to three long side plates. Therefore, T-welded joint structures have a more complex cross-section and cannot be described as plate-like structures in the sense of searching for FGWs in modal studies. As a result, FGWs at T-welded joint structures are more difficult to be identified and compared to their counterpart wave modes that exist in a plate. Moreover, the vertical plate in the T-welded structure offers an additional leakage direction for the potential FGW trapped in the weld region, which can decrease the likelihood of the occurrence of any trapped wave modes. These factors pose challenges to the development of damage detection techniques for T-welded joint structures using FGW.

The paper aims to explore the feasibility to achieve a fast inspection of weld defects on a steel T-welded joint structure, which is one of the common

structural components in aerospace and ship hull structures. Modal studies are performed to search for possible FGWs using SAFE. A new algorithm is developed to post-process the solutions from eigenvalue problems of SAFE, where wave modes with relatively low energy concentration and high attenuation are filtered out, consequently, only the suitable wave modes are retained. A FGW that has a similar mode shape to the Rayleigh wave, is discovered and selected, which is found to propagate only near the weld region with no energy leakages to the side plates. Therefore, it can greatly constrain its energy at the desired weld region, which enables a long-distance and sensitive screening for small weld defects. The dispersion relations, energy concentrations and mode shapes of the wave modes obtained from SAFE are compared and discussed. The reflectivity of the selected wave from different defects is investigated through a 3D FE model and validated by experimentally measured data. Backwards scattering ratios (BSR) are calculated for different sizes of defects and the time domain signals are also used to estimate the location of the defect using the time-of-flight approach. The findings in this study are beneficial to non-destructive testing techniques developed for T-welded joint structures.

This paper starts with a brief theory of the SAFE-PML method and follows by modal studies performed on a T-welded joint steel plate in Section 2.2. 3D FE models are employed in Section 2.3. An experiment and the measured data are described in Section 2.4. Lastly, a conclusion is given in Section 2.5.

2.2. Theoretical Fundamentals

2.2.1. SAFE-PML method

Unlike one-dimensional structures along which the GW energy is confined in the propagation direction, structures with additional coherent features, such as

welds, bends, and stiffeners can be considered as multi-dimensional structures, in which GWs decay due to beam spreading even without material damping. In such case, GWs travelling in the topographical feature of a structure can be regarded as FGW, which interacts with the irregularly shaped boundaries and results in the concentration of wave energy. The semi-analytical approach can be used to perform dispersive and modal studies for waveguides with irregular cross-sections. The eigenvalue problem is solved by combining the analytical expression along the wave propagation direction and the FE discretization imposed on the cross-section.

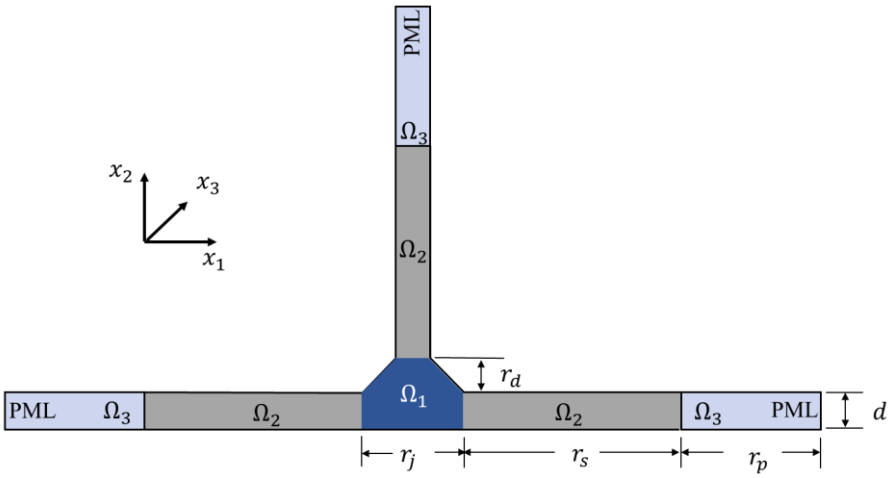

Fig. 2.1. Two-dimensional SAFE model of the T-welded joint steel plate.

Fig. 2.1 shows the two-dimensional model of the T-welded joint steel plate. The desired T-weld trapped region is labelled as Ω_1, three side plates are labelled as Ω_2 and Ω_3. For simulating the infinite exterior domain of the plates at three sides, PML is modelled for each plate, which can absorb waves that propagate away from Ω_1. Assuming the harmonic displacement vector in the waveguide is given by

$$u(x_1, x_2, x_3, t) = U_i(x_1, x_2)e^{I(kx_3-\omega t)}, \qquad (1)$$

where k denotes the complex wavenumber, ω is the angular frequency, and I is the imaginary unit. For general anisotropic materials (stiffness matrix denoted by C_{ikjl}), the motion equation is given by

$$\sum_{j,k,l=1}^{3}\left[C_{ikjl}\frac{\partial^2 u_j}{\partial x_k \partial x_l}\right] + \rho\omega^2 u_i = 0, i = 1,2,3, \qquad (2)$$

By substituting Eq. (1) into Eq. (2), the eigenvalue problem formalism is expressed as

$$C_{ikjl}\frac{\partial^2 u_j}{\partial x_k \partial x_l} + I\left(C_{i_3jk} + C_{ikj_3}\right)\frac{\partial(kU_j)}{\partial x_k} - kC_{i_3j_3}\left(kU_j\right) + \rho\omega^2\delta_{ij}U_j = 0, \quad (3)$$

where δ_{ij} is the Kronecker delta. Commercial FE package can be used to solve Eq. (3), obtaining the wavenumber for each structural frequency, and finally the dispersion curves for the T-welded joint. It should be noted that the elastic stiffness tensor of the material can be complex-valued. For SAFE combined with the PML method, the original wave propagation eigenfunctions in an infinite medium are mapped into exponentially decaying ones in the model with PMLs of finite length[25].

The dimension of the model is defined by the parameters shown in **Fig. 2.1**. In this study, the thickness of the steel plate is $d = 5\text{mm}$, the length is $r_a = 50\text{mm}$, and the length of PMLs is $r_p = 15\text{mm}$. The welded joint area has a thickness r_d = 5mm and a width r_j = 15mm, respectively. The weld surfaces exposed on the sides have an angle of 45 degrees with respect to the horizontal line. The model is meshed using quadratic triangular elements, and finer elements are introduced in the joint area. The mass density of the steel plate is $\rho = 7850\text{kg/m}^3$, Young's modulus is $E = 212\text{GPa}$, and Poisson's ratio is ν=0.3. The eigenvalue problem is solved from 10 kHz to 750kHz with a step

of 10kHz. It should be noted that the obtained wavenumbers at each specified frequency can be complex numbers, of which the imaginary part denotes the attenuation of the corresponding GW mode.

2.2.2. Identification of T-welded joint guided Rayleigh waves

The propagation of desired wave modes should mostly confine to the T-welded joint domain (Ω_1) with as minimal attenuation as possible. Vice versa, wave modes whose energy is not concentrated on Ω_1, such as resonances that exist on the entire cross-section [13], are classified as unwanted wave modes in this study. To filter out unwanted wave modes from the modal solutions, a power flow ratio η is defined to represent the energy concentration coefficient of wave mode.

$$\eta = \frac{P_{\Omega_1}}{P_{\Omega_1+\Omega_2+\Omega_3}}, \quad (4)$$

where P is the axial power flow of a specific GW mode [26].

A new algorithm is developed in this study to post-process the solutions from the eigenvalue problem of SAFE. The new algorithm is performed on all eigenvalue solutions and aims to search for modes with both high energy concentration and low attenuation. Compared to the conventional trace algorithm [24], where baseline inputs are required from plate modes dispersion curves to perform tracing, this algorithm is more suitable for this study. This is due to the cross-section of T-welded structure can no longer be considered as a plate-like structure, and hence wave modes that exist in the T-welded joint may possess large difference in modal properties from those on the plate.

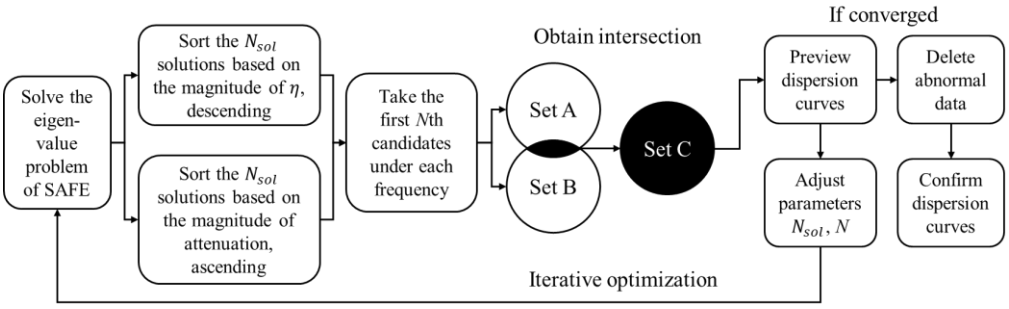

Fig. 2.2. Flowchart of the algorithm used to post-process the solutions from the eigenvalue problem of SAFE.

A flowchart is shown in **Fig. 2.2** to demonstrate the algorithm. The eigenvalue solutions were obtained by solving the eigenvalue problem of SAFE, where the number of solutions is represented by N_{sol}. The N_{sol} were sorted twice in different sequences based on η and attention, correspondingly. Firstly, N_{sol} were sorted in descending order based on the magnitude of η under each frequency. Subsequently, the first Nth solutions under each frequency were extracted to form Set A, which contains the top Nth solutions with the highest η under each frequency. Secondly, the N_{sol} were sorted in ascending order based on the magnitude of attenuation under each frequency. Then, Set B can be obtained by taking the first Nth solutions, which contain the top Nth solutions that have the lowest attenuation under each frequency. The intersection of Set A and Set B is then obtained and labelled as Set C, which represents wave modes with both high energy concentration and low attenuation. A preview of dispersion curves that contain wanted modes can then be plotted using the data of Set C. Iterative optimizations were performed by adjusting the number of N_{sol} and Nth to cover all propagating modes. In the current study, values of N_{sol} and Nth are optimized as 2000 and 150, respectively. Unreasonable data are removed to form the final dispersion curves.

Fig. 2.3 (a) shows the final phase velocity dispersion curves in the T-welded joint structure. As expected, wave modes that propagate on the three

side plates are filtered out due to the small magnitude of η [17, 26]. The modal solutions of SAFE are plotted using scattered points, where the colour bar denotes the normalized ηvalue of the wave mode (cooler colour denotes lower energy concentration in the joint area). The fundamental modes of side plates (5mm steel plate) are also plotted using solid and dash lines for comparison. A FGW mode with a phase velocity of around 3000 m/s has drawn our attention. This mode shows an almost flat phase velocity curve and has dominant ηvalues from the frequency range 460 kHz to 600 kHz among all calculated modes, which is of great interest in T-welded damage detection. Due to these advantages, this mode is selected for damage detection in this study and has been found to have a similar mode shape and phase velocity to the Rayleigh surface wave, as discussed later in this section. Due to its similarity to the Rayleigh surface wave, it is labelled as Rayleigh T-welded wave (RTW) in **Fig. 2.3** (a) and referred to as RTW in this study. The phase velocity of the Rayleigh surface wave on the side plate can be estimated as the intersection regions of S_0, A_0, and SH_0 in **Fig. 2.3** (a). It is shown that RTW has a smaller phase velocity than its counterpart on the side plate. Moreover, RTW exists in a much earlier frequency range, i.e., Rayleigh surface wave starts to appear above 750 kHz in the 5mm side plate, whilst RTW starts to appear at about 460 kHz.

High order FGW modes are also presented in **Fig. 2.3** (a). The excitation of high order modes can be unavoidable in the frequency range of desired RTW. The group velocity, wavenumber, and attenuation of the interested RTW are calculated and shown in **Fig. 2.3** (b) to (d). The phase and group velocity of RTW are both smaller than the fundamental shear horizontal wave (SH_0) in the side plate at the calculated frequency range. **Fig. 2.3** (d) shows the attenuation of RTW is minimal at the calculated frequency range, and the attenuation is increasing from 460 kHz to 600 kHz. In summary, these characteristics confirm that RTW has the potential to propagate a relatively long distance on Ω_1 and is preferably selected for T-welded joint damage inspection.

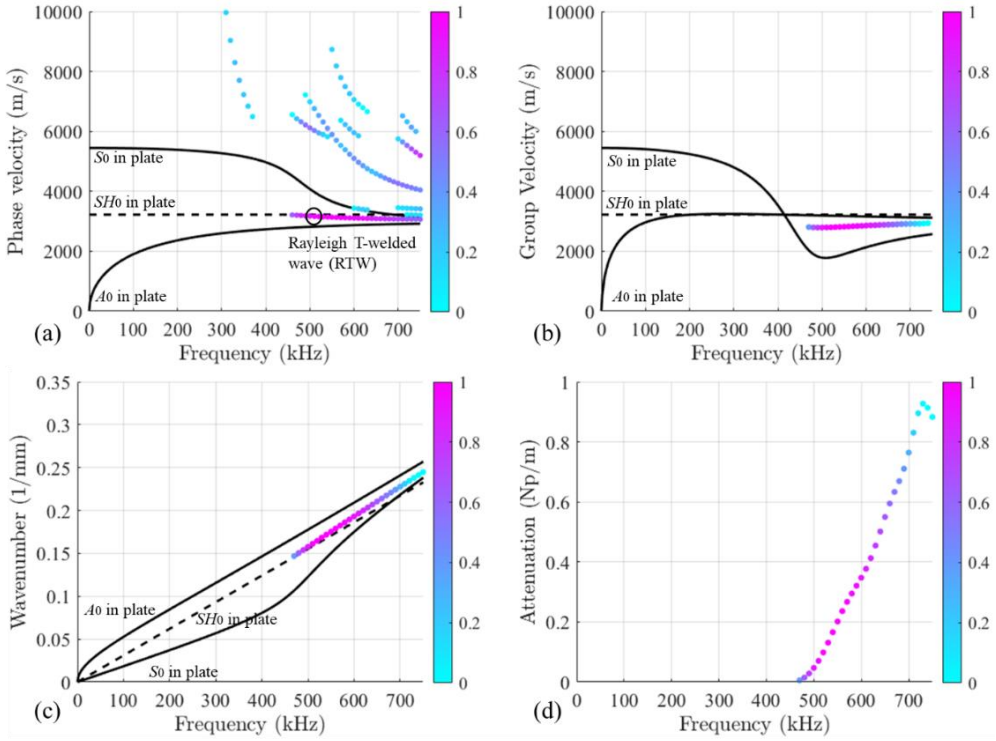

Fig. 2.3. Dispersion curves for a 5mm T-welded joint steel structure (scatter plot: SAFE modal results, line plot: fundamental modes in the 5mm side plate) (a) frequency-phase velocity, (b) frequency-group velocity, (c) frequency-wavenumber, (d) frequency-attenuation. The colour bar represents the normalized ηvalue (cooler colour denotes lower energy concentration in the joint area).

Mode shapes of RTW at f = 460 kHz, 500 kHz, 550 kHz, and 600 kHz are compared, as shown in **Fig. 2.4** and **Fig. 2.5**. The contour plots in **Fig. 2.4** show the axial power flow (P) of RTW whilst the contour plots in **Fig. 2.5** show the axial displacement (u_3) of RTW at these frequencies. Red arrows indicate the sectional displacement (u_1 and u_2) in both figures. It can be seen that axial power flow is confined in the desired trapped domain (Ω_1), with most of the energy concentrated on the fusion weld surfaces exposed at the two sides and surface of the bottom plate, which is quite similar to the Rayleigh surface wave. These two surfaces are labelled to as “side surface” and “bottom surface” in this

study. A considerable amount of energy is also found to concentrate around the weld toe and root area, where a weld toe crack can grow. It is also observed that the energy tends to concentrate more on the side surface when the frequency increased from 460 kHz to 600 kHz. The displacement fields in **Fig. 2.5** show that RTW is dominated by bending and axial motions at the calculated frequencies. In particular, the axial displacement field (u_3) is distributed not only at the surfaces, but also largely around the root of the weld. This indicates the excitation of RTW can be achieved by applying axial displacement on Ω_1.

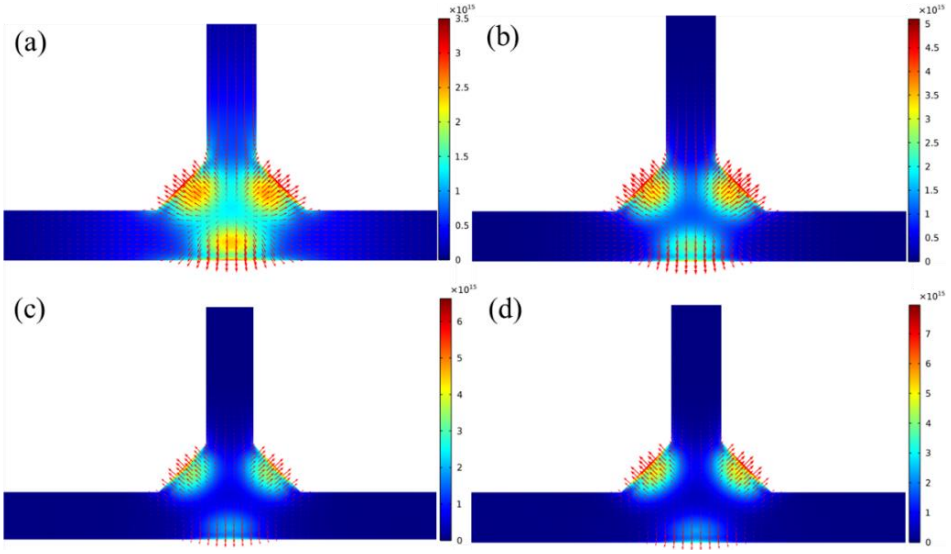

Fig. 2.4. Mode shape of the RTW propagating through T-welded joint at (a) f = 460 kHz, (b) f = 500 kHz, (c) f = 550 kHz, (d) f = 600kHz; Colour bar represents the relative magnitude of axial power flow (P), and red arrow represents the sectional displacements(u_1 and u_2).

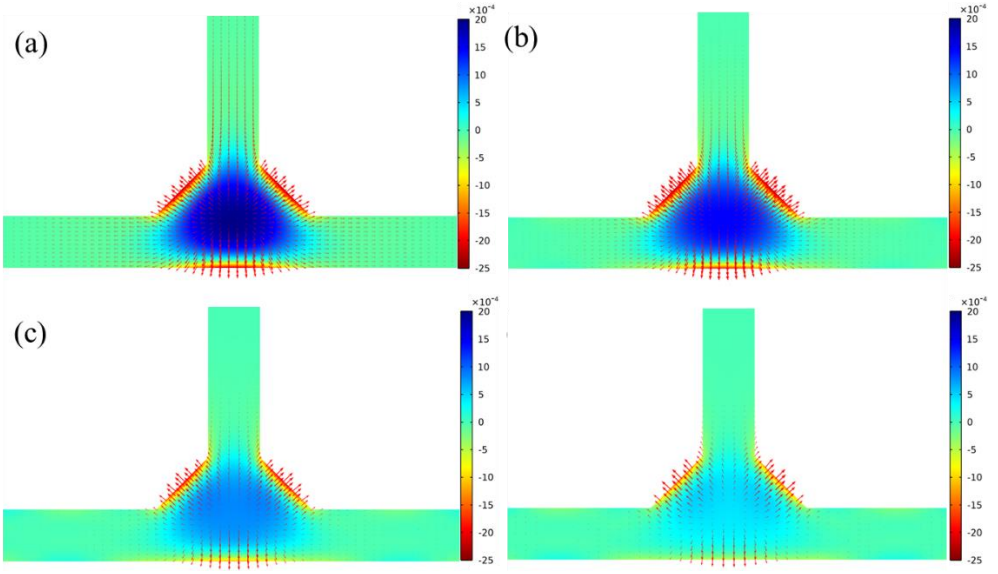

Fig. 2.5. Displacement field of the RTW propagating through T-welded joint at (a) f = 460 kHz, (b) f = 500 kHz, (c) f = 550 kHz, (d) f = 600kHz; Colour bar represents the relative magnitude of axial displacement (u_3), and red arrow represents the sectional displacements (u_1 and u_2).

The distributions of the axial power flow with respect to the midpoint at the side surface and bottom surface are also obtained from SAFE. **Fig. 2.6** (a) shows the locations of the midpoint at the side surface and bottom surface, while **Fig. 2.6** (b) and (c) show the plots of axial power flow at the bottom surface and side surface, respectively. The width of the axial flow can be measured by the full width at half maximum (FWHM), with smaller FWHM indicating higher energy concentration relative to the midpoint [20]. It can also be observed from the results that the energy is much more concentrated with respect to the midpoint for f = 500 kHz to f = 600 kHz compared to f = 460 kHz at both the bottom surface and side surface. Furthermore, **Fig. 2.6** (c) also shows that the energy is concentrated more at the side surface from the bottom surface when the frequency increase from 460 kHz to 600 kHz. In summary, 500 kHz to 600 kHz are preferable compared to 460 kHz due to their ηvalue being much higher. A minor difference is shown in the η value for 500 kHz to

600 kHz. However, the attenuation of 550 kHz and 600 kHz are higher than 500 kHz. To minimize the excitation of other high order modes and maintain high energy concentration at the weld region areas, the excitation frequency is selected as 500kHz in this study for detecting the weld defect.

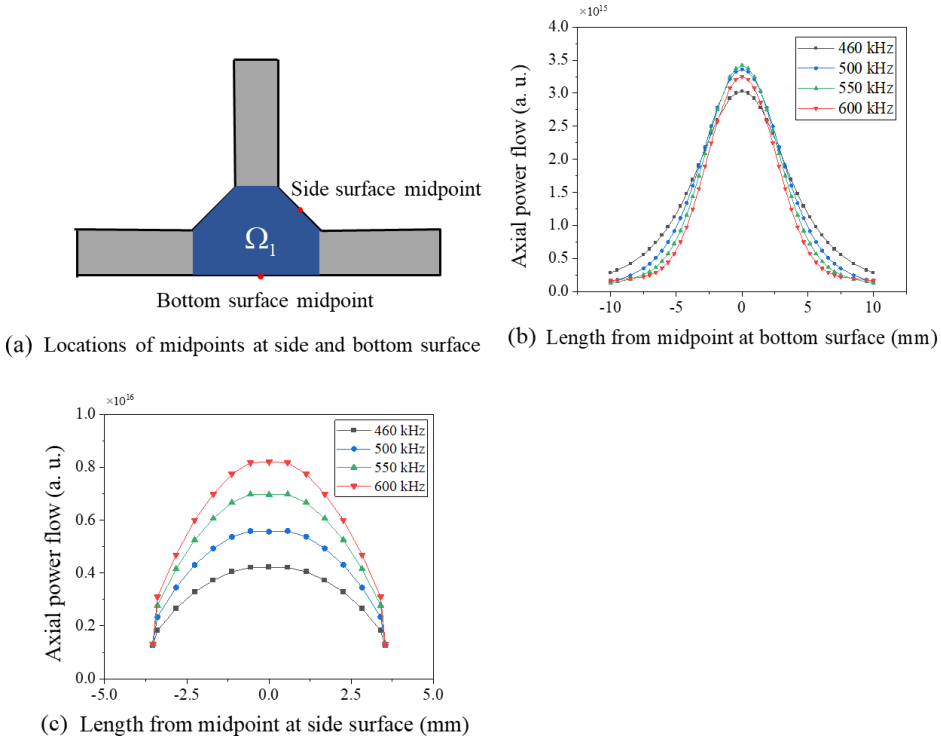

Fig. 2.6. Axial power flow plots of RTW, calculated from SAFE at f = 460 kHz, f = 500 kHz, f = 550 kHz, and f = 600kHz: (a) locations of midpoints, (b) results at bottom surface, (c) results at side surface.

2.3. Numerical Studies

2.3.1. FE model description

To gain a visual understanding of FGW propagation in T-welded joint structure, as well as the scattering interaction with the weld defects, three-dimensional (3D) FE models are developed using the commercially available software

package ABAQUS/Explicit, with a typical model presented in **Fig. 2.7**. The figure shows the dimensions and the cross-section geometry of the specimen which are the same as that used in the SAFE simulation and the experiment. ALID (Absorbing layers with increasing damping) are defined at the three lateral edges of the plates to reduce the unwanted wave reflections. 3D eight-node linear brick element with reduced integration (C3D8R) is utilized to mesh the model. The maximum element size is set to be 0.5 mm to allow at least 20 elements covered by one wavelength distance under the excitation f = 500kHz [6]. Finer mesh is applied to the joint region. The RTW is excited by applying displacements perpendicular to the excitation area, as shown in **Fig. 2.7**. Since the energy of RTW is found to mainly concentrated on the side weld surface and the bottom plate surface in Section 2.2.2, two sets of measurement points are defined at these locations. As can be seen in **Fig. 2.7**, "side surface measurements" are defined as aligned with the midpoint at the side surface, while "bottom surface measurements" are aligned with the midpoint at the bottom plate surface.

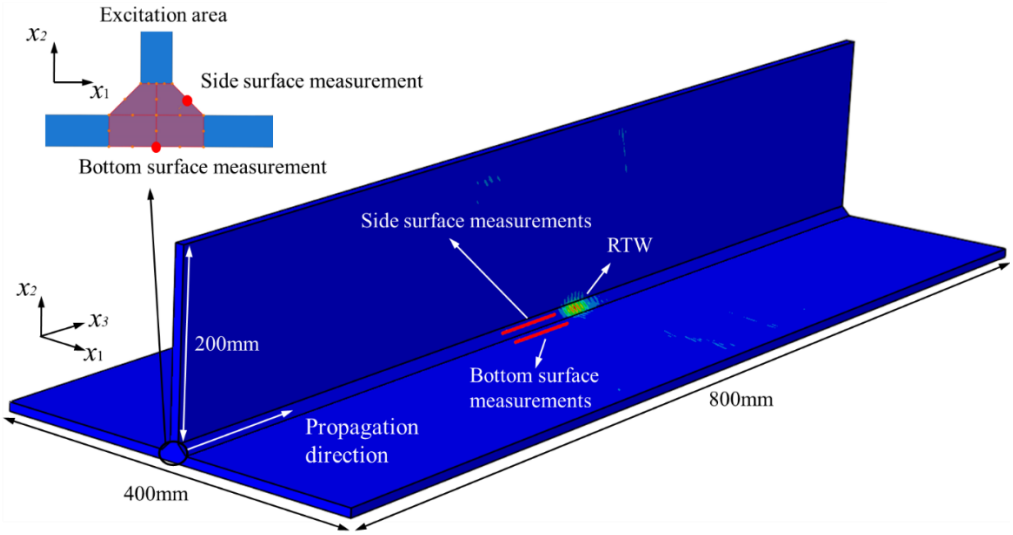

Fig. 2.7. Screenshot of total displacements in the 5mm T-welded specimen with a centre frequency f = 500kHz at 1.81×10^{-4}s after the wave excitation.

2.3.2. Model verification

Fig. 2.7 shows a screenshot at 1.36×10^{-4}s after a narrow-band 500 kHz Hann windowed pulse is excited on the intact sample. It is shown that the energy of RTW at 500 kHz is greatly constrained in the welded joint area, consisting with the predictions by the SAFE method. No leaky modes are observed, revealing that RTW is a non-leaky mode at 500 kHz. Multiple wave modes are excited under an excitation frequency of 500 kHz, however, dispersive modes and modes with little energy concentration to the welded joint area are quickly damped out and absorbed by ALID at the three lateral regions of the horizontal and vertical plates. The group velocity and wavenumber of RTW are measured and validated against the SAFE dispersion curves, as discussed below.

Group velocities are calculated from the data measured from bottom surface measurements in the FE models with frequencies ranging from 460kHz to 600 kHz with a step of 10 kHz, and the results are presented in **Fig. 2.8** (a). The figure presents the FE group velocities results together with the dispersion

curve obtained from SAFE, showing that the FE results agree well with the SAFE result, with errors less than a 5% interval. The wavenumber of the selected frequency f = 500 kHz is validated using a two dimensional (2D) discrete Fourier transform (DFT) method [26]. The number of cycles is set to 30 to have an excellent resolution in the frequency domain. 60 measurement points evenly spaced by 1 mm are defined to measure the out-of-plane displacements at 300 mm away from the excitation areas in x_3 direction at bottom measurements. The time-domain signals are transformed into a frequency-wavenumber contour and are plotted with the dispersion curve calculated from SAFE, as shown in **Fig. 2.8**. (b). It can be observed that the RTW is the only propagating wave at the measurement locations and the wavenumbers of the incident RTW are in line with the SAFE dispersion curves. The 2D-DFT method is also applied to the data measured from side surface measurements and an identical result is obtained.

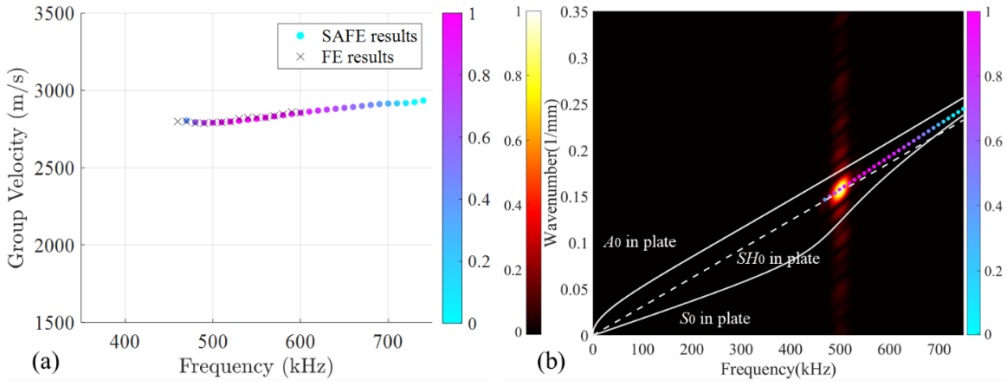

Fig. 2.8. Validation of SAFE dispersion curves for a 5mm T-welded joint steel structure using FE results. The right-hand-side colour bar in both figures denotes the normalized η value (cooler colour denotes lower energy concentration in the joint area). The left-hand-side colour bar in (b) denotes the normalized 2D-DFT magnitude. (a) frequency-group velocity, (b) frequency-Wavenumber contour by 500 kHz incident wave, and the dispersion curves (scatter plot: SAFE results, line: fundamental modes in the 5 mm side plate).

2.3.3. Backwards and forward scattering at weld defect

Upon the validation of the FE models, further analysis is carried out to evaluate the sensitivity of RTW to weld defects using the models. From **Fig. 2.4** and **Fig. 2.5**, it can be seen that the energy of RTW is mostly concentrated on the surfaces. It's expected that RTW is not sensitive to lack of root fusion defects. Thus, this study focuses on surface type defects, such as surface cracks with different orientations. The sensitivity of RTW from different sizes of transverse cracks and axial cracks is investigated under the optimal excitation frequency f = 500 kHz. Furthermore, the location of the transverse crack is estimated using time-of-flight based on the backwards scattering time domain data. The FE results are then compared with the experimental results presented in Section 2.4. Firstly, full-length transverse open cracks are introduced to the model as shown in **Fig. 2.9**. The length of the crack is 7 mm, and the depths are increased from 1 mm to 5 mm with a step of 1 mm to simulate a growing process of crack depth. BSR are calculated for each crack depth case.

The location of the transverse crack is 380 mm away from the excitation source in the x_3 direction and a backwards scattering measurement point is defined at 80 mm before the defect. The number of cycles is set to 15 in order to separate the backwards scattering wave from the incident wave at the measurement location. **Fig. 2.9** (a) shows the contour snapshot of the time step right before the wave reached the transverse crack with 1mm depth. The snapshot shows the RTW is separated from other high order modes and its energy is concentrated on the joint region. **Fig. 2.9** (b) shows the interaction of RTW with the transverse crack, where backwards scattering wave and diffracted wave are generated and propagated in different directions. It is shown that the backwards scattering wave can also constrain its energy around the joint area. **Fig. 2.9** (c) shows the view at the bottom surface at the same time step as in **Fig. 2.9** (b). backwards scattering waves and diffracted waves can also be seen at the bottom surface. It is of interest to compare the magnitude of the

backwards scattering waves recorded at side surface measurement and bottom surface measurement. Therefore, a backwards scattering measurement point located 80 mm before the defect is also defined at the bottom surface to capture the signal.

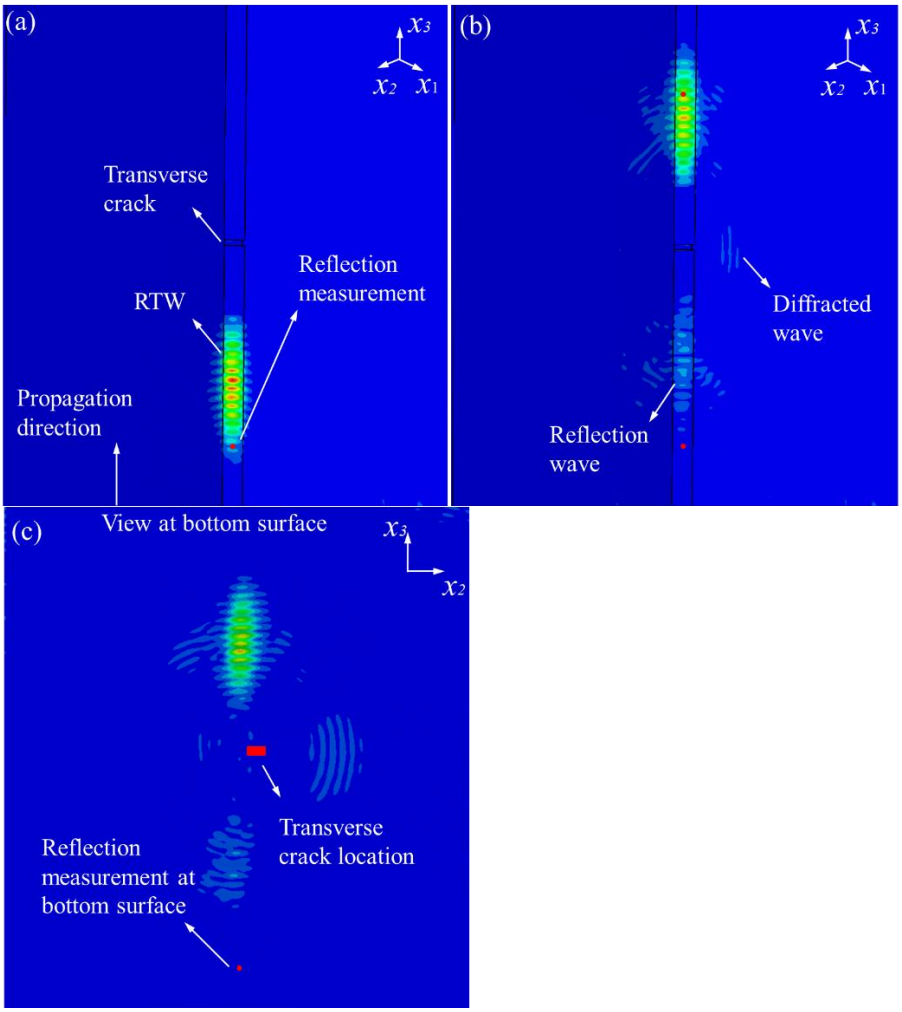

Fig. 2.9. Contour snapshot of total displacements for the 5mm T-welded specimen with a transverse crack on the side weld surface, (a) before RTW approaches the crack, (b) after the interaction of RTW with the crack; (c) view at the bottom surface at the same time step as in (b).

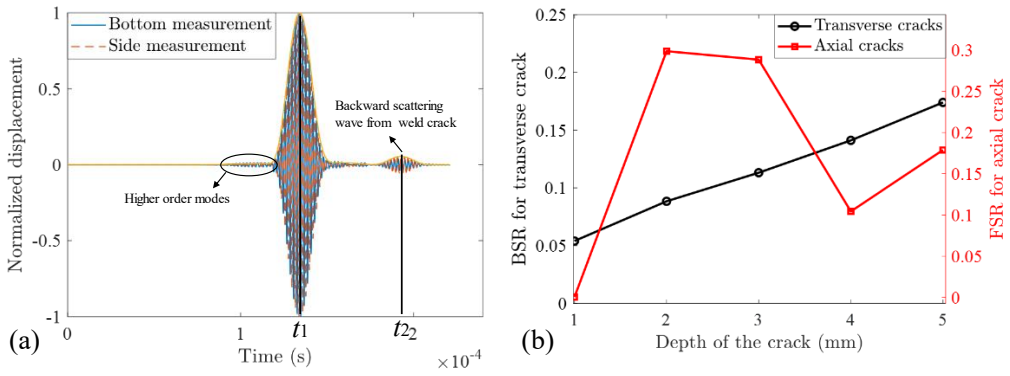

Fig. 2.10. (a) Normalized FE time domain data at the side and bottom surfaces measurement point for the full-length transverse crack with a depth of 1mm. (b) Backwards scattering ratio (BSR) for transverse cracks (plot against the y-axis located on the left) and forward scattering ratio (FSR) for axial cracks located at the weld toe ((plot against the y-axis located on the right).

Fig. 2.10 (a) shows the normalized time signal measured at both side surface measurement and bottom surface measurement for the transverse crack with a depth of 1mm. A small waveform arriving ahead of the RTW can be seen in the figure. This pulse is identified as a higher order mode by confirming the group velocity with the dispersion curve, which is generated from the excitation. It is also shown that this signal is separated from the incident wave and therefore not interfering with the incident wave. The receiving of this waveform is avoidable by moving the measurement location away from the excitation source because it quickly damped out shortly after it passes the measurement point. However, doing so requires increasing in the size of the model, and hence a longer computational time, which is unnecessary in this case. The figure also shows that high order mode has a larger displacement at the bottom measurement compared to the side surface measurement, whilst RTW has a larger displacement at the side surface measurement. (i.e., the amplitude of the backwards scattering wave is larger at the side surface measurement compared to that at the bottom measurement). This is also shown in the mode shapes, where the axial power flow of RTW at 500 kHz is concentrated more at the side

weld surface compared to that at the bottom surface. Therefore, side surface measurement signals are believed to be more sensitive to damage and used to calculate the BSR. The BSR is calculated by the amplitude of the backwards scattering wave divided by the amplitude of the incident wave. Envelopes are generated using Hilbert transform to obtain the amplitudes for both the backwards scattering pulse and incident pulse. The location of the crack can be estimated from the time domain signal using the following equation,

$$ds = \frac{v_{gr}(f_0) \cdot (t_2 - t_1)}{2}, \qquad (5)$$

where ds is the distance of crack away from the backwards scattering measurement point in x_3 direction, $v_{gr}(f_0)$ is the group velocity of the excitation frequency f_0(in this case f_0=500kHz and v_{gr}=2792 m/s). $t_1$and t_2 are the arrival times of peak amplitude of the incident wave and backwards scattering wave, respectively. t_1 and t_2 are 1.34×10^{-4}s and 1.93×10^{-4}s. Therefore, ds can be calculated as 82.4 mm, which gives an accurate estimation of the location of the crack with a 2% error.

The depths of the full-length transverse cracks are then increased from 1mm to 5mm with a step of 1mm. The resultant BSR are shown in **Fig. 2.10** (b), which are plotted against the y-axis on the left. The BSR shows a consistently increasing trend with the depth of the crack. In particular, the BSR of the 1mm depth crack is around 5%, which confirms the sensitivity of RTW. The sensitivity of RTW to axial cracks is also investigated under excitation frequency f_0=500kHz. The axial crack is simulated at the weld toe to represent the typical toe crack that can grow into the root of the weld. FE studies are performed to investigate the effects of the growing depths of the crack on the detection sensitivity of the RTW. The dimension of the axial crack is defined the same as in the transverse crack study: the length of the crack is 7mm, and the depth of the crack is increased from 1mm to 5mm with a step of 1mm in

each case. **Fig. 2.11.** (a) shows a typical contour before RTW approaches a 2mm depth axial crack located at the weld toe, and **Fig. 2.11.** (b) and (c) show the interaction of RTW with the crack. The contours show the energy of the RTW is trapped at the crack when it propagates through the crack. Forward and backwards scattering waves are generated after the interaction of RTW with the crack. It is found that the magnitude of the backwards scattering wave generated from the crack is small in this case due to RTW has bending and axial dominated motions. Instead, the forward scattering wave is found to be more sensitive to the crack due to its magnitude being relatively larger. Therefore, forward scattering ratio (FSR) is calculated and used for comparison between different crack conditions. The FSR is calculated using the following equation,

$$FSR = \frac{EP[T_{dam} - T_{base}]}{EP[T_{base}]}, \qquad (6)$$

where T_{dam} is the time domain data measured at the forward scattering measurement point and T_{base} is the time domain data for an undamaged baseline signal measured at the same location. Function $EP[T_I]$ returns the envelope peak for an input time domain signal T_I, where the Hilbert transform is used to generate the envelope for T_I.

The results are plotted against the crack depth and added using y-axis located on the right in **Fig. 2.10**. (b). In particular, a 2mm depth crack returns a maximum FSR of 0.3. FSR show an overall fluctuation trend with the increasing depths of the damage. The fluctuation of the trend can be explained by the following reasons: 1) As shown in Fig. 11 (c), multiple forward scattering waves are mixed with the incident wave. The mixture of muti-waves can make the FSR difficult to predict. 2) When the defect is deeper, the localized cross-section is compressed. Complex mode conversion can occur such that the mode shape of the propagating wave can be different.

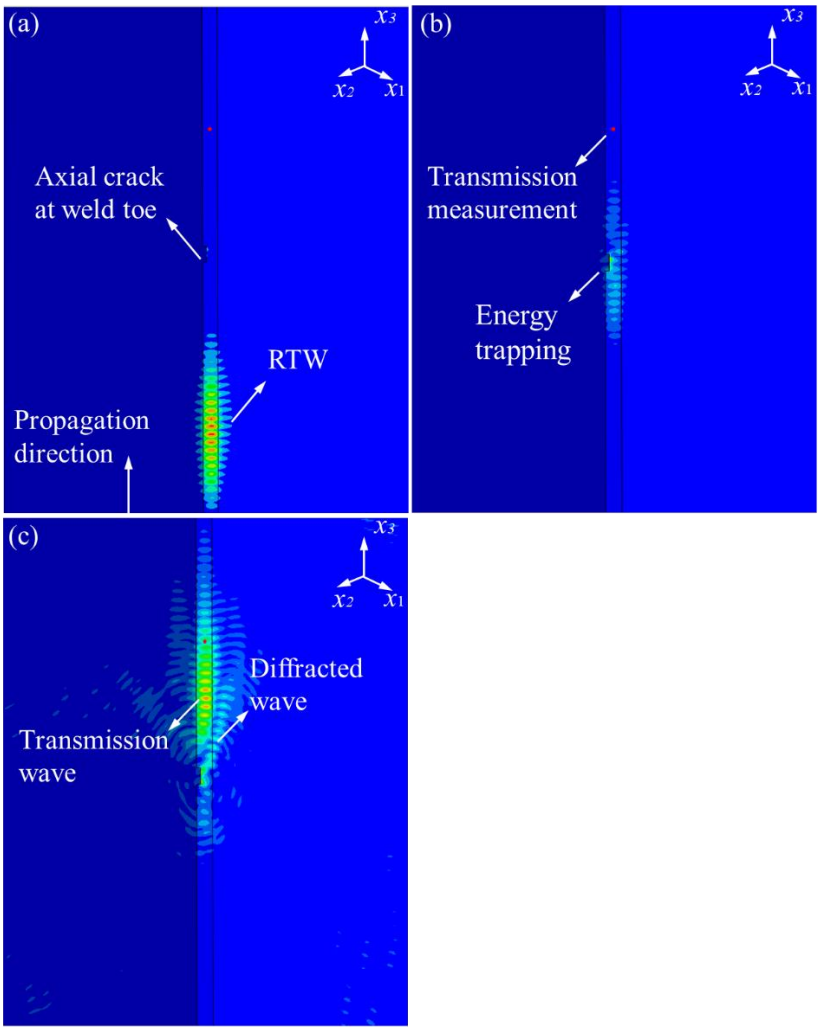

Fig. 2.11. Contour snapshot of total displacements for the 5mm T-welded specimen with an 2mm depth axial crack at the weld toe on the side weld surface, (a) before RTW approaches the crack, (b) interaction of RTW with the crack; (c) after the interaction of RTW with the crack.

2.4. Experiments

2.4.1. Specimen preparation and experimental setup

Fig. 2.12 (a) shows a photograph of the specimen. The circles in the figure indicate the locations of the wave excitation area and the full-length transverse crack. Zoomed view photographs at these locations are shown in **Fig. 2.12** (b) and (c). Two 5mm-thick steel plates (labelled as "Plate 1" and "Plate 2" in **Fig. 2.12** (a) were used to manufacture the specimen, where Plate 1 with the dimension of 400mm × 800mm was welded to the centre line of Plate 2 (800mm × 800mm). The welding used manual metal-arc welding (MMAW) method, which generates an electric arc at the welding point to melt the parent and filler metal [27, 28]. The filler material in the electrode core has the same grade of steel as the parent material. Full penetration butt weld configured in double bevel grooves, was used in the T joint. This welding configuration allows a complete penetration of the filler metal in the joint, achieving a higher connection strength and better corrosion resistance than the fillet weld [27]. The edge of "plate 1" at the welding side is prepared for the full penetration butt weld according to standard AS/NZS 1554.1, and the welding process was conducted in x_3 direction. The weld size at the wave excitation area in **Fig. 2.12** (b) was measured to be 5mm in thickness and the weld surface exposed on the side has an angle of around 45 degrees with respect to a horizontal line, which is the same as that used in the SAFE and FE modelling. The weld surfaces exposed on the side were sanded and polished to remove excess weld material after the welding process. The cross-section geometry, properties of the material, and thickness of the plate are the same as that in the SAFE simulation and in the FE study. Absorbing clay was attached at three ends of the side plate edges to minimize the unwanted reflection waves from the edges. **Fig. 2.12** (c) shows a typical photograph of a full-length transverse crack with 1.3mm depth on the side weld surface. The depth of the crack was increased using a saw blade

to obtain the BSR from the cracks with varying depths, which were demonstrated later in this Section.

Fig. 2.12 (d) shows the experimental setup. The wave was excited by a surface-attached transducer (ULTRAN-GC500) at the top end of the specimen. The diameter of the transducer is 10 mm, which can cover the whole excitation area applied in the FE modelling, therefore duplicating the wave excitation method used in the FE models. The transducer was clamped with the specimen, and vacuum grease（DOW CORNING) was used for coupling between the transducer and the specimen. The signal was generated by a NI PXIE-5122 signal module and the signal voltage was amplified by an amplifier (Ciprian). A Polytech 1D scanning laser Doppler vibrometer was used to measure the out-of-plane displacement of the signal and the data were fed to the acquisition system. The measurement locations are the same as those given in **Fig. 2.7** at both side surface measurements and bottom surface measurements. The specimen in **Fig. 2.12** (d) was rotated at a typical angle to measure the out-of-plane displacements at the side surface measurements using the laser system. A thin layer of reflective painting was evenly sprayed on these surfaces to improve the light reflection level. The sampling frequency was set to be 10.24 MHz with 1000 times samples averaging. A low-pass filter was also applied to improve the signal-to-noise ratio.

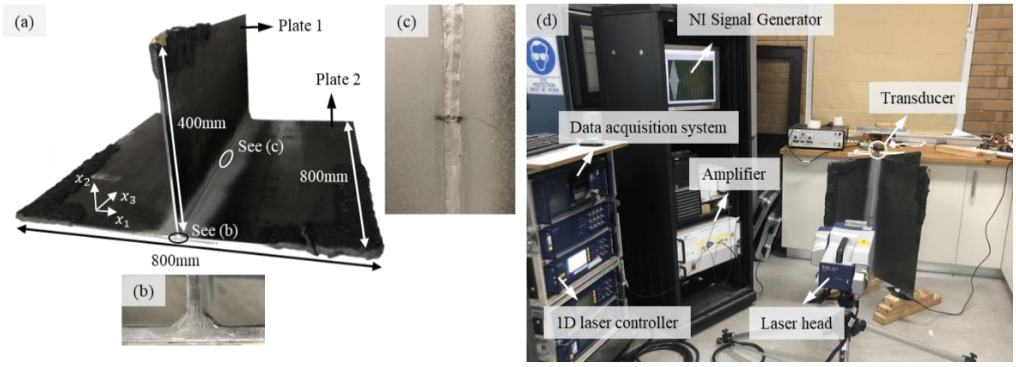

Fig. 2.12. Photographs of (a) the specimen, (b) zoomed view of wave excitation area, (c) zoomed view of full-length transverse crack with 1.3mm depth on the side weld surface, and (d) experimental setup.

2.4.2. Experimental results

Before implementing the damage and conducting backwards scattering studies, wave mode at the selected 500 kHz was validated using the 2D-DFT method. The locations of the measurement points on the side and bottom surfaces were applied consistently as the same as that in the FE models, where the first measurement point is located 300 mm away from the excitation areas in the x_3 direction, allowing the separation of RTW and other modes from excitation. Other excitation modes are expected to be damped out due to their energy is not concentrated on the joint region, leaving RTW to be the only propagating mode at the measurement points. The number of cycles is set to 30 to have an excellent resolution in the frequency domain. **Fig. 2.13** (a) shows typical time domain data measured from side surface measurement and bottom surface measurement at 300 mm away from the excitation areas in x_3 direction. The time domain data on both surfaces indicate RTW is separated from other modes at the measurement locations. Arrivals of high order modes generated from excitation can be seen in the figure, however, their amplitudes are neglectable compared to RTW. The wave amplitude of the side measurement is larger compared to the bottom measurement, which is confirmed by the FE study. **Fig. 2.13** (b) shows the experimental 2D-DFT result measured from side surface measurements. The contour indicates that RTW is the only propagating mode at 500kHz at the measurement locations, and its wavenumber has a good agreement with the SAFE dispersion curve. A small misalignment is shown between the contour and the dispersion curve. The misalignment can be caused by the small difference between the cross-section shape of the specimen and that in the SAFE, especially in the weld region along the propagation path.

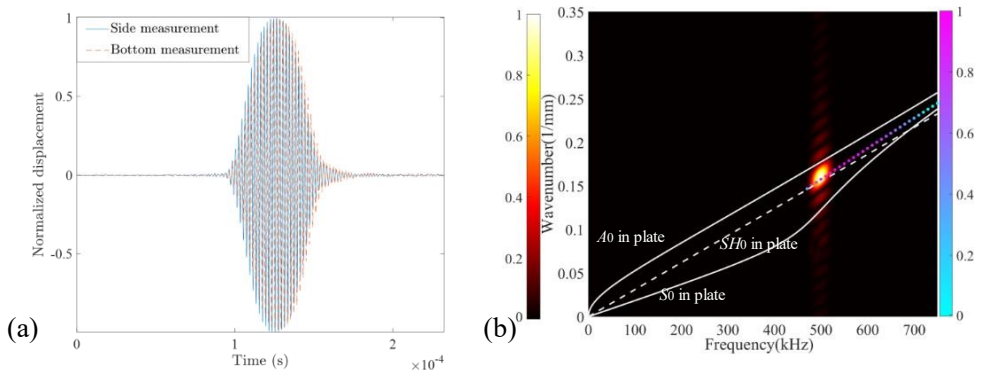

Fig. 2.13. (a) Normalized experimental time domain data at the side and bottom surfaces measurement, and (b) Experimental 2D-DFT contour plot and the SAFE dispersion curve by 500 kHz incident wave.

Attenuations of RTW at f = 460 kHz, 500 kHz, 550 kHz, and 600 kHz were also recorded for the intact specimen. 15 measurement points were evenly spaced from 300 mm to 600 mm away from the excitation source on the side surface measurement. The measurement process was repeated 3 times to reduce instrumentation errors. **Fig. 2.14** shows the attenuation results, where the wave amplitudes were normalized with respect to the amplitude at the first measurement location. The results indicate the attenuation of RTW increases from 460 kHz to 600 kHz, which consists with the SAFE results.

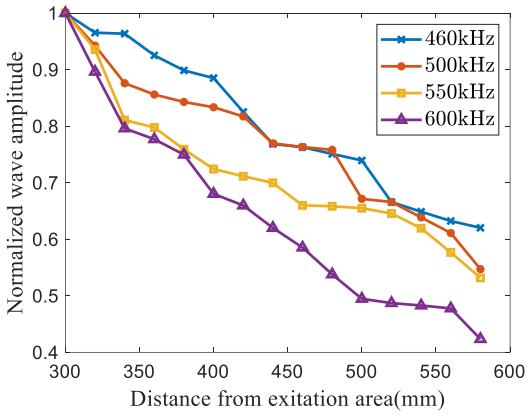

Fig. 2.14. Experimental attenuation results of RTW at different frequencies.

To validate the results from FE modelling, full-length transverse cracks with varying depths were artificially implemented on the specimen. Ideally, identical dimensions of transverse cracks as FE should be implemented in the experiment to validate the FE results. However, it was found that the depth of the crack cannot be implemented with the same depth sizes as those used in the FE modelling due to the instrumental limitation of the saw blade. The resultant depths of the transverse crack were measured to be 1.3 mm, 2.5 mm, 3.2 mm, 3.8 mm, and 4.7 mm. A backwards scattering measurement point was defined at 100 mm ahead of the defect which is also the same as the FE model. The time domain signal was measured at the backwards scattering measurement point for each crack depth case. The measurement process for each crack depth was repeated three times to obtain consistent results by reducing the instrumental errors such as an unstable reflection level of the measuring surface, misalignment of the measuring locations, etc.

Fig. 2.15 (a) shows a typical time domain signal measured for a full-length crack with a depth of 1.3 mm, it is compared with the FE results for a full-length crack with a depth of 1mm. A good agreement is achieved between the two results. A small waveform arrived ahead of the RTW, which is a higher-order mode generated from the excitation. This was well predicted and discussed in the FE Section; thus, it is concluded that the interference from the higher order mode to the incident wave is neglectable due to the amplitude of the higher order mode being small, and it is separated from the incident wave. The figure confirms that FE can closely predict the arrival time and magnitude of the experimental backwards scattering wave. However, a difference in backwards scattering wave magnitude and arrival time between two pulses is also presented, which were due to the following reasons: 1) Group velocity difference can be contributed by the small difference in cross-section shape of weld region in the specimen and the SAFE in along the propagation path. 2) Small misalignment of the damage locations and depth. The location of the defect is then estimated using Eq. (5), resulting in ds= 84.2 mm, which is within

an acceptable 5% error range. BSR is calculated for transverse cracks with varying depths as shown in **Fig. 2.15** (b). Error bars is also plotted to represent the variation in each measurement process for each crack depth. Minor difference is shown due to the instrumental error between each measurement for the same transverse crack. Overall, the BSR of the experimental results shows a consistently increasing trend in agreement with that observed based on the FE results. Typically, the BSR of RTW is around 5% for the crack depth of 1.3 mm, which is approximately 25% of the weld thickness. The BSR results confirmed the sensitivity of RTW in detecting defects close to the surface. The discrepancy between the FE and the experimental results in **Fig. 2.15** (b) can be induced by the following reasons: 1) The width of the defect is about 1.6 mm implemented in the experiment; however, it is defined as 1mm in the FE studies. 2) Mismatches of the depth and shape of the transverse crack. Consequently, this can lead to the possible variance in backwards scattering wave magnitude and phase. On the other hand, the roughness of the weld surfaces can influence the amplitudes the scattering waves. The weld surfaces were polished in this study to minimize wave scattering from local weld waviness. However, when the surface roughness cannot be neglected compared to the wavelength of the excitation wave, the scattering waves from the damage may be polluted by the scattering waves from surface roughness. As a result, small defects might be missed. In this case, baseline data may be required to extract the damage information from the polluted data. It might also be necessary to use a lower frequency RTW with a larger wavelength to balance between the inspection sensitivity and the effects of the surface roughness.

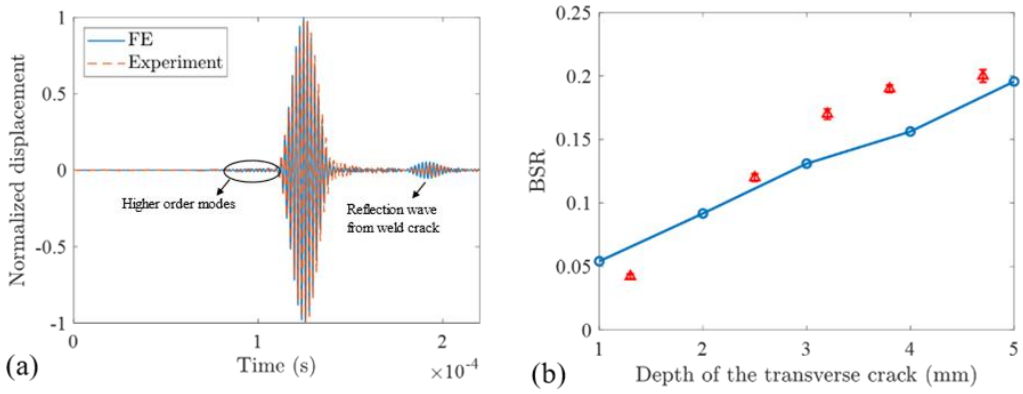

Fig. 2.15. Experimental and FE (a) time signal for a full width crack with a depth of 1.3 mm (experiment) and a 1mm (FE), correspondingly (b) BSR resulting from the full transverse cracks with varying depths by 500 kHz incident wave.

2.5. Conclusions

This study has explored the feasibility to achieve a fast inspection of weld defects on a steel T-welded joint structure. Challenges arose from identifying propagating modes on T-welded joints since the weld region is connected to three side plates, which cannot be considered as the conventional plate-like structure in the modal studies. SAFE-PML method was performed to obtain the modal properties on the waveguide and the criteria for mode selections have been discussed based on a newly proposed algorithm that can automatically detect wave modes with both high energy concentration and low wave attenuations. A FGW mode (labelled RTW) that has a dominant advantage of strong energy concentration at the weld surface with minor attenuation, has been identified and selected in this study. Mode shapes and dispersion curves of RTW at different frequencies were compared and discussed for the feasibility to detect weld defects.

3D FE models were used to evaluate and validate the excitability and propagation of RTW. The models also provide visual concepts of the propagating RTW on the T-welded joint structures under selected frequency and were validated by experimental results. Both experimental and FE results demonstrate that the propagation of RTW can be separated from other multi-modes due to its high energy concentration on the weld joint, resulting in a possible single-mode inspection. The sensitivity of the RTW from different sizes of cracks was also investigated using the BSR both in FE and a validated experiment. The location of the crack along the propagation direction on the weld was estimated based on the backwards scattering time domain signal. This study has confirmed the existence of RTW in the T-welded structure, which exhibits high energy concentration around the weld region and good sensitivity to detect small weld defects in a fast and cost-effective way.

2.6. Acknowledgement

This work was funded by the Australian Research Council (ARC) under grant number DP210103307. The authors are grateful for this support.

2.7. References

1. Nikfam, M., et al., *Experimental and XFEM modelling of high cycle fatigue crack growth in steel welded T-joints.* International journal of mechanical sciences, 2019. **153**: p. 178-193.
2. Kozak, J. and J. Kowalski, *The influence of manufacturing oversizing on postwelding distortions of the fillet welded joint.* Polish Maritime Research, 2015. **22**(4 (88)): p. 59-63.
3. Crupi, V., et al., *Different methods for fatigue assessment of T welded joints used in ship structures.* Journal of ship research, 2007. **51**(02): p. 150-159.
4. Yu, X., et al., *Detection of damage in welded joints using high order feature guided ultrasonic waves.* Mechanical Systems and Signal Processing, 2019. **126**: p. 176-192.

5. Wahab, M. and M. Alam, *The significance of weld imperfections and surface peening on fatigue crack propagation life of butt-welded joints.* Journal of Materials Processing Technology, 2004. **153**: p. 931-937.
6. Zhu, H., C.T. Ng, and A. Kotousov, *Low-frequency Lamb wave mixing for fatigue damage evaluation using phase-reversal approach.* Ultrasonics, 2022: p. 106768.
7. Wu, J., C.T. Ng, and H. Fang, *Internal damages detection for structural timber members using low-frequency anti-symmetric guided wave.* Construction and Building Materials, 2022. **322**: p. 126355.
8. Jiang, C., et al., *Assessment of damage in composites using static component generation of ultrasonic guided waves.* Smart Materials and Structures, 2022. **31**(4): p. 045025.
9. Fan, Z. and M. Lowe, *Interaction of weld-guided waves with defects.* NDT & E International, 2012. **47**: p. 124-133.
10. Fan, Z. and M.J. Lowe, *Elastic waves guided by a welded joint in a plate.* Proceedings of the Royal Society A: Mathematical, Physical and Engineering Sciences, 2009. **465**(2107): p. 2053-2068.
11. Yu, X., et al., *Shear horizontal feature guided ultrasonic waves in plate structures with 90 transverse bends.* Ultrasonics, 2016. **65**: p. 370-379.
12. Ramdhas, A., et al., *Antisymmetric feature-guided ultrasonic waves in thin plates with small radius transverse bends from low-frequency symmetric axial excitation.* The Journal of the Acoustical Society of America, 2013. **134**(3): p. 1886-1898.
13. Fan, Z., et al., *Feature-guided waves for monitoring adhesive shear modulus in bonded stiffeners.* Ndt & E International, 2013. **54**: p. 96-102.
14. Yu, X., R. Qin, and M. Deng, *New insights into topographically feature guided waves (FGW) propagation in non-uniform elastic waveguides.* Wave Motion, 2021: p. 102866.
15. Postnova, J. and R.V. Craster, *Trapped modes in topographically varying elastic waveguides.* Wave Motion, 2007. **44**(3): p. 205-221.
16. Gridin, D., R.V. Craster, and A.T. Adamou, *Trapped modes in curved elastic plates.* Proceedings of the Royal Society A: Mathematical, Physical and Engineering Sciences, 2005. **461**(2056): p. 1181-1197.
17. Zuo, P., X. Yu, and Z. Fan, *Numerical modeling of embedded solid waveguides using SAFE-PML approach using a commercially available finite element package.* NDT & E International, 2017. **90**: p. 11-23.
18. Wang, Y., et al., *Propagation characteristics of ultrasonic weld-guided waves in friction stir welding joint of same material.* Ultrasonics, 2020. **102**: p. 106058.
19. Juluri, N., M. Lowe, and P. Cawley. *The guiding of ultrasound by a welded joint in a plate*. in *AIP Conference Proceedings*. 2007. American Institute of Physics.
20. Ramdhas, A., et al., *Symmetric low-frequency feature-guided ultrasonic waves in thin plates with transverse bends.* Ultrasonics, 2015. **56**: p. 232-242.

21. Yu, X., et al., *Feature guided wave inspection of bond line defects between a stiffener and a composite plate.* NDT & E International, 2017. **89**: p. 44-55.
22. Yu, X., M. Ratassepp, and Z. Fan, *Damage detection in quasi-isotropic composite bends using ultrasonic feature guided waves.* Composites Science and Technology, 2017. **141**: p. 120-129.
23. Yu, X., et al., *Anisotropic effects on ultrasonic guided waves propagation in composite bends.* Ultrasonics, 2016. **72**: p. 95-105.
24. Li, W., et al., *Theoretical and numerical investigations of the nonlinear acoustic response of feature guided waves in a welded joint.* Wave Motion, 2021. **101**: p. 102696.
25. Yu, X., R. Qin, and M. Deng, *New insights into topographically feature guided waves (FGW) propagation in non-uniform elastic waveguides.* Wave Motion, 2022. **109**: p. 102866.
26. Foster, E.A., et al., *Inspection of nuclear assets with limited access using feature guided waves.* NDT & E International, 2022: p. 102695.
27. Taheri, H., et al., *The use of effective full penetration of T-butt welds in welded moment connections.* Welding in the World, 2020. **64**(9): p. 1503-1519.
28. SAA/SNZ, *Structural steel welding – Part 1: Welding of steel structures, AS/NZS 1554.1.* 2014.

3. Internal Damages Detection for Structural Timber Members Using Low-frequency Anti-symmetric Guided Wave

Jinhang Wu, Ching Tai Ng*, Han Fang

School of Civil, Environmental & Mining Engineering, The University of Adelaide, SA 5005, Australia

Publication: Wu, J., C.T. Ng, and H. Fang, *Internal damages detection for structural timber members using low-frequency anti-symmetric guided wave.* Construction and Building Materials, 2022. **322**: p. 126355

https://doi.org/10.1016/j.conbuildmat.2022.126355

Statement of Authorship

Title of Paper	Internal damages detection for structural timber members using low-frequency anti-symmetric guided wave
Publication Status	☑ Published ☐ Accepted for Publication ☐ Submitted for Publication ☐ Unpublished and Unsubmitted work written in manuscript style
Publication Details	Wu, J., C.T. Ng, and H. Fang, Internal damages detection for structural timber members using low-frequency anti-symmetric guided wave. Construction and Building Materials, 2022. 322: p. 126355.

Principal Author

Name of Principal Author (Candidate)			
Contribution to the Paper	Conceptualization, Methodology, Writing – original draft.		
Overall percentage (%)	80%		
Certification:	This paper reports on original research I conducted during the period of my Higher Degree by Research candidature and is not subject to any obligations or contractual agreements with a third party that would constrain its inclusion in this thesis. I am the primary author of this paper.		
Signature		Date	18/09/2023

Co-Author Contributions

By signing the Statement of Authorship, each author certifies that:

i. the candidate's stated contribution to the publication is accurate (as detailed above);
ii. permission is granted for the candidate in include the publication in the thesis; and
iii. the sum of all co-author contributions is equal to 100% less the candidate's stated contribution.

Name of Co-Author	Ching-Tai Ng		
Contribution to the Paper	Conceptualization, Supervision, Writing – review & editing.		
Signature		Date	23/10/2023

Name of Co-Author	Han Fang		
Contribution to the Paper	Supervision, Writing – review & editing		
Signature	Han Fang	Date	20/10/2023

Please cut and paste additional co-author panels here as required.

Abstract

Structural timber is one of the commonly used construction materials. Timber can contain natural internal defect such as knot or natural decay due to its anatomical complexity. Moreover, internal damage or stiffness reduction can also be induced by environmental and biological factors such as weathering and termite attacks. This hidden internal damage increases the difficulty of damage detection using conventional non-destructive testing (NDT) methods. Ultrasonic guided wave (GW) damage detection technique is one of the promising damage detection techniques, which can be employed to achieve an effective and robust damage inspection in timber. However, limited attention has been paid to the use of GW for damage detection in timber, due to the material anisotropy and inhomogeneity. This paper assesses the capability of GW in detecting different sizes of the internal damages in a structural red oak timber using the fundamental anti-symmetric mode (A_0) of GW. Measured GW signals in forward and backward scattering directions are used to calculate the reflection and transmission ratios for different sizes of internal damages. A series of comprehensive experimental and numerical parametric studies are carried out using three-dimensional (3D) finite element (FE) simulations. Good agreement is obtained between numerical and experimental results. The experimentally verified FE model is utilized to further investigate the wave reflection and transmission phenomena from different characteristics of internal damages, such as different lengths, widths, thicknesses, and through thickness locations. The outcomes of this study demonstrate the robustness of GW technique in detecting conspicuous internal damages in structural timber. It demonstrates the feasibility of quantitative assessments of internal damage in timber using A_0 GW.

Keywords: Timber; damage assessment; internal defect; Lamb wave; finite element; scattering.

3.1. Introduction

3.1.1. Backgrounds

Timber has been widely utilised in civil construction due to its sustainable and renewable nature [1, 2]. Recent developments in non-destructive testing (NDT) and structural health monitoring (SHM) techniques have enabled a higher standard for damage detection and structural integrity monitoring in structural members made by timber [3-5]. Visual inspection is implemented for timber damage evaluation, but it is incapable of identifying the internal decay or invisible damage [6]. Timber is a natural grow material, it can contain internal defects such as knot, cracks or natural decay. Physical process on either standing trees or onboard timber members can also produce internal defects [6, 7]. Consequently, internal defects usually exist and can affect the structural performance of timber structures. Apart from the natural defects, internal damages can also be induced by working and environmental conditions. This involves cracks generated from the mechanical loadings, interior deterioration from high moisture content (MC) [12] and reduction of bearing capacity from ultraviolet (UV) aging [13]. Moreover, timber structures, especially historical constructions [8], are susceptible to insect attack due to its organic and biomass nature. The internal flaws can be generated by termites and beetles with only small surface entry larvae boreholes, which are hard to be detected by visual inspection [9, 10]. The reduction in timber material for a structural member due to the internal damage can reduce the stiffness of the structure. Mori et al [11] measured and reported a noteworthy diminution in timber Young's modulus and bending strength from artificial holes on timber.

To minimize the risk of failures due to deterioration of structural performance of timber and ensure the structural safety, an effective NDT damage detection method of critical damage at its early-stage is essential. Compared to metallic materials, such as aluminium and steel, mechanical behaviour derivations of timber are more complicated due to its anisotropy,

inhomogeneity and presence of natural defects. Hence, different damage detection techniques for timber have been developed and investigated in the literatures and they are described in the following sections.

3.1.2. Traditional timber damage detection methods

Traditional semi-destructive testing (SDT) methods, such as Resistograph [14, 15] measures the resistance or properties variation of a timber section by means of electric drilling. However, destructive testing is prohibited for most of the modern or preserved historical construction. NDT methods allow evaluating the condition of structures without inducing any damages. Traditional timber damage detection methods have acoustic emissions, vibration-based methods, sounding and conventional ultrasonic methods, such as C-Scan. The effectiveness of a damage detection method to detect the damages depends not only its sensitivity to damage, but also the operational feasibility considering the realistic environmental conditions.

Acoustic emissions [16] is a passive monitoring approach, through which the elastic wave is generated by a sudden redistribution of stress from localized damages rather an external excitation source. Consequently, the location of acoustic energy source can be determined. Vibration based method [17, 18] primarily examines dynamic responses, such as modal frequencies and modeshapes of structures to determine changes in global stiffness of structures [19]. This method can detect the existence of large discontinuities or damages in timber members. However, compared to conventional ultrasonic method, vibration-based method is less sensitive to small size of damages and incapable of accurately identifying the location of these small damages [19]. Sounding techniques were utilized to measure the embedded length or examine the heath stage of timber utility pole [20]. However, the sonic wave is usually created by means of by impact hammer and belongs to broadband signal. Compared to narrowband signal, broadband excitation signal has higher attenuation and is more dispersive, which is difficult to analyse the signals. On the other hand, the

conventional ultrasonic method, such as C-Scan, was also commonly used for damage detection of structural timbers [21]. This method relies on ultrasonic device to generate bulk wave, which was used in detecting small holes [22, 23] and delamination [24] in timber. In the literature, different studies showed it has adequate sensitivity to the damages. However, conventional bulk wave method has limited inspection area: only a small scanning area covered by the ultrasonic device can be inspected. In summary, these techniques are incapable to effectively detect relatively small-size damages. Therefore, a robust method to detect early-stage inconspicuous defects in timber is essential.

3.1.3. Damage detection of timber structures using guided wave

Guided wave (GW) technique can provide large area inspection and has high sensitivity to different types of damage; thus it has the potential to fulfil the requirements of damage detection for timber. This technique has been widely applied in concrete, metallic and composites materials in the literature [25, 26]. However, limited attention has been paid on damage detection of timber using GW.

In the literature, most of the studies focused on GW and timber were aimed at identifying properties of timber material. Dahmen et al [27] determined nine anisotropic constants of timber using a method combining GWs and bulk waves. The results showed that the computational cost to include all the timber anisotropies is very high. A number of studies indicate that GW is capable of detecting the changes in material properties brought by the environmental factors such as the changes in MCs [28, 29] and UV aging [13]. Fathi et al [28] recently measured the elastic properties of timber under different MC using GW propagation method. They showed that the elastic properties determined using GW are in good agreement with the results obtained from a three-points-bending test. GW has also been recently used to measure the moisture-dependent viscoelastic properties of timber, such as shear storage, shear loss and loss factor [29]. These studies indicate GW can provide a more accurate

estimation of the material properties under the changes of MC and UV aging compared to the conventional bulk wave methods.

However, there were limited studies focusing on damage detection of timber members using GW. One of the main real applications of GW technique in timber is to measure the embedded length [3, 30] or to assess the health conditions of timber utility poles [20, 31]. Dackermann et al [20] proposed a new method for monitoring the structural health of timber utility poles. The method combines the machine learning algorisms with GW technique using a multi-sensor system. El Najjar et al [3] assessed the embedded length and the damage in the embedded portions of the timber poles using GW propagation method. They concluded that the wave energy leakage to the surrounding soil is minimal. Numerical studies have also been performed to simulate the wave propagation on the timber poles. Studies showed that timber can be assumed as transversely isotropic material in modelling wave propagating on a timber pole [32, 33]. This is because the stiffness in fibre direction is much greater than the stiffness in the other two directions direction [34]. This assumption was proven to be valid when treating the timber pole as one-dimensional (1D) waveguide. Zhang et al [35] also conducted a preliminary study on damage detection of timber using a piezoelectric transducer (PZT). The wavelet packet energy of GW is calculated for cracks with different lengths.

GW technique has the potential to enable a robust damage inspection in timber, however, limited studies were presented in the literature. Past studies were mainly focused on using GW to measure the timber properties, and only few studies focused on timber damage detection. Therefore, development of GW technique in timber damage detection, typically those inconspicuous internal damages from interior deterioration or insect attack, are remained critical. To the best of author's knowledge, limited studies have provided quantitative assessments on internal damages in structural timber.

This paper aims to provide a comprehensive wave scattering analysis on the internal damage in structural timber member using fundamental anti-symmetric mode (A_0) GW. To assess the sensitivity of A_0 GW to the timber internal

damage, different sizes of internal damage have been created experimentally on a structural timber member using a rotary tool. Wave reflection and transmission ratios are obtained before and after the internal damages. In order to have a visual understanding and gain insight into the interaction between the internal damage and the GW, three-dimensional (3D) finite element (FE) simulations are used to model the internal damage. A series of parametric studies using experimentally verified FE model are performed to investigate the wave reflection and transmission ratios by varying the length, width, thickness and location of the internal damages.

The arrangement of the paper is as follows. Section 3.2 presents the theory of GW propagation in the transversely isotropic timber. Section 3.3 describes the details of the 3D FE model. Section 3.4 describes the setup and the procedures in the experiment to create different sizes of internal damages. The reflection and transmission ratios obtained from numerical and experimental results, along with the numerical case studies using the validated FE, are discussed in Section 3.5. The limitations of the present study are discussed in Section 3.6. Finally, a conclusion is provided in Section 3.7.

3.2. Governing Equations for GW Propagating in Transversely Isotropic Material

This section presents the governing equations of the GW propagation in timber. Plane wave assumption is used in the analytical solution. Timber is an orthotropic material with elastic properties being different along three principal axes as shown in **Fig. 3.1**. Fibre direction is labelled as 1 while tangential and radial direction are labelled as 2 and 3, respectively. The propagation direction of the plane wave is defined to be consistent to the fibre direction 1. Due to the presence of unidirectional fibres, elastic modulus presents large differences between fibre direction and radial direction while only minor difference

between radial and tangential direction [32]. Therefore, timber can be assumed to be transversely isotropic material [32, 34].

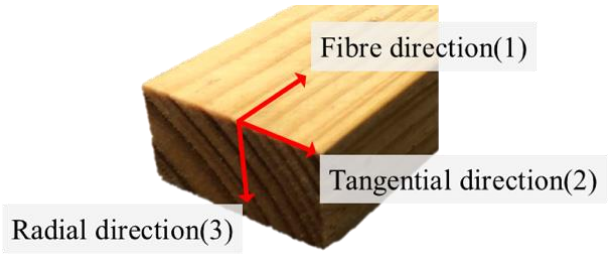

Fig. 3.1. Three principal axes used in the timber modelling

Governing equations for GWs propagating in an orthotropic plate is given in [36]. For plate wave propagation in a transversely isotropic plate, governing equations can be derived by simply substituting the restrictions on elastic constants to the existing solutions. The compliance matrix of transversely isotropic material can by expressed by taking the inverse of the stiffness matrix as shown in Eq. (1a), where ε and σ are strain tensor and stress tensor, respectively. Five independent variables are required to compute the matrix and they are $E_1, E_3, \vartheta_{13}, \vartheta_{23}$ and G_{13}, where E, ϑ and G are young's modulus, Poisson's ratio and shear modulus in the given direction, correspondingly. ϑ_{ij} and ϑ_{ji} are related by $\frac{\vartheta_{ij}}{E_i} = \frac{\vartheta_{ji}}{E_j}$. Due to directions 2 and 3 have the same material elasticity, a symmetric plane is defined for direction 2-3. Therefore, transverse isotropy has $E_2 = E_3$, $\vartheta_{21} = \vartheta_{31}$ and $G_{12} = G_{13}$, which yields the following simplified symmetric matrix.

$$\varepsilon_{kl} = {c_{ijkl}}^{-1}\sigma_{ij} = \begin{vmatrix} \frac{1}{E_1} & -\frac{\vartheta_{13}}{E_1} & -\frac{\vartheta_{13}}{E_1} & 0 & 0 & 0 \\ -\frac{\vartheta_{13}}{E_1} & \frac{1}{E_3} & -\frac{\vartheta_{32}}{E_3} & 0 & 0 & 0 \\ -\frac{\vartheta_{13}}{E_1} & -\frac{\vartheta_{32}}{E_3} & \frac{1}{E_3} & 0 & 0 & 0 \\ 0 & 0 & 0 & \frac{1}{G_{23}} & 0 & 0 \\ 0 & 0 & 0 & 0 & \frac{1}{G_{13}} & 0 \\ 0 & 0 & 0 & 0 & 0 & \frac{1}{G_{13}} \end{vmatrix} \begin{pmatrix} \sigma_{11} \\ \sigma_{22} \\ \sigma_{33} \\ \sigma_{23} \\ \sigma_{13} \\ \sigma_{12} \end{pmatrix}, \qquad i,j,k,l = 1,2,3 \text{ (1a)}$$

$$G_{23} = \frac{E_3}{2(1+\vartheta_{23})} \tag{1b}$$

Substituting the stress-strain relationship in Eq. (1) into equations of motion in Eq. (2), coupled displacement equations in three directions can be obtained and shown in Eq. (3) [36]. The propagation direction of the plane wave is defined to be consistent with the fibre direction 1, whereas direction 3 is the thickness direction of the timber.

$$\frac{\partial \sigma_{ij}}{\partial x_j} = \rho \frac{\partial^2 u_i}{\partial t^2} \tag{2}$$

$$u_j = U_j e^{i\xi(x_1 + \alpha x_3 - ct)}, \qquad j = 1,2,3 \tag{3}$$

where $u_i$is the displacement component and U_j displacement amplitude of u_j. ξ is wavenumber and c is phase velocity. α is an unknown representing the ratio of x_3 to x_1 wavenumbers. Eq. (3) leads to

$$K_{mn}(\alpha)U_n = 0, \quad m,n = 1,2,3 \tag{4}$$

where the coefficient $K_{mn}(\alpha)$ is a symmetric matrix, such that $K_{mn} = K_{nm}$. For the transversely isotropic case, coefficient $K_{mn}(\alpha)$ are:

$$\begin{aligned} K_{11} &= C_{11} - \rho c^2 + C_{55}\alpha^2 \\ K_{22} &= C_{55} - \rho c^2 + C_{44}\alpha^2 \\ K_{33} &= C_{55} - \rho c^2 + C_{33}\alpha^2 \\ K_{23} &= 0 \\ K_{13} &= (C_{13} + C_{55})\alpha \\ K_{12} &= 0 \end{aligned} \tag{5}$$

where contracted notions are defined and used in Eq. (5) to replace c_{ijkl} in Eq. (1a) with C_{ab} following the order of stress tensor index, consequently: 11 = 1, 22 = 2, 33 = 3, 23 = 4, 13 = 5 and 12 = 6. For consistency of the solutions, $C_{11}, C_{33}, C_{44}, C_{55}$ and C_{13} are chosen to express all coefficient. According to Nayfeh et al [36], shear horizontal mode (SH) are uncoupled mathematically from fundamental symmetric mode (S_0) and A_0 if wave propagates along principle axis in a transversely isotropic plate. Equating determinant of Eq. (4) to zero gives a sixth order polynomial [36]:

$$\alpha^6 + B_1\alpha^4 + B_2\alpha^2 + B_3 = 0 \tag{6}$$

where B_1, B_2 and B_3 are coefficients involving material constants and phase velocity. Both coefficients and solution for α are given in Appendix A.

Solve Eq. (6), substitute α into displacement and stress expressions and apply stress free conditions at plate boundaries [36], the characteristic equations for the symmetric and antisymmetric Lamb wave modes propagate along principal axis in a transversely isotropic plate can be obtained as shown in Eqs. (7)-(9). Eq. 7(a) is for symmetric waves while Eq. 7(b) applies to anti-symmetric waves [36].

$$\frac{\tan(\gamma\alpha_1)}{\tan(\gamma\alpha_3)} = \frac{D_{11}D_{23}}{D_{13}D_{21}} \tag{7a}$$

$$\frac{\tan(\gamma\alpha_1)}{\tan(\gamma\alpha_3)} = \frac{D_{13}D_{21}}{D_{11}D_{23}} \tag{7b}$$

$$\gamma = \frac{\xi d}{2} \tag{8}$$

$$\begin{aligned} D_{1k} &= (C_{13} + C_{33}\alpha_k W_k) \\ D_{2k} &= C_{55}(\alpha_k + W_k) \\ W_k &= \frac{\rho c^2 - C_{11} - C_{55}\alpha_k^2}{(C_{13} + C_{55})\alpha_k} \end{aligned} \tag{9}$$

where d is the thickness of the plate and $k = 1,2,3,4,5,6$.The corresponding roots for α are given in Appendix A. Semi-analytical solutions of Eqs. (7)-(9) are shown in Section 3.3.1.

3.3. 3D FE Model

3D FE models were developed using ABAQUS/Explicit to simulate the GW propagation and wave scattering phenomena in timber. Reflection and transmission ratios from different sizes of internal damage were obtained. An experiment was performed to validate the FE results. The validated FE model was then used to perform a series of parametric studies, and the results are given in Section 3.5.

3.3.1. Model definition

A 10 mm thick Tasmanian red oak was modelled in ABAQUS, which is the same as the specimen used in the experiment. To avoid unwanted reflections from the edges, the width and length of the timber were set to be 800 mm, which are large enough to avoid wave reflections from edges. The configuration of the model is shown in **Fig. 3.2** (a). A Cartesian coordinate is established to describe the locations of measurement points. The coordinate is defined at the surface of the timber, and the origin of system is defined at the excitation centre. x direction is aligned with timber fibre direction, which is also the direction of wave propagation. A symmetric boundary condition with respect to x axis was applied. Different sizes of internal damages were created at x = 290mm. To ensure the reflection wave is separated from the incident wave, the reflection wave measurement point is at x = 100mm while the transmission wave measurement point is at equal distance away from the damage with respect to reflection scanning point. The timber is modelled using 3D eight-node linear brick elements with reduced integration and hourglass control (C3D8R) element. To investigate the precision of using reduced integration element, 3D eight-node linear brick elements with incompatible mode, full integration, and hourglass control (C3D8I) were also used to model timber. C3D8I not only utilises full integration but also has additional degree of freedom, which can also capture bending motion. Identical results were obtained from these two

models. Since C3D8I is more computationally expensive, C3D8R was used in this study.

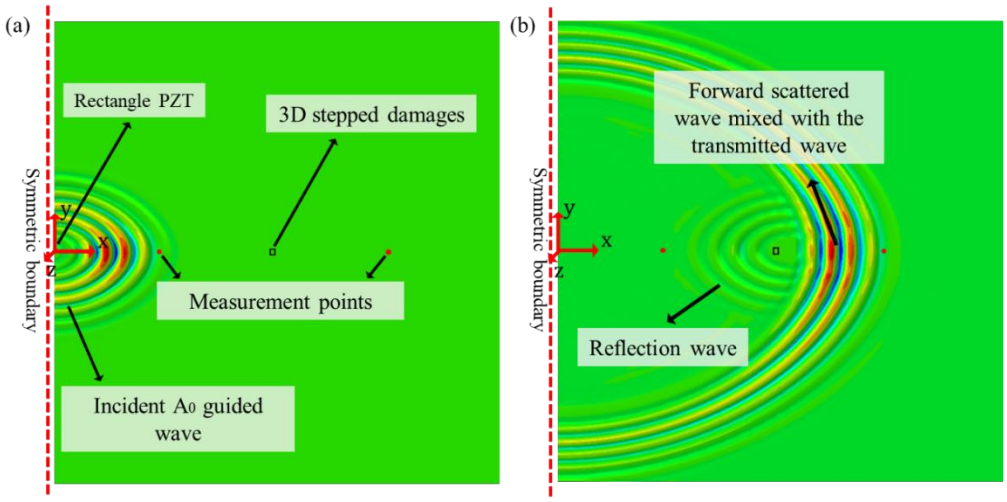

Fig. 3.2. Screenshot of out-of-plane displacements in *z* axis in a 10 mm red oak at different time steps: (a) right after incident A_0 wave was generated; (b) interaction of A_0 wave with the 3D stepped damages.

Red oak was modelled using transversely isotropic material in this study. The material properties are listed in Table 1 and density of the timber was measured to be 647.7 kg/m^3 [34]. Fibre direction (E_{11}) is aligned with *x* direction as shown **Fig. 3.2**. Young's modulus of fibre direction (E_{11}) is measured experimentally by means of time-of flight using GW, which is 10.5 GPa, shared a similar value of 8.91 GPa from reference [34].

Table 1 Elastic properties of Tasmanian red oak

E_{11} (GPa)	E_{22} (GPa)	E_{33} (GPa)	ϑ_{12}	ϑ_{13}	ϑ_{23}	G_{12} (GPa)	G_{13} (GPa)	G_{23} (GPa)
10.50	1.24	1.24	0.05	0.05	0.43	0.89	0.89	0.43

To simulate the wave attenuation in the model, Rayleigh damping is employed to simulate energy dissipation during wave propagation [25]. Attenuation constant k_i represents the rate of energy dissipation along the direction of the wave propagation and it is determined by fitting an exponential function to the experimental data for the decrement of signal amplitude versus distance [37, 38]. Eq. (10) shows the formula to obtain k_i, where x_1 and x_2 are the locations of measurement points, while A_1 and A_2 are the wave amplitudes, correspondingly.

$$\frac{A_1}{A_2} = \exp\left(k_i(x_2 - x_1)\right) \tag{10}$$

Mass-proportional damping constant (α_ω) and stiffness-proportional constant (β_ω) can then be computed using k_i. $\alpha_\omega = 2k_i c_g$ and $\beta_\omega = \frac{\alpha_\omega}{\omega^2}$, where c_g and ω are the group velocity and angular central frequency.

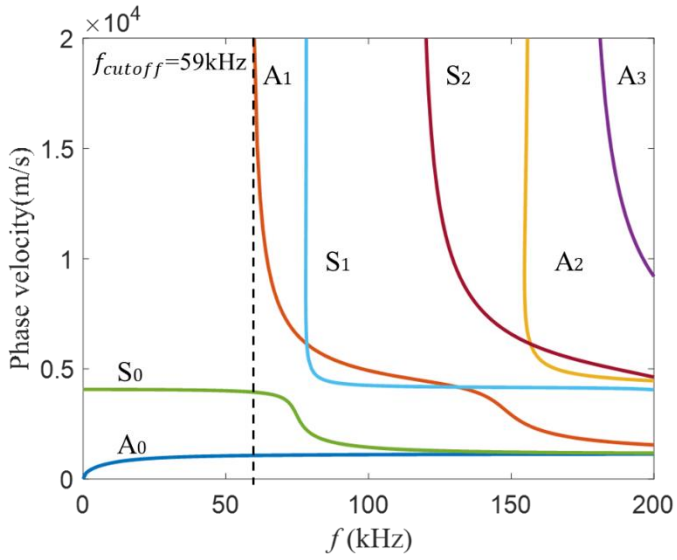

Fig. 3.3 Dispersion diagram for wave propagation along 0° in *x* direction in 10 mm Tasmanian red oak

The dispersion relationships for Lamb wave propagating along 0° in *x* direction in 10 mm Tasmanian red oak can be obtained by solving the governing equations Eqs. (7)-(9). The wave modes for up to 200 kHz are shown in **Fig.**

3.3. As shown in the **Fig. 3.3**, A_0 wave has smaller phase velocity and wavelength than S_0 GW under same excitation frequency. Therefore, A_0 GW is more sensitive to smaller damages, and hence, it is selected as the excitation wave mode in this study. The cut off frequency is 59 kHz. To minimize the complexity in wave analysis of higher orders and multi-modes, the excitation frequency is chosen below 59kHz. Theoretically, a higher frequency can have a smaller wavelength, which is more sensitive to smaller size of damage. However, it is found that 35 kHz can provide the best signal-to-noise ratio for the experimentally measured signal. Therefore, the excitation signal is selected as a 5-cycle narrow-band 35 kHz Hann windowed pulse and used for the rest of the study.

In the FE simulation, the A_0 wave is generated by applying out-of-plane displacements on a 12 mm × 6 mm rectangle region, which has the same size and shape as the PZT used in the experiment. The maximum element size and time increment were recommended to be less than $\Delta l = \frac{\lambda}{20}$; $\Delta t = \frac{1}{20f}$ to ensure the stability and accuracy of explicit analysis [39], where Δl is the maximum element size, Δt is the time step, λ is the wavelength of excitation signal, and f is the central excitation frequency. The wavelength is 28 mm for A_0 GW under selected excitation frequency 35 kHz. Therefore, the maximum element size is set to be 1 mm to ensures there are at least 28 elements existed per wavelength. To ensure the out-of-plane displacement is accurately modelled, the thickness of the element is set to be 1 mm and there are 10 layers of element in the thickness direction.

Fig. 3.2 (a) shows a snapshot of out-of-plane displacement in FE right after A_0 GW is excited. As shown in the displacement contour, the energy of incident A_0 wave concentrates along the fibre direction, which has dominant stiffness. Therefore, the measurement locations are defined along fibre direction to capture most of the wave energy. **Fig. 3.2** (b) shows the interaction of A_0 with the internal damage. As a result, reflection wave and forward scattered wave

are generated at the damage. It can also be seen that the forward scattered wave is mixed with the transmitted wave.

3.3.2. Simulation of internal damages

Internal damages were approximated as 3D semi-stepped damages in the model validation. This approximation was developed from a 2D stepped notch damage model, which was simulated to represent corrosion damage in metallic materials [40]. It was found that the stepped notches provide a realistic approximation to the corrosion damage. Therefore, it was utilized and further enhanced to 3D semi-stepped damages to represent the internal damages in the experiment.

Internal damages were created experimentally with a small surface entry, whose diameter equal to D_1. The diameter of the damage gradually increases from D_1 at the surface and reaches a maximum diameter D_2 at the mid-depth ($\frac{d}{2}$) of the timber, where d is the thickness of the timber. A schematic diagram of a 3D semi-stepped damage is shown in **Fig. 3.4**. As it can be seen in the *x-y* plane view, each layer of the 3D semi-stepped damage composed by a square. The diameter of the square damage gradually increases from the top surface (D_1) to mid-plane (D_2). Different internal damage cases were created by enlarging D_2, while D_1 and depth of the damage remained the same in the experiment. However, due to D_1, D_2 and depth of the damage were fixed, an identical 3D stepped damage with "unit increasing step" is inapplicable. For example, when there are n layers of squares, each layer will possess a thickness of $d/2n$ mm. However, the length and width of the squares in each layer are fixed as (D_2 - D_1) / ($2n$ – 2) mm. Therefore, if h/n is not equal to (D_2 - D_1) / ($2n$ - 2), the shape of each "unit step" becomes "semi-stepped". Denser elements were used to mesh the damage region to achieve good elements aspect ratio. Different sizes of 3D semi-stepped damages were validated by the experimental results and shown in Section 3.5.1. The experimentally validated FE model was then used to perform a series of numerical parametric studies to obtain the reflection and

transmission ratios for different internal damage cases in Sections 3.5.2 and 3.5.3.

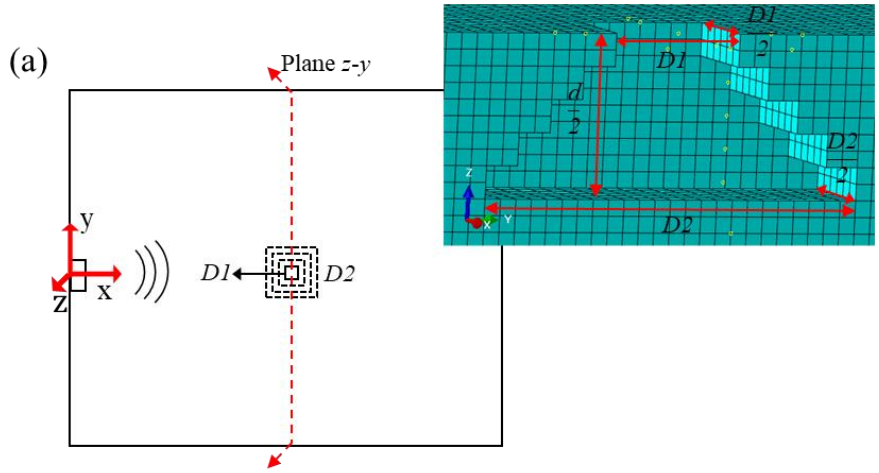

Fig. 3.4. Schematic diagram for a 3D FE semi-stepped damage

3.4. Experiment

An experiment was conducted to provide validation of the FE model, and physical understanding of the GW propagation in the timber and scattering at the internal damage. Reflection and transmission waves were measured for different sizes of internal damages to obtain the reflection and transmission ratios. A 10×90×1000 mm^3 ($d \times w \times l$) red oak structural timber was used in this study, which has the same thickness as FE model. Red oak is categorized as hard wood, which possesses a stiffer rigidity compared to most softwoods. Specimen dimensions are the same as the original product to ensure the practicability of the experiment. The properties of oak were determined as described in Section 3.3.1. All experimental measurements were conducted in an indoor environment on the same day. The indoor temperature was maintained at 27°, and hence, the moisture content of timber sample is assumed to remain unchanged. Internal damage generation, and the measurements for reflection and transmission wave are performed on a selected region of the specimen. The timber grain of the region is selected to be smooth, and hence,

no natural defects or obvious cracks are presented. Therefore, it is ensured that the received scattering waves are only generated by the internal damage

The A_0 wave was excited by a 2×12×6 mm^3 ($d \times w \times l$) surface-mounted rectangle PZT. The PZT was placed at 300 mm away from the right end and at the centre of the specimen. The locations of reflection and transmission wave scanning points, and the locations of internal damage are the same as those used in the FE simulation as shown in **Fig. 3.2**. The excitation signal was a 5-cycle narrow-band 35 kHz Hann windowed pulse, generated by a NI PXIE-5122 signal module. Due to the narrow width of the specimen, absorbing clay was attached at four edges of the timber to absorb unwanted wave reflections from edges. A Kron-Hite 7500 amplifier was used to amplify signal voltage. Signals were measured by a Polytec 1D scanning laser Doppler vibrometer before and after the wave interaction with the damages [41, 42]. Since the focus of this study is on A_0 GW, only out-of-plane displacements were measured. Reflective paints were evenly sprayed on scanning areas to improve light reflections on sample surface for the measurements. Sampling frequency was set to be 10.24 MHz with 1200 times samples averaging. A photo and a figure of schematic experimental setup are shown in **Fig. 3.5**(a).

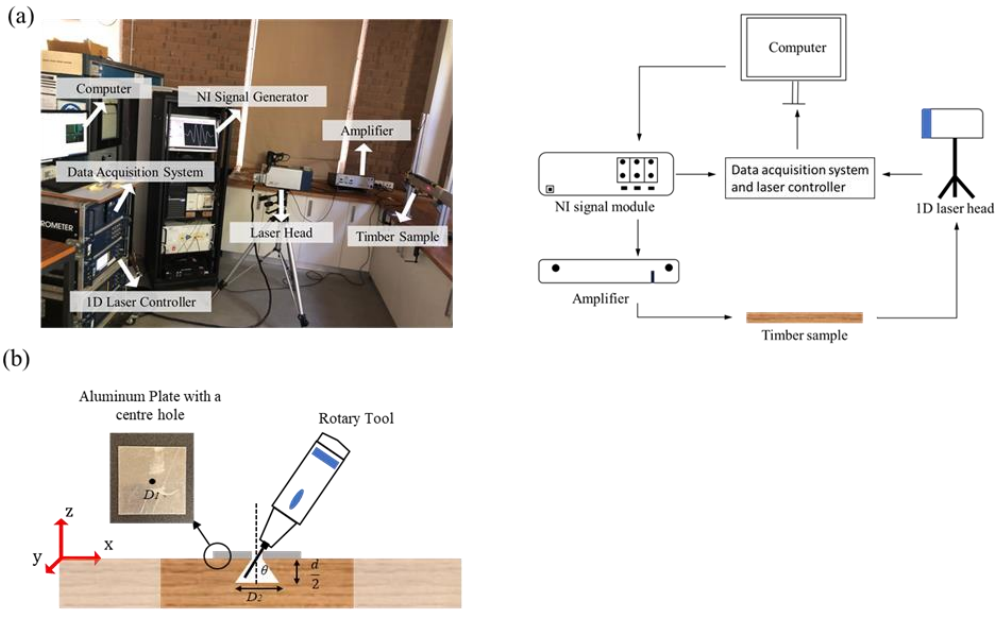

Fig. 3.5. (a) experimental setup and (b) zoomed view of the sections where internal damages were implemented in experiment

Before implementing internal damages on the specimen, the accuracy of the wave simulation in FE was validated by experimental results and the analytical dispersion curve. A 2D discrete Fourier transform (DFT) method was used in this study to validate A_0 GW in both numerical models and experiment results. 2D DFT method transforms the time-domain signals, which acquired from numbers of equally spaced measurement points along wave path, to frequency-wave number domain, so that superimposed wave signal resulting from multi-modes can be separated [43]. Applying 2D DFT to space-time signal $u(x,t)$ yields the following results [43]:

$$H_{\xi+1,f+1} = \frac{1}{MN}\sum_{n=1}^{N}\sum_{m=1}^{M} u_{n,m} e^{-2\pi i(\frac{\xi}{N}(n-1)+\frac{f}{M}(m-1))} \quad (10)$$

where f and ξ donate frequency and wavenumber; $u_{n,m}$ is the space-time signal consisting of M time samples at N measurement points.

Time-domain signals at 60 evenly spaced points along fibre direction were measured on the intact specimen. The excitation wave was a 5-cycle narrow-band 35 kHz Hann windowed pulse, which is the same as the FE model. The same Cartesian coordinate in **Fig. 3.2** is used to describe the measurement locations. The first measurement point is located at x = 100 mm, the rest of the points were distanced by an equal distance of 5 mm. It was experimentally determined that the number of measurement points and an equal measurement spaced of 5 mm are good enough to produce an acceptable resolution in the contour. In addition, zero paddings were used in time-domain and space-domain data to increase resolutions of the plots. Identical measurement locations were also defined in the FE model for performing the 2D DFT.

The 2D DFT results obtained from FE and experiment are shown in **Fig. 3.6** (a) and **Fig. 3.6** (b), respectively. A wavenumber-frequency contour is plotted with the analytical dispersion curves for the 10 mm thick oak timber

under the excitation frequency of 35 kHz. As shown in **Fig. 3.6** (a) and (b), there is excellent agreement for the experiment and FE data. The contours have good agreement with analytical A_0 dispersion curves. Moreover, contours reach a maximum amplitude around 35 kHz, which is the centre frequency of the excitation pulse and marked using a blue circle. The results show that A_0 is strongly dominant under the low frequency condition (35 kHz), and S_0 GW is not observed from the contour.

To capture the wave attenuations with FE, the out-of-plane displacements were also measured at the scanning area. By using Eq. (10), Rayleigh damping constants were computed as k_i=1.965 *Np/m*, α_ω= 4677.093 *rad/s* and β_ω = 9.671×10^{-8} *s/rad*.

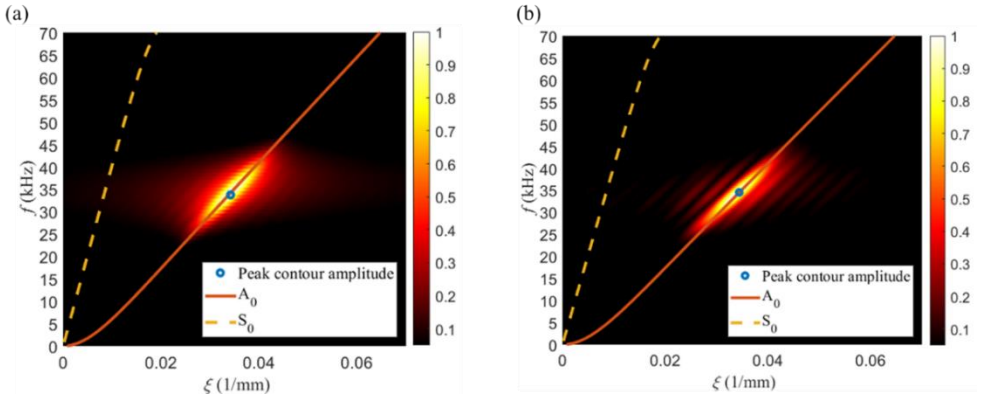

Fig. 3.6. Wavenumber-frequency contour plot and the analytical dispersion curves (solid line: A_0, S_0: dashed line) for a 10mm thick red oak, (a) FE results (b) Experimental results by 35kHz incident wave.

3.4.1. Generation of internal damage

Five different sizes of internal damages were investigated to obtain the reflection and transmission wave ratios. The locations of reflection and transmission wave scanning points, and the locations of internal damage are the same as in those used in the FE simulation as shown in **Fig. 3.2**.

Fig. 3.5 (b) shows a schematic diagram of the internal damage implementations. The diagram zooms in on the sections where internal damage is implemented. Experimentally, an internal damage cannot be created without comprising the integrity of the surface of the timber specimen. Therefore, a small surface hole with diameter (D_1 = 6 mm) is created to allow an internal access. The diameter of the internal damage increases gradually from the surface (D_1) and reaches the maximum diameter D_2 at mid-plane ($\frac{d}{2}$ = 5 mm) of the timber using a rotary tool. To control the sizes of internal damage diameters, an aluminium plate with a centre hole (diameter is equal to D_1), was temporarily mount on top of the timber surface. The centre hole on the aluminium plate provides a fixed rotational angle (θ) between rotary head and the vertical line, which provide a reasonable accuracy in generating the D_2 of the damage. To create different sizes of D_2, different sizes of rotary heads were substituted in the rotary tool. Each internal damage was created by rotating the rotary tool in 360°, which was considered to have equal damage extent in fibre and tangential direction. Due to the availability of rotary heads and aforementioned difficulties in control of the sizes D_2, five discrete sizes of D_2 were created (7 mm, 9 mm, 12 mm, 14 mm and 16 mm) providing that the depth of the damage and D_1 remain 5 mm and 6 mm, respectively.

Time signals were recorded for each damage size at the aforementioned locations. In addition, a fan was used to clean the accumulative wood dust inside the damage before the next drilling progression. **Fig. 3.7** (a) and (b) compare the FE results with the experiment time signal at reflection and transmission measurement locations for the case when D_2 = 7 mm. The time domain signals at reflection and transmission points are normalized with respect to the incident wave amplitude at the reflection measurement point. Both figures confirmed that the time of arrivals and the wave amplitudes in experiments are accurately predicted by FE. Mode conversion effect could occur through the interaction between A_0 GW and the internal damage, from which, the in-plane waves could be generated. However, the time domain data was recorded in out-of-plane

direction only due to the focus of this study is on A_0 GW. The magnitudes of the resulting in-plane waves are very small and have not been observed in the out-of-plane time domain data in both numerical and experimental data. Minor phase shifts are observed in **Fig. 3.7**, and due to following reasons: 1) the presence of local inhomogeneities in timber sample and 2) slight misalignments of damage size or location. It is also noticed there is a small unabsorbed wave component from the first reflection at sample width in **Fig. 3.7**(a). The unabsorbed wave component does not interfere with the reflection components from the damage as it can be seen that the two components are clearly separated.

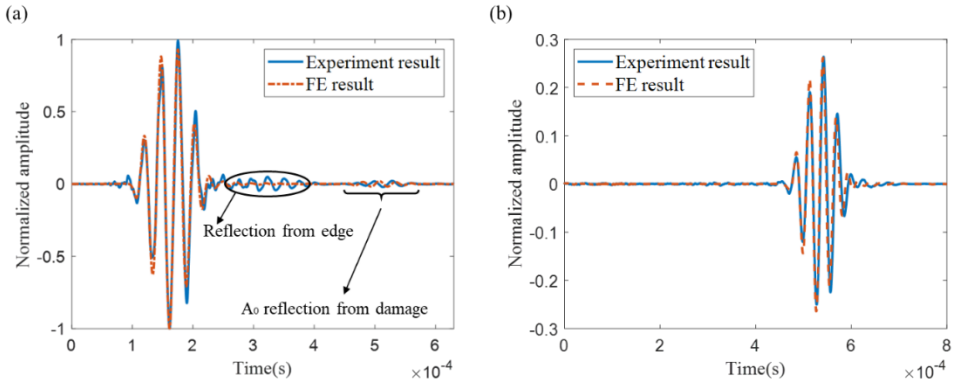

Fig. 3.7. FE and experimental time signal for internal damage size D_2 = 7 mm at (a) x = 100mm (b) x = 480 mm by 35kHz incident wave

3.5. Results of Numerical Case Studies

As descripted in Sections 3.3 and 3.4, reflection and transmission waves before and after the internal damages were captured. Three ratios are defined to quantify wave reflection and transmission ratios, which are reflection wave ratio r_r, transmission wave ratio r_{tr} and forward scattered wave ratio r_{trb}. These wave pockets are shown in **Fig. 3.2**. Forward scattered wave is retrieved by means of baseline subtraction due to it mixes with the transmission wave.

The ratios are calculated based on the same normalization method as before. They are normalized by the areas of the incident wave at the reflection point as follow:

$$r_r = \frac{A_r}{A_i}, \quad r_{tr} = \frac{A_{tr}}{A_i}, \quad r_{trb} = \frac{A_{tr} - A_{udtr}}{A_i} \tag{10}$$

where A_i, A_r and A_{tr} represent the areas under the incident pulse, reflection pulse, and transmission pulse in time-domain signal, respectively. The time-domain signals were computed as the absolute values when used to calculate the areas under the signal. A_{udtr} represents the areas under transmission wave for the undamaged case. As aforementioned, it is used for the purpose of baseline subtraction to obtain the forward scattered wave ratio (r_{trb}).

r_r and r_{tr} from the experimental and numerical results are shown in Section 3.5.1. The experimentally validated 3D FE model was then used to perform a series of parametric studies to further investigate the reflection and transmission effects from different internal damage cases. The wave measurement locations were defined consistently as before, and the wave excitation frequency was the same as 35 kHz. Section 3.5.2 shows the effects of internal damages with different dimensions. Section 3.5.3 shows the effects of the through thickness locations of internal damages.

3.5.1. Experimental results

r_r and r_{tr} obtained from five different sizes of internal damages are shown in **Fig. 3.8**(a) and (b). As for r_{trb}, baseline subtraction is impractical to measure in the experiment. It is because the specimen needs to be taken off from the laser scanning frame for creating the damage, hence, large phase shifts can be induced from a minor change in measurement location or a minor delay in wave generation each time. In general, the experimental results exhibit consistent trends as the FE results. Both experimental and FE results show that the r_r increases with the sizes of D_2 and reaches a peak at D_2 =16 mm, while the r_{tr} presents the opposite trend. A small discrepancy between FE and experiment predictions is observed in both figures. This is due to minor mismatches of shapes and sizes of the internal damages. From **Fig. 3.8**, the size of D_2 can be estimated from the reflection and transmission area ratio. Despite the internal

damages in the reality have irregular shapes, the experimental results still indicate the great sensitivity and potentials of GW for detecting timber internal damages.

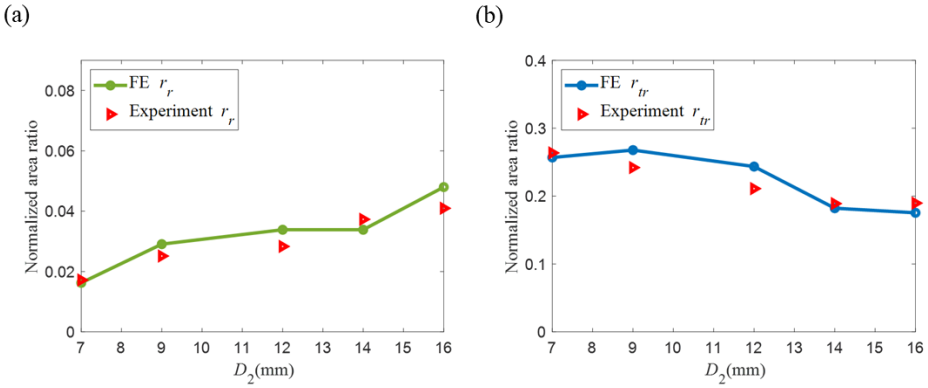

Fig. 3.8. Normalized area ratio for the (a) reflection wave (b) transmission wave resulting from internal damages by 35kHz incident wave

3.5.2. Effects of internal damages with different dimensions

The experimentally verified FE model was used to further investigate the reflection and transmission ratios for varying length (l), width (w), and thickness (t) of the internal damage. As shown in **Fig. 3.9**, the internal damages were modelled in an ideal cuboid shape to quantify l, w and t of the damage. The centroid of the internal damage is located at the mid-plane of the timber and is axial symmetric in both plane x-y and plane y-z.

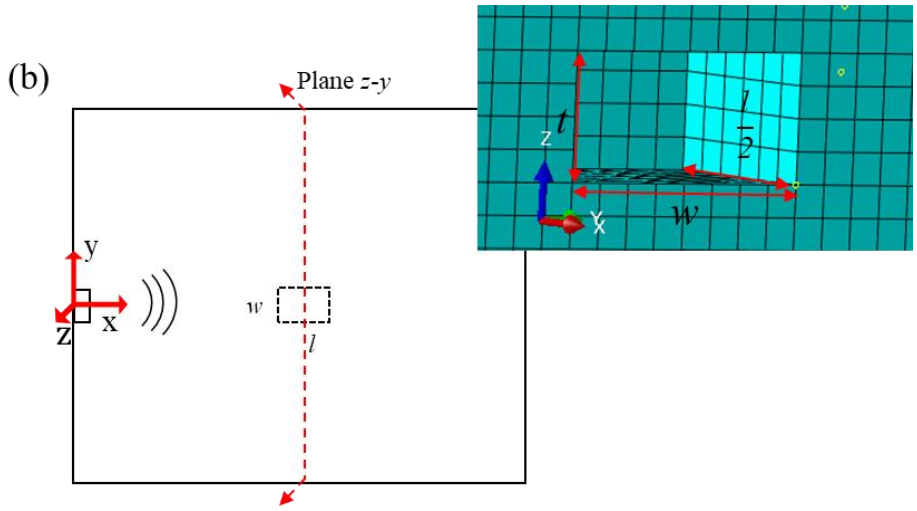

Fig. 3.9. Schematic diagram for FE internal damage with different dimensions

l and *w* of the damage were quantified with respect to wavelength (λ), while *t* of the damage was quantified with respect to the thickness (*d* = 10 mm) of the timber. The dimensions of the damage were initialized by 0.2λ×0.2λ×0.2*d* ($l \times w \times t$). Parametric studies were performed to vary one of these three parameters *l*, *w* and *t*, and keep the other parameters unchanged in the initial stage. *l* and *w* of the damage were swept from zero to 2λ with a step of 0.2λ respectively. *t* of the damage was swept from zero to a hundred percent of the *d* with a step of 0.1*d*. The parametric results are presented in the sequence of varying *l*, *w* and *t* as shown in the following paragraphs. In addition to r_r and r_{tr}, r_{trb} is also calculated. This is due to an ideal undamaged baseline is available from the numerical model.

Fig. 3.10 shows the results for varying *l*. In summary, r_{tr} and r_{trb} presented a more intuitive linear increasing trend compared to the r_r. This is due to r_r is affected by the interference between the first reflection pulse from the start of the damage and second reflection pulse from the far end of the damage. Two reflection pulses can either interfere constructively and destructively when length to wavelength ratio is equal to 0.2 and 0.3, respective, as shown in **Fig. 3.11** (a) and **Fig. 3.11**(b). A clear separation of two reflection waves can be

observed when length to wavelength ratio is equal to 1.8 as shown in Fig. 3.11(c).

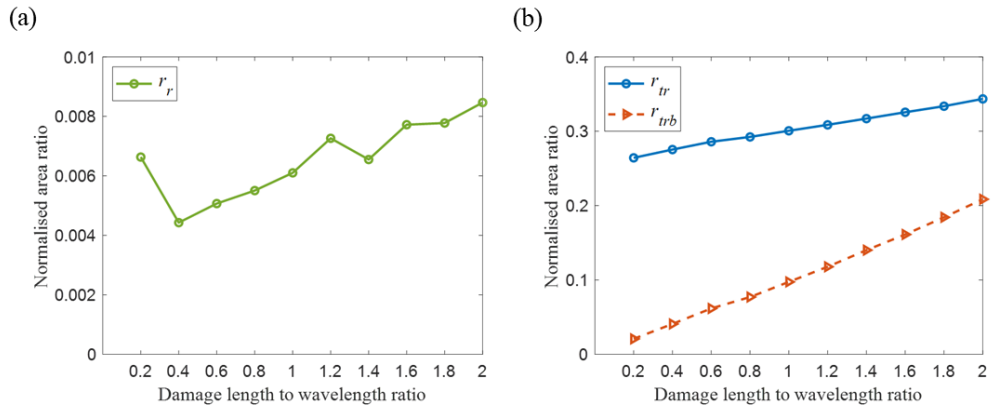

Fig. 3.10. Normalized area ratio for varying damage length for the (a) reflection wave (b) transmission wave (solid line) and forward scattering wave (dashed line) by 35kHz incident wave

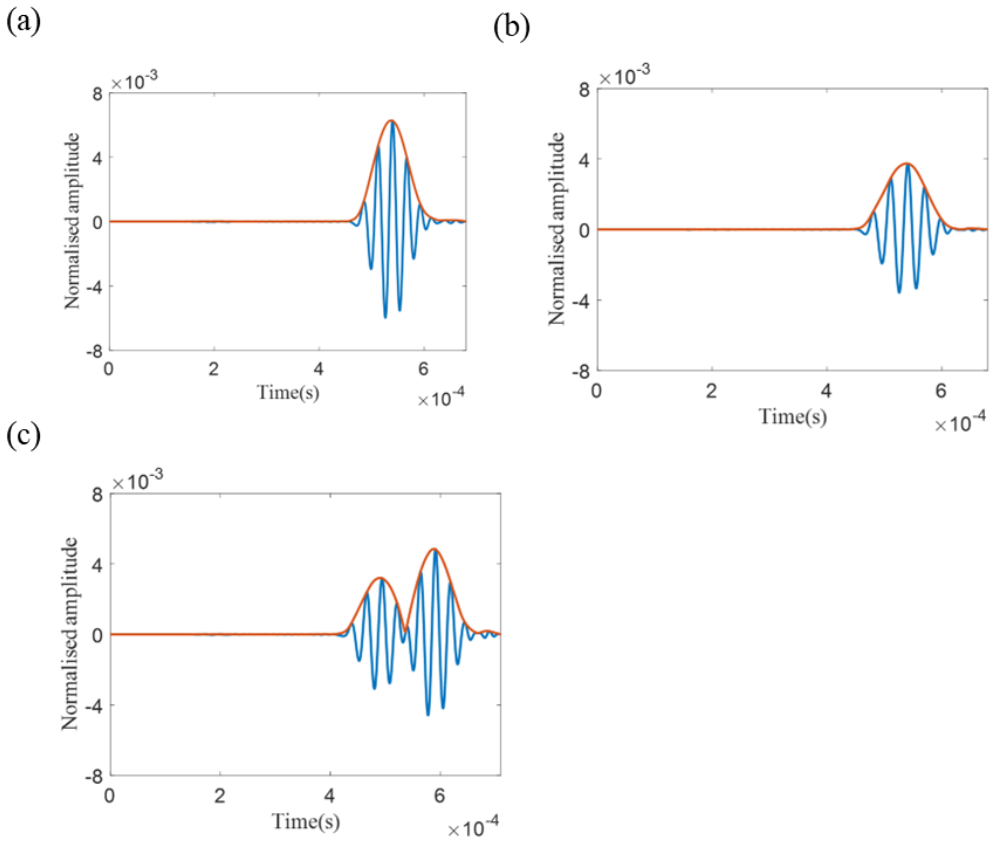

Fig. 3.11. Time signal of reflection wave at damage length to wavelength ratio equals to (a) 0.2, (b) 0.3 and (c) 1.8 by 35kHz incident wave

Fig. 3.12 and **Fig. 3.13** show the reflection and transmission results for varying w and t of the damage. As aforementioned, the l of the damage was kept to 0.2 wavelength, which minimize the destructive interference effects from interference phenomenon between two reflection waves as shown in **Fig. 3.11**(a). Despite the width and thickness of the damage were quantified differently, i.e. width was quantified with respect to wavelength while thickness was to the thickness of the timber, the trends of r_r, r_{tr} and r_{trb} in both cases display almost identical patterns. The results clearly indicate that r_r increases monotonically with the increasing damage width and depth, while r_{tr} and r_{trb} experienced a slight fluctuation.

In summary, r_r shows a more intuitive increasing pattern for the increasing size of internal damage compared to r_{tr} and r_{trb} and therefore more suitable to

be used for identifying the increasing size of the internal damage. Despite in general, r_{tr} and r_{trb} have larger amplitude than r_r, it is found that the patterns of r_{tr} and r_{trb} can fluctuate for different damage cases. Moreover, the measurement of the transmission wave requires the additional access to the far end of the damage, and hence, it is less practical compared to the measurement of the reflection wave.

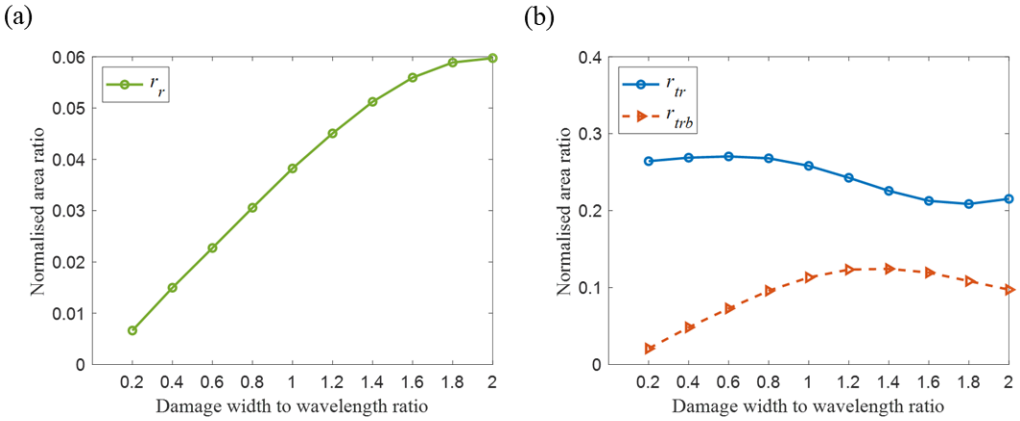

Fig. 3.12. Normalized area ratio for varying damage width for the (a) reflection wave (b) transmission wave (solid line) and forward scattering wave (dashed line) by 35kHz incident wave

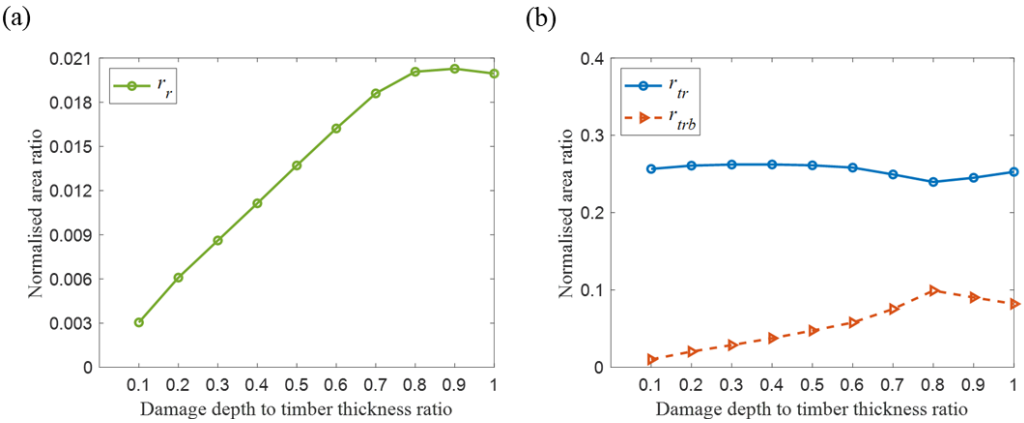

Fig. 3.13. Normalized area ratio for varying damage thickness for the (a) reflection wave (b) transmission wave (solid line) and forward scattering wave (dashed line) by 35kHz incident wave

3.5.3. Effect of internal damages with different thickness locations

Section 3.5.2 shows that results of the reflection and transmission wave for varying *l*, *w* and *t* are different. On the other hand, internal damage can exist in any through thickness locations. Therefore, it is also important to investigate the sensitivity of A_0 GW to the through thickness locations of the internal damage. Internal damages with different though thickness locations were modelled by the experimentally validated FE model. The FE model and wave excitation frequency are the same as those used as Section 3.5.2. **Fig. 3.14** shows a schematic diagram of the through thickness locations of the damage. The dimensions of the damage are 0.2λ×2λ×0.1d ($l \times w \times t$). The through thickness locations of the damage is represented by the lower surface of the damage and described by z axis. Therefore, the locations of the damage were moved from upper surface z = -1 mm to z = -10 mm with a step of 0.1d. It is noteworthy that when z = -1 mm and z = -10 mm, the damage is a surface notch located at the upper and the lower surface of the timber, respectively.

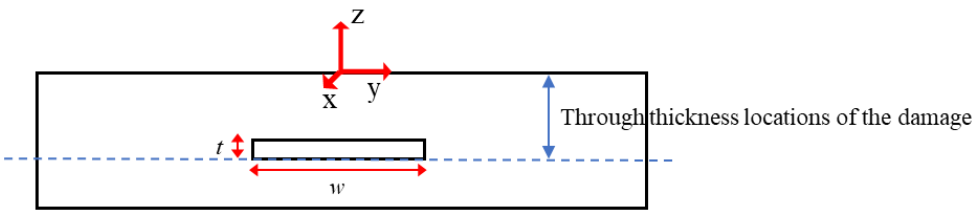

Fig. 3.14. Schematic diagram of through thickness location of the internal damage

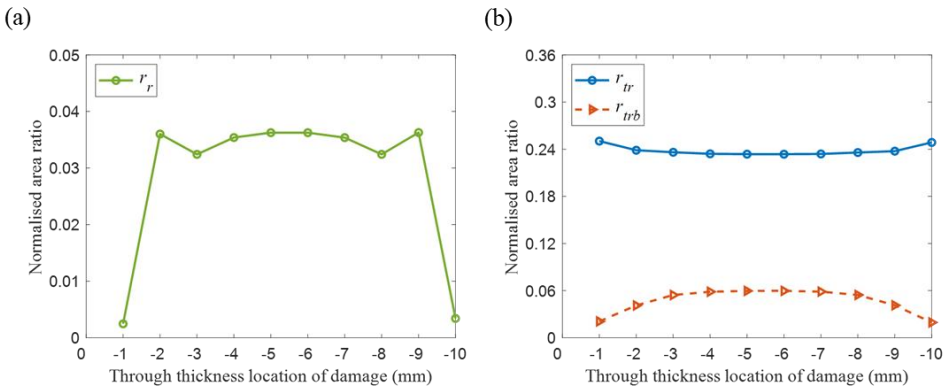

Fig. 3.15. Normalized area ratio for internal damage with different through thickness locations (lower surface of the damage in z axis location) for the (a) reflection wave (b) transmission wave (solid line) and forward scattering wave (dashed line) by 35kHz incident wave

The reflection and transmission results are shown in **Fig. 3.15**(a) and (b). r_r, r_{tr} and r_{trb} show symmetric patterns with respect to the mid-plane of the timber. This is because of the symmetric out-of-plane displacement mode shape of A_0. The changes of the damage location can change the bending stiffness of the timber. Therefore, the response of reflection wave r_r changes correspondingly. According to **Fig. 3.15**(a), r_r reached the maximum amplitude of at the mid-plane of the timber at *z* = -5 mm and *z* = -6 mm, while r_r has the minimum amplitude at the damage is a surface notch at *z* = -1 mm and *z* = -10 mm. It is also noteworthy that when the damage is a surface notch, z = -1 mm and *z* = -10 mm, the amplitude of r_r is much smaller than that is located internally. Therefore, based on the amplitude of r_r, it is concluded that A_0 GW is more sensitive to the damage located internally than the damage located at the surface i.e. surface notch at 35 kHz. Furthermore, the fluctuation of r_r also indicated that even if the damage size is the same, the reduction in timber stiffness can vary for the different through thickness locations of the damage.

3.6. Limitations of the Proposed Study

Despite the reflection and transmission area ratios measured from the experimental internal damages display a simple monotonical pattern, the application of GW for practical application in timber damage detection can be more complex. The limitations of the proposed methods are discussed in this section.

The first challenge is the multimodal nature of GW. As shown in **Fig. 3.3**, the cut-off frequency for a 10mm red oak timber is 59kHz. To minimize the complexity in wave analysis of higher orders and multi-modes, the excitation frequency is chosen below the cut-off frequency. In real-cases, timber might have a much larger thickness than the specimen in this study. This results a smaller cut-off frequency and therefore the excitation frequency needs to be reduced. For structural timber with large thicknesses, a different GW type such as surface wave, longitudinal wave might be considered as the excitation mode. Moreover, the generation of internal damage and the measurements for reflection and transmission wave are performed on a selected region of the specimen in this study. The wood grain of the region is selected to be smooth, and hence, no natural defects or obvious cracks are presented. When the size of timber is much larger, it is impossible to avoid the existence of timber natural defects. Therefore, a baseline state of the sample with natural defects is required to extract the damage-related information, which can become a more complex analysis. To account for the high-variability in damage conditions and timber properties, the GW technique can be combined with the data-driven approaches such as machined learning in future research, which paves the way for real-cases online monitoring.

3.7. Conclusion

This paper has provided a comprehensive wave scattering study from the internal damages for a structural timber using GW. The study helps to improve the in-situ timber damage assessment using GW. Different sizes of internal damage have been created experimentally on a structural timber member using a rotary tool. The reflection and transmission ratios of wave have been measured before and after the internal damages. The experimental internal damages have been modelled by the 3D semi-stepped damage in 3D FE simulation. A good agreement has been achieved between the experimental and the numerical results. In summary, both r_r and r_{tr} obtained from the experiment results have simple trend, in which r_r increases with the size of the damage while r_{tr} has the opposite trend. Therefore, it can be used for identifying the internal damage size in the experiment. To simplify the level of anisotropy, timber properties have been modelled as transversely isotropic for simulating the wave propagation on the timber and have proven to be accurate in the FE simulation. It has been shown that the energy of the wave concentrates along the fibre direction and the low frequency incident A_0 GW has low attenuation when propagating along the fibre direction.

The experimentally validated FE model was used to study the reflection and transmission effects of damages with different *l*, *w* and *t*. In general, r_r presents an intuitive increasing pattern compared to r_{tr} and r_{trb} and therefore more suitable to be used for identifying the increasing size of the internal damage. However, the amplitude of r_r is smaller than the r_{tr} in most of the cases. It has also been observed that when varying *l* of the damage, two reflection waves from start and far end of the damage can either interfere constructively, or destructively due to different arrival times of the two reflection waves. Therefore, a slight fluctuation has been observed in r_r for varying the damage *l*. In addition, the reflection and transmission effects of damage with different though thickness locations have been studied. It has been found that for the

same size of damage, when the location of the damage is at the surface, i.e., a surface notch, the amplitude of r_r is much smaller than those cases when the damage is located internally.

In summary, this study has confirmed the robustness and sensitivity in detecting conspicuous damages in timber using A_0 GW. The findings in this study have provided improved insights into GW interaction with internal damage in structural timber, revealing the potentials for the application of GW in timber damage detection.

3.8. Acknowledgement

This work was funded by the Australian Research Council (ARC) under the grant number DP210103307. The authors are grateful for this support.

3.9. References

1. Ghanbari-Ghazijahani, T., J. Wu, and C.-T. Ng, *Plastic buckling and axial crushing of concrete-filled steel tubes: usage of multiple wood blocks.* Thin-Walled Structures, 2020. **150**: p. 106487.
2. Palma, P. and R. Steiger, *Structural health monitoring of timber structures - Review of available methods and case studies.* Construction and Building Materials, 2020. **248**: p. 118528.
3. El Najjar, J. and S. Mustapha, *Condition assessment of timber utility poles using ultrasonic guided waves.* Construction and Building Materials, 2021. **272**: p. 121902.
4. Aseem, A. and C.T. Ng, *Debonding detection in rebar-reinforced concrete structures using second harmonic generation of longitudinal guided wave.* NDT & E International, 2021. **122**: p. 102496.
5. Pineda Allen, J.C. and C.T. Ng, *Nonlinear Guided-Wave Mixing for Condition Monitoring of Bolted Joints.* Sensors, 2021. **21**(15): p. 5093.
6. Ross, R.J., *Inspection of timber bridges using stress wave timing nondestructive evaluation tools: a guide for use and interpretation*. Vol. 114. 1999: US Department of Agriculture, Forest Service, Forest Products Laboratory.

7. Mousavi, M., et al., *Feature extraction of wood-hole defects using empirical mode decomposition of ultrasonic signals.* NDT & E International, 2020: p. 102282.
8. Cruz, H., et al., *Guidelines for on-site assessment of historic timber structures.* International Journal of Architectural Heritage, 2015. **9**(3): p. 277-289.
9. Hadlington, P.W., *Australian termites and other common timber pests*. 1996: UNSW Press.
10. Ghaly, A. and S. Edwards, *Termite damage to buildings: Nature of attacks and preventive construction methods.* Am J Eng Appl Sci, 2011. **4**(2): p. 187-200.
11. Mori, M., et al., *Nondestructive evaluation of bending strength of wood with artificial holes by employing air-coupled ultrasonics.* Construction and Building Materials, 2016. **110**: p. 24-31.
12. Dietsch, P., et al., *Methods to determine wood moisture content and their applicability in monitoring concepts.* Journal of Civil Structural Health Monitoring, 2015. **5**(2): p. 115-127.
13. Nasir, V., H. Fathi, and S. Kazemirad, *Combined machine learning–wave propagation approach for monitoring timber mechanical properties under UV aging.* Structural Health Monitoring, 2021: p. 1475921721995987.
14. Kappel, R. and C. Mattheck, *Inspection of timber construction by measuring drilling resistance using Resistograph F300-S.* WIT Transactions on the Built Environment, 2003. **66**.
15. Ceraldi, C., V. Mormone, and E.R. Ermolli, *Resistographic inspection of ancient timber structures for the evaluation of mechanical characteristics.* Materials and structures, 2001. **34**(1): p. 59-64.
16. Diakhate, M., et al., *Cluster analysis of acoustic emission activity within wood material: Towards a real-time monitoring of crack tip propagation.* Engineering Fracture Mechanics, 2017. **180**: p. 254-267.
17. Yang, X., et al., *Application of modal analysis by transfer function to nondestructive testing of wood I: determination of localized defects in wood by the shape of the flexural vibration wave.* Journal of wood science, 2002. **48**(4): p. 283-288.
18. Hu, C. and M.T. Afzal, *A statistical algorithm for comparing mode shapes of vibration testing before and after damage in timbers.* Journal of Wood Science, 2006. **52**(4): p. 348-352.
19. Farrar, C.R., S.W. Doebling, and D.A. Nix, *Vibration–based structural damage identification.* Philosophical Transactions of the Royal Society of London. Series A: Mathematical, Physical and Engineering Sciences, 2001. **359**(1778): p. 131-149.
20. Dackermann, U., B. Skinner, and J. Li, *Guided wave–based condition assessment of in situ timber utility poles using machine learning algorithms.* Structural Health Monitoring, 2014. **13**(4): p. 374-388.
21. Ross, R.J., B.K. Brashaw, and R.F. Pellerin, *Nondestructive evaluation of wood.* Forest products journal, 1998. **48**(1): p. 14.

22. Mousavi, M., et al., *Feature extraction of wood-hole defects using empirical mode decomposition of ultrasonic signals.* NDT & E International, 2020. **114**: p. 102282.
23. Yang, H. and L. Yu, *Feature extraction of wood-hole defects using wavelet-based ultrasonic testing.* Journal of forestry research, 2017. **28**(2): p. 395-402.
24. Sanabria, S.J., et al., *Air-coupled ultrasound inspection of glued laminated timber.* 2011.
25. Soleimanpour, R. and C.-T. Ng, *Scattering analysis of nonlinear Lamb waves at delaminations in composite laminates.* Journal of Vibration and Control, 2021: p. 1077546321990145.
26. Hu, X., C.T. Ng, and A. Kotousov, *Scattering characteristics of quasi-Scholte waves at blind holes in metallic plates with one side exposed to water.* NDT & E International, 2021. **117**: p. 102379.
27. Dahmen, S., et al., *Elastic constants measurement of anisotropic Olivier wood plates using air-coupled transducers generated Lamb wave and ultrasonic bulk wave.* Ultrasonics, 2010. **50**(4-5): p. 502-507.
28. Fathi, H., S. Kazemirad, and V. Nasir, *Lamb wave propagation method for nondestructive characterization of the elastic properties of wood.* Applied Acoustics. **171**: p. 107565.
29. Fathi, H., S. Kazemirad, and V. Nasir, *A nondestructive guided wave propagation method for the characterization of moisture-dependent viscoelastic properties of wood materials.* Materials and Structures, 2020. **53**(6): p. 1-14.
30. Li, J., M. Subhani, and B. Samali, *Determination of embedment depth of timber poles and piles using wavelet transform.* Advances in Structural Engineering, 2012. **15**(5): p. 759-770.
31. Yu, Y., et al., *Wavelet packet energy–based damage identification of wood utility poles using support vector machine multi-classifier and evidence theory.* Structural Health Monitoring, 2019. **18**(1): p. 123-142.
32. Subhani, M., J.C. Li, and B. Samali, *A comparative study of guided wave propagation in timber poles with isotropic and transversely isotropic material models.* Journal of Civil Structural Health Monitoring, 2013. **3**(2): p. 65-79.
33. Subhani, M., et al., *Reducing the effect of wave dispersion in a timber pole based on transversely isotropic material modelling.* Construction and Building Materials, 2016. **102**: p. 985-998.
34. Green, D.W., J.E. Winandy, and D.E. Kretschmann, *Mechanical properties of wood.* Wood handbook: wood as an engineering material. Madison, WI: USDA Forest Service, Forest Products Laboratory, 1999. General technical report FPL; GTR-113: Pages 4.1-4.45, 1999. **113**.
35. Zhang, J., Y. Huang, and Y. Zheng, *A feasibility study on timber damage detection using piezoceramic-transducer-enabled active sensing.* Sensors, 2018. **18**(5): p. 1563.
36. Nayfeh, A.H. and D.E. Chimenti, *Free wave propagation in plates of general anisotropic media.* 1989.

37. Ramadas, C., et al., *Modelling of attenuation of Lamb waves using Rayleigh damping: Numerical and experimental studies.* Composite Structures, 2011. **93**(8): p. 2020-2025.
38. Mohseni, H. and C.T. Ng, *Rayleigh wave propagation and scattering characteristics at debondings in fibre-reinforced polymer-retrofitted concrete structures.* Structural Health Monitoring-an International Journal, 2019. **18**(1): p. 303-317.
39. He, S., C.T. Ng, and C. Yeung, *Time-Domain Spectral Finite Element Method for Modeling Second Harmonic Generation of Guided Waves Induced by Material, Geometric and Contact Nonlinearities in Beams.* International Journal of Structural Stability and Dynamics, 2020. **20**(10).
40. Demma, A., et al., *The reflection of guided waves from notches in pipes: a guide for interpreting corrosion measurements.* Ndt & E International, 2004. **37**(3): p. 167-180.
41. Hughes, J.M., et al., *Damage detection with the fundamental mode of edge waves.* Structural Health Monitoring, 2021. **20**(1): p. 74-83.
42. Hughes, J.M., et al., *The fundamental ultrasonic edge wave mode: Propagation characteristics and potential for distant damage detection.* Ultrasonics, 2021. **114**: p. 106369.
43. Alleyne, D. and P. Cawley, *A two-dimensional Fourier transform method for the measurement of propagating multimode signals.* The Journal of the Acoustical Society of America, 1991. **89**(3): p. 1159-1168.

3.10. Appendix A

Coefficients of Eq. (6) for wave propagates in a transversely isotropic plate

$$B_1 = [C_{11}C_{33}C_{44} - {C_{13}}^2C_{44} - 2C_{13}C_{44}C_{55} + C_{33}{C_{55}}^2 - (C_{33}C_{44} + C_{33}C_{55} + C_{44}C_{55})\,\rho c^2] /(C_{33}C_{44}C_{55}) \quad (A1)$$

$$B_2 = [C_{11}C_{33}C_{66} + C_{11}C_{44}C_{55} + {C_{13}}^2C_{55} - 2C_{13}{C_{55}}^2 - \left(C_{33}C_{11} + C_{11}C_{44} - {C_{13}}^2 - 2C_{13}C_{55} + C_{33}C_{55} + C_{55}C_{44} + {C_{55}}^2\right)\rho c^2 + (C_{33} + C_{44} + C_{55})\rho^2 c^4] /(C_{33}C_{44}C_{55}) \quad (A2)$$

$$B_3 = [C_{11}{C_{55}}^2 - \left(2C_{11}C_{55} + {C_{55}}^2\right)\rho c^2 + (C_{11} + 2C_{55})\rho^2 c^4 - \rho^3 c^6]/(C_{33}C_{44}C_{55}) \quad (A3)$$

Solutions of Eq. (6) for wave propagates in a transversely isotropic plate

$$\alpha_{1,3} = \frac{-B \pm [B^2 - 4AC]^{\frac{1}{2}}}{2A}, \alpha_2 = -\alpha_1, \alpha_4 = -\alpha_3, \alpha_5 = -\alpha_6 = [(\rho c^2 - C_{66})/C_{44}]^{1/2} \quad (A4)$$

where

$$A = C_{33}C_{55}$$
$$B = (C_{11} - \rho c^2)C_{33} - (C_{55} - \rho c^2)C_{55} - (C_{13} + C_{55})^2 \quad (A5)$$
$$C = (C_{11} - \rho c^2)(C_{55} - \rho c^2)$$

4. Detection of Edge Delamination in Composite Laminates using Edge Waves

(Under preparation)

Jinhang Wu [a], Chang Jiang [a,*], Ching-Tai Ng [a,*], Han Fang [b]

[a] *School of Architecture and Civil Engineering, University of Adelaide, Adelaide, South Australia, 5000, Australia*

[b] *School of Civil Engineering, University of Leeds, Leeds, 00000, United Kingdom*

Statement of Authorship

Title of Paper	Detection of edge delamination in composite laminate using edge wave
Publication Status	☐ Published ☐ Accepted for Publication ☐ Submitted for Publication ☑ Unpublished and Unsubmitted work written in manuscript style
Publication Details	Wu, J., et al., Detection of edge delamination in composite laminate using edge wave.

Principal Author

Name of Principal Author (Candidate)	Jinhang Wu
Contribution to the Paper	Conceptualization, Methodology, Writing – original draft.
Overall percentage (%)	
Certification:	This paper reports on original research I conducted during the period of my Higher Degree by Research candidature and is not subject to any obligations or contractual agreements with a third party that would constrain its inclusion in this thesis. I am the primary author of this paper.
Signature	Date 20/10/2023

Co-Author Contributions

By signing the Statement of Authorship, each author certifies that:

i. the candidate's stated contribution to the publication is accurate (as detailed above);
ii. permission is granted for the candidate in include the publication in the thesis; and
iii. the sum of all co-author contributions is equal to 100% less the candidate's stated contribution.

Name of Co-Author	Chang Jiang
Contribution to the Paper	Methodology, Advising, Writing – original draft.
Signature	Date 10/20/2023

Name of Co-Author	Ching Tai Ng
Contribution to the Paper	Supervision, Writing – review & editing.
Signature	Date 23/10/2023

Please cut and paste additional co-author panels here as required.

Name of Co-Author	Han Fang		
Contribution to the Paper	Supervision, Advising		
Signature	Han Fang	Date	20/10/2023

Abstract

Detecting near-edge damage in composite structural elements using guided wave-based techniques can be challenging, primarily due to the complexity of wave analysis arising from material anisotropy. Furthermore, scattered waves containing damage information can be contaminated by waves reflected from the edges, which makes detecting near-edge damage difficult to implement. In the literature, studies showed that in elastic materials, the edge of a structure can serve as a waveguide, enabling the existence of typical edge modes with concentrated energy at the edge. However, studies regarding edge waves in composite structures have received limited attention. This paper aims to explore the potential of detecting edge delamination damage in composite laminates using edge waves. The modal properties of edge waves in composite laminates with different stacking sequences are investigated using Semi-Analytical Finite Element (SAFE) method. Following this, numerical and experimental studies were conducted to investigate the sensitivity of edge waves in detecting edge delamination in the composite laminates. The outcomes of this study provide physical insights into the modal properties of edge waves in composite laminates and confirm the capability of edge waves in detecting damage near the edges.

Keywords: Edge waves, Composite laminates, Edge delamination detection, Ultrasound, Guided waves

4.1. Introduction

Fibre-reinforced composite materials have been widely utilized to enhance the mechanical properties of construction materials due to their lightweight and high-strength characteristics. Recent advancements in non-destructive evaluation (NDE) techniques have shown promise in detecting the early stages of damage in composite laminates, including delamination, fiber breakage and cracks [1]. Notably, prior research has highlighted that the edges of composite laminates are particularly vulnerable to damage. Composite laminates are susceptible to free-edge delamination, which can arise from high interlaminar stresses near the free edge due to the mismatch of elastic properties between adjoining plies [2]. Additionally, composite laminates tend to be more fragile to impacts occurring near or on their edges, resulting in a greater reduction in compressive strength compared to impacts at the center [3]. Typical damage occurring at edges, such as delamination, can substantially reduce the material stiffness and propagate under service-related loadings, therefore, compromising structural integrity. Moreover, it is often challenging to detect delamination due to its limited visibility.

Ultrasonic-based techniques have been widely applied within the NDE community for detecting damage in composite structures. This is primarily because they offer fast, sensitive, and long-range inspection capabilities. The dispersion relations of guided waves in composite materials display unique complexities when compared to isotropic materials. These include factors like the direction-dependent phase velocity, steering effects, and mode coupling. Scattering studies were conducted for Lamb wave in a quasi-isotropic composite laminate at delamination [4, 5] and through hole damage , demonstrating the good sensitivity of Lamb waves in detecting small delamination sizes. Time-domain data of scattering waves were utilized in studies focused on damage detection in composite materials [6, 7]. These

studies integrated a damage detection algorithm within a sensor network to generate an image for determining the location of the damage. Nonlinear analysis techniques employing the contact acoustic nonlinearity (CAN) effect were also applied for delamination detection in composite materials [8, 9]. The generation of higher harmonics can provide a good indication for the presence of defects. On the other hand, studies focusing on damage detection on or near the edges of composite laminates using guided waves receive relatively less attention. This is attributed to a range of challenges, such as the potential for the wave signal that carries defect information, to be contaminated by boundary reflection waves [10]. Additionally, propagating modes typically exhibit coupling, multi-modal behaviour, and complex dispersion relations.

As opposed to a source of scattering, it has been discovered that the edge of a structure can serve as a waveguide, concentrating wave energy and allowing the wave to propagate in one dimension. These waves, referred to edge waves, encompass two fundamental modes: the fundamental flexural mode (EA_0) and fundamental extensional wave (ES_0), in the elastic materials[11]. Modal solutions for edge waves in the low-frequency range were initially derived using two-dimensional (2D) plate theories in pioneering studies. Subsequently, theoretical studies were extended to describe edge wave in a three-dimensional (3D) plate, leading to the development of more precise modal solutions for edge waves at higher frequency ranges [12, 13]. The semi-analytical finite element (SAFE) approach resolves the eigenvalue problem by integrating analytical expressions along the wave propagation direction on a 2D discretised cross-section. Rekatsinas et al. [14] developed a multimode explicit layer-wise spectral finite element method for modelling both the physical presence of piezoelectric sensors, the existence of delamination cracks, and the excitation of each fundamental wave mode separately. Although the study investigated the efficient simulation of wave propagation, it mainly focused on transient wave responses and is unable to provide the frequency domain response of composite structures and efficient dispersion and wave structure

analysis. Similarly, Lonkar and Chang [15] introduced a layered solid spectral element for modelling piezo-induced ultrasonic wave propagation in composite structures. Despite the computational efficiency of the spectral element method compared with the traditional finite element method, neither of them can be used for efficient guided wave dispersion, mode shape, and frequency response analysis of a given structure [16]. In the recent studies, the SAFE method was applied to obtain dispersion curves and modeshapes for surface Rayleigh waves [17] and edge waves [18, 19]. Additionally, SAFE approaches were employed to investigate flexural edge waves propagating at the apex of a wedge [20]. The propagation characteristics of edge waves in different wedge-like features were analysed and compared to the wave modes in the ideal wedge, providing practical examples for inspecting members containing wedge features. Edge waves were employed to identify damages along the edges of metallic structures, including aluminium plates [21] and I-beams [18]. 3D finite element (FE) models and experiments were conducted in these studies. Studies focusing on edge waves in composite materials have received limited attention, with the majority focusing on theoretical calculations of modal solutions [12, 13]. Chu and Courtney [22] conducted a damage detection study to detect impact damage at the free edge using ES_0 on a composite laminate. Their results demonstrated that edge waves can travel over considerable distances, enabling inspection coverage that spans several meters. However, comprehensive studies that delve into the characteristics of existing edge modes in composite laminates, their behaviours, and the potential for detecting delamination at the free edge using edge waves are lacking.

This paper aims to explore the potential of detecting edge delamination in a $[(0/90)_2]_s$ composite laminate using edge waves. Modal studies were conducted using the SAFE approach. It was found that edge waves can be distinguished from other modes by their high energy concentration at the edge, making them suitable for detecting edge delamination damage. The study also found that the orientation of the fibre can strongly influence the energy

concentration between laminae. While the primary focus was on edge waves in the composite laminate with a stacking sequence $[(0/90)_2]_s$, a dispersion curve for edge waves in a composite laminate with a stacking sequence [0/45/90/-45]s is also provided for comparison. Three wave modes, labelled as Mode1 to Mode 3 in this study, are identified as great candidates for detecting edge delamination in the composite laminate with a stacking sequence $[(0/90)_2]_s$. Subsequently, the study explores the methods for exciting these modes and assesses their sensitivity to various sizes of delamination through a 3D FE analysis. Lastly, experimental studies are performed to validate the numerical results. Reflection ratios from an edge delamination damage are experimentally measured using a pulse-echo configuration.

4.2. Edge Waves in a Composite Laminate

4.2.1. SAFE model

To investigate the edge wave in composite laminates, the SAFE method [17, 19] is adopted to numerically calculate the possible propagating waves within the specified waveguide, predicting their wavenumbers and leakage coefficients. The SAFE modelling process leverages the efficiency of analytical descriptions in the wave propagation direction while discretising the cross-section of the waveguide with arbitrary shape. Consequently, the 3D wave propagation problem can be reduced to a 2D problem, describing the displacement vector in the plate as follows

$$u(X_1, X_2, X_3, t) = U(X_1, X_2)exp[J(kX_3 - \omega t)], \quad (1)$$

where X_1, X_2, X_3 are the axis of a global coordinate, k is the complex wavenumber, ω is the angular frequency, t is the time variable, J is the imaginary unit, and U is the maximum displacement amplitude. **Fig. 4.1** shows the SAFE model of the composite laminate. The edge waves are assumed to

propagate harmonically along the X_3 direction. The dynamic equilibrium equation is given by

$$\sum_{j,k,l=1}^{3}\left[C_{ijkl}\frac{\partial^2 u_k}{\partial X_j \partial X_l}\right] = -\rho\omega^2 u_i, i = 1,2,3, \qquad (2)$$

where C_{ijkl} are the components of the elastic stiffness tensor of anisotropic materials, and ρ is the mass density. Substituting Eq. (1) into Eq. (2), the wave motion equation of an eigenvalue problem can be obtained as follows

$$C_{ijkl}\frac{\partial^2 U_k}{\partial X_j \partial X_l} + J\left(C_{i3kj} + C_{ijk3}\right)\frac{\partial (kU_k)}{\partial X_j} - kC_{i3k3}(kU_k) + \rho\omega^2\delta_{ik}U_k = 0, (3)$$

where the summation is over the indices *k*=1, 2, 3 and *j*, *l*=1, 2, and δ_{ik} is the Kronecker delta. For Eq. (3), the wavenumber k can be considered as the eigenvalue, and the equation can be solved using a commercial FE package [19].

In this study, a 1.6mm thick eight-ply $[(0/90)_2]_s$ composite laminate is considered. The composite laminate is constructed using T300/M914 carbon/epoxy prepreg. The SAFE model is developed to calculate the dispersion curves, modeshapes, and wave structures of edge waves. These wave characteristics are independent characters of the material damping in composite laminate. Hence, the composite laminate is assumed to be undamped. The elastic constants M_{ijkl} of the lamina are shown in Table 2.

Table 2 Elastic constants (in GPa) of lamina T300/M914 used in this study

M_{11}	M_{12}	M_{13}	M_{22}	M_{23}	M_{33}	M_{44}	M_{55}	M_{66}
13.3	6.5	6.2	13.3	6.2	143.8	5.7	5.7	3.4

A local material coordinate system (x_1, x_2, x_3) is used to compute the elastic constant of each lamina. The fibre direction is aligned with the x_3 direction, and an angle of $\theta°$ is defined to describe the rotation around x_1 axis. For a ply with a 90° direction fibre, θ is equal to 90°. The elastic stiffness tensor C_{ijkl} in the global coordinate system is then calculated by

$$C_{ijkl} = R * M_{ijkl} * R^t, (4)$$

where R is the rotation matrix and R^t represents the transpose of R.

A perfectly matched layer (PML) layer [24] was implemented at the top end of the laminate, as shown in **Fig. 4.1**. This PML layer functions as a wave-absorbing region, providing advantages in reducing the model size and enhancing computational efficiency. It was determined that a PML length of 60 mm is sufficient to achieve convergence in the SAFE model. An edge tip domain is defined at the bottom of the laminate, and to connect the edge tip with the PML region, a plate with a length of 100 mm is introduced. It is worth noting that in elastic materials, the energy of the edge wave is primarily concentrated at a depth of approximately one to two wavelengths from the free edge end [18, 25]. Therefore, the length of the edge tip should be selected to adequately encompass the primary energy concentration regions of the edge wave, especially the one with the longest wavelength within the calculated frequency range. The combined length of the edge tip and plate should cover the entire energy concentration regions of the edge wave to avoid interference with the PML regions. In this study, the considered frequency range extends up to 1 MHz, resulting in a maximum frequency thickness value (FTV) [26] of around 3 (with a shear velocity of approximately 1700 m/s for both fast and slow shear velocities). Based on the findings of edges modes in isotropic materials [18, 19], it is expected that fundamental edge modes are the predominant edge modes at low FTV regions (for FTV values up to 4), and their wavenumbers closely resemble those of fundamental Lamb and shear horizontal waves. Therefore, it is anticipated that ES_0 possesses the longest wavelength within the specified frequency range and can be adequately represented with an edge length of 40 mm. The plate region of the 2D model is discretised using free triangle elements with a size of 0.2 mm. Denser meshes with a size of 0.067 mm were applied to the edge tip domain and the PML domain, ensuring approximately three elements per layer in the thickness direction. The eigenvalue problem is solved up to 1 MHz, and the imaginary part of the wavenumber k represents the wave attenuation coefficient.

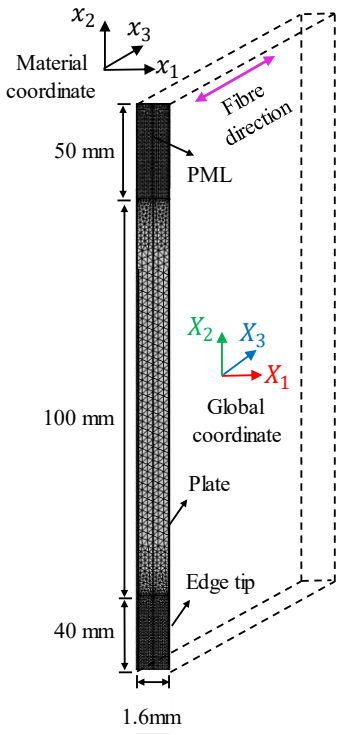

Fig. 4.1. Schematic diagram of SAFE model of a 1.6mm $[(0/90)_2]_s$ composite laminate (not to scale).

4.2.2. SAFE results

The obtained solutions at each frequency were assessed using a filtering algorithm [27, 28]. In this study, a ratio denoted as η is introduced to represent the power flow of edge wave propagation in the edge tip domain over that in the entire plate domain. The fundamental criterion for distinguishing edge waves from the rest of the solutions is that the power flow of these modes should be concentrated as extensively as possible at the edge tip. A criteria for mode selection, as reported in [19], is applied to ensure that the power flow at the edge tip region exceeds that at the PML region. The SAFE results are shown in **Fig. 4.2** using scatter plots, where brighter colours indicate a higher energy concentration at the edge tip, and vice versa. Dispersion curves for Lamb and shear horizontal modes were computed and are displayed in the figure using lines. Notably, within the calculated frequency range (i.e., the low FTV range,

FTV ≤ 4), the dispersion relations of the filtered results closely resemble those of their plate mode counterparts. Similar results have been reported in the studies focused on edge waves in elastic materials. [18, 26].

Three modes with high η value (bright colour) were identified in the proximity to the fundamental antisymmetric mode (A_0), fundamental shear horizontal mode (SH_0) and fundamental symmetric mode (S_0). They are labelled as "Mode 1" to "Mode 3" in the **Fig. 4.2**, where Mode 1 was identified as the fundamental flexural edge mode (EA_0) and Mode 2 was identified as the fundamental extensional edge mode (ES_0), respectively. Furthermore, an additional Mode 3, exhibiting the same wavenumber as S_0, was also detected. Remarkably, this mode was not observed in isotropic materials. The imaginary part of the wavenumbers, representing the attenuation due to the leakage [29], is plotted in **Fig. 4.2** (d). The results indicate that at frequencies below 180 kHz, all three modes exhibit relatively small η values (represented by green and blue colours on the colour bar) with a relatively high value of the imaginary part of the wavenumber. This is because edge waves have not fully developed at these frequencies, and a portion of their energy is concentrated in the plate, flowing towards the PML. The energy flowing towards the PML region will be absorbed, resulting in its imaginary part of the wavenumber. The magnitude of the imaginary part of the wavenumber of Mode 1 and Mode 2 becomes negligible when the frequency exceeds 200 kHz. Conversely, Mode 3 exhibits leakage across the calculated frequency domain. It was discovered that Mode 3 radiates SH_0 into the composite laminate, which has a smaller phase velocity than Mode 3. A detailed investigation is provided later in Section 4.3.3. Similar phenomena of leaky modes with smaller phase velocities than the incident feature guided waves have been reported in other studies [29, 30]. Additionally, solutions were observed near and first order antisymmetric wave (A_1) with relatively small η values.

When selecting suitable wave modes and frequencies for detecting edge delamination, it is advisable to choose an excitation frequency that achieves several goals: maintaining a relatively high η value at the chosen frequency, minimizing the number of propagating modes, and minimizing dispersive effects [10]. Consequently, Mode 1 to Mode 3 within frequency range of 250 kHz to 500 kHz (i.e., below the first-order antisymmetric cut-off frequency) are deemed preferable for these reasons. Detailed discussions regarding the modeshapes of Mode 1 to Mode 3 within the frequency range of interest are provided in the subsequent section.

As shown in **Fig. 4.2**, the dispersion curves of edge waves closely resemble those of their plate mode counterparts for an 8-ply $[(0/90)_2]_s$ composite laminate. It is also intriguing to investigate whether this pattern still holds true for a composite laminate containing a 45° degree lamina. Dispersion curves of edge waves in a quasi-isotropic composite laminate are provided in **Appendix A** for comparison. A more detailed investigation into this aspect can be considered for future research, although it falls beyond the scope of this study.

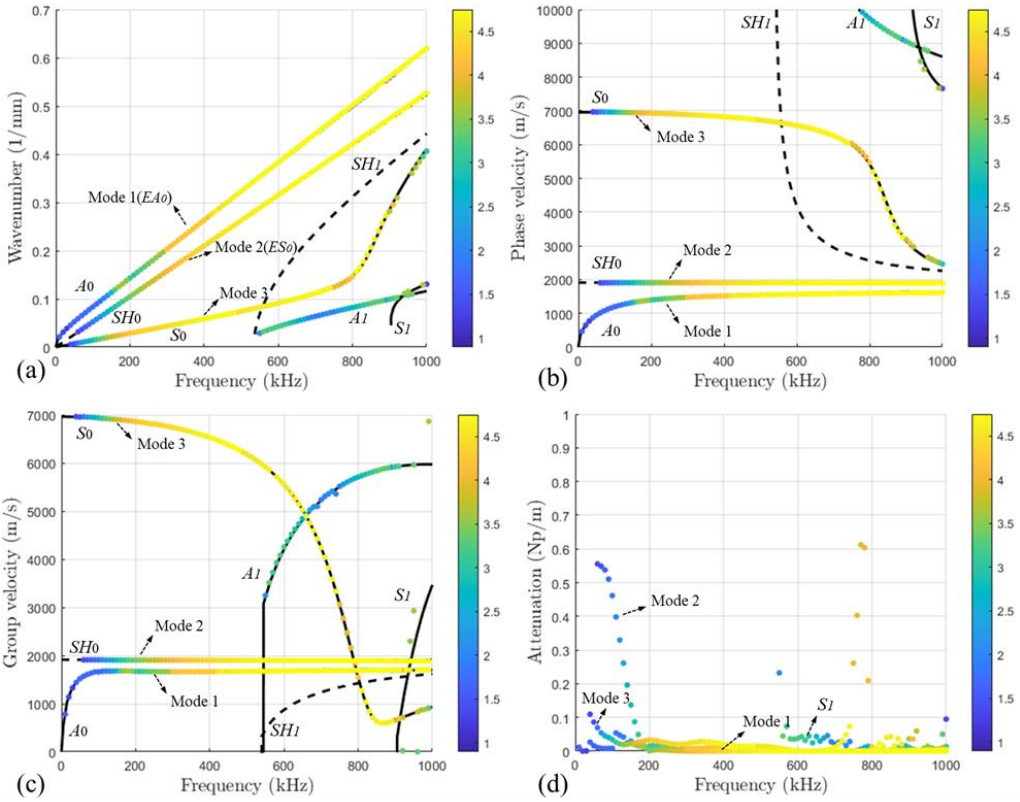

Fig. 4.2. Dispersion curves for a 1.6mm $[(0/90)_2]_s$ T300/M914 composite laminate along 0° propagation direction (scatter plot: edge waves calculated from SAFE, line plot: Lamb and shear horizontal modes) (a) frequency-wavenumber, (b) frequency-phase velocity, (c) frequency-group velocity, (d) frequency-attenuation. The colour bar represents the η value (brighter colour denotes higher energy concentration in the edge tip). (For interpretation of the references to colour in this figure legend, the reader is referred to the Web version of this article.)

4.2.2.1. Mode and frequency selection

Modeshapes of Mode 1 to Mode 3 at 400kHz are shown in **Fig. 4.4** (a) to (c), respectively. Additionally, for comparison, modeshapes of EA_0 and ES_0 at 400kHz in a 1.6mm steel plate are also presented in **Fig. 4.3** (a) and (b), respectively. The displacement field of EA_0 and ES_0 shows little difference from

that in the steel plate: EA_0 exhibits a u_1-dominated displacement field, while Mode 2 exhibits a u_2-dominated displacement field (i.e., shear direction for the plate). However, a significant difference can be observed in the distribution of power flow. It is evident that the fiber direction can significantly influence the power flow distribution, with a 0° orientation fibre providing the strongest guidance for energy flow. Additionally, it was found that Mode 3 have a u_3-dominated displacement field, with its energy notably concentrated on the 0° laminae. All three modes satisfy the requirement of having the most energy concentration occurring at the edge tip.

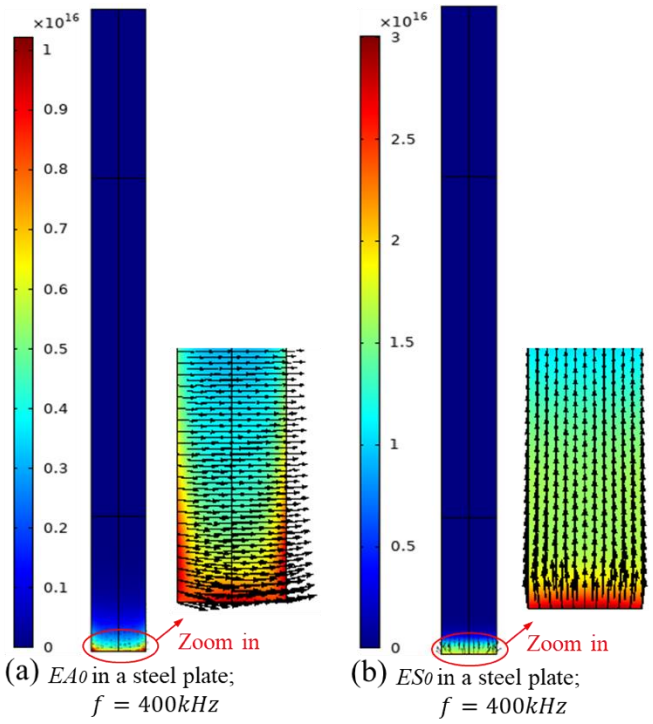

Fig. 4.3. Modeshapes of (a) EA_0 and (b) ES_0 at 400 kHz in a 1.6mm steel plate. Contour plot represents the axial power flow, and black arrows represents and sectional displacements (u_1 and u_2).

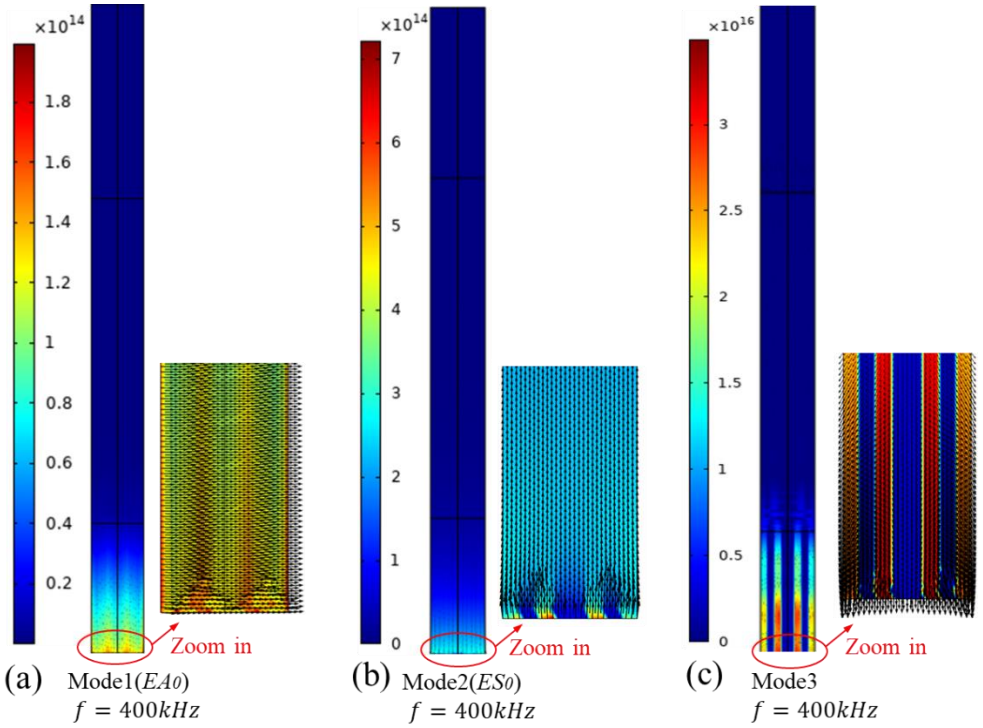

Fig. 4.4. Modeshapes of (a) Mode 1, (b) Mode 2, (c) Mode 3, labelled in Fig. 2 (a), in a 1.6mm $[(0/90)_2]_s$ T300/M914 composite laminate (not to scale). Colour bar and arrows have the same meaning as **Fig. 4.3**.

As shown in **Fig. 4.2**, the scatter plot colour for all three modes become increasingly brighter with rising frequency, signifying an increase in the η value. To delve deeper into this, two measurement lines were defined. They are labelled as "Line 1" and "Line 2" in **Fig. 4.5**, respectively. The magnitude of axial power flow was measured at the meshed points along these two lines for all three wave modes from 250 kHz to 500 kHz, with a 50 kHz increment. The results for Mode 1 are shown in **Fig. 4.5** (a) and (b); for Mode 2 in (c) and (d); and for Mode 3 in (e) and (f), respectively. The results suggest that for all three modes the axial power flow concentrates more towards the edge as the frequency increases. Furthermore, the results indicate that the orientation of the fiber has a more significant influence on the energy distribution of symmetric modes compared to anti-symmetric modes. This phenomenon is shown in **Fig.**

4.5 (a), (c) and (e). For Mode 1 (i.e., anti-symmetric mode) , the normalized value of axial power flow concentrated at the 90° lamina is around 0.75 to 0.8 compared to 1 at the 0° lamina. However, little to no energy concentration can be observed at the 90° lamina for both Mode 2 and Mode 3 (both are symmetric modes). Further details regarding the excitation methods and the sensitivity of these modes to edge delamination will be examined and discussed in the later sections of this paper.

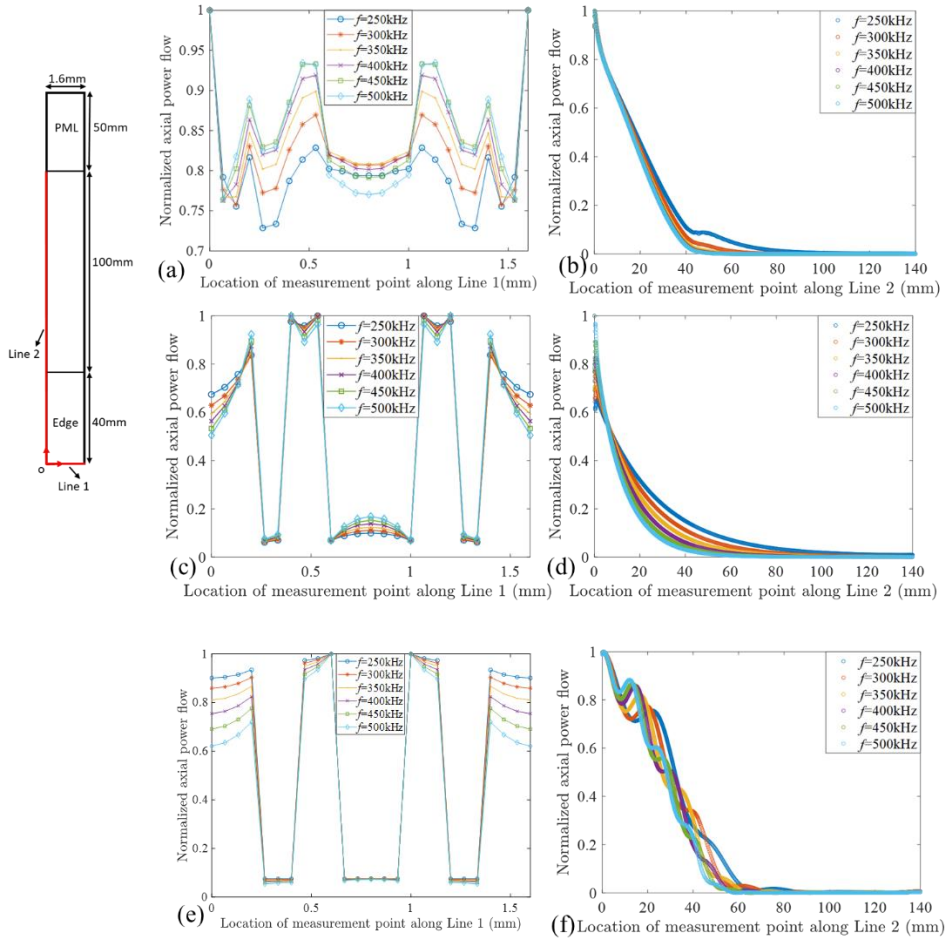

Fig. 4.5. The axial power flow distribution for Mode 1 is shown along (a) Line 1 and (b) Line 2, for Mode 2 along (c) Line 1 and (d) Line 2, and for Mode

3 along (e) Line 1 and (f) Line 2 within the specified frequency range. A reference system is provided at the left side of the figure.

4.3. 3D Finite Element Models

4.3.1. Finite Element Setup

A 3D explicit FE model was developed using ABAQUS/CAE to validate the SAFE results and explore the sensitivity of Mode 1 to Mode 3 in detecting edge delamination. A 1.6mm $[(0/90)_2]_s$ composite laminate was modelled, utilizing the material properties detailed in **Table 2**, with each lamina rotated according to specifications. Tie constraint was applied at the interfaces to join each laminae. The model is 600mm in length and 400mm in width. The assembled structure was then meshed using 3D eight-node linear brick elements with reduced integration (C3D8R). The thickness of the laminate was discretised with eight layers of elements, and each laminae was meshed using a single-layer element with a thickness of 0.2 mm. The length and width of each element were determined to be 1 mm by 1 mm, resulting in a total of 1,920,000 elements used in the mesh. Absorbing layers with increasing damping (ALID) were defined at two ends of the laminate to avoid boundary reflections, as shown in a typical screenshot in **Fig. 4.6** (a). In this study, the ALID regions at the two ends of the laminate were subdivided into 40 equally spaced layers. Mass-proportional damping was incrementally raised from the innermost layer to the outermost layer. The coefficients for mass-proportional damping at each layer were expressed as $\alpha(x) = \alpha_{max} X(x^3)$ [31]. The value of α_{max} was determined to be 6×10^6 through trial and error.

The excitation signal for all three wave modes was a 7-cycle narrow-band Hann windowed pulse with a centre frequency of 350 kHz. Mode 1 to Mode 3 were generated using different excitation methods. Mode 1, characterized by a mid-plane anti-symmetrical displacement field primarily in

the X_1 direction, was generated by applying anti-symmetric u_1 displacements within two 12 mm × 6 mm areas (i.e. labelled as piezoelectric transducer (PZT) in **Fig. 4.6** (a)), one on each side of the laminate. An additional incident flexural mode was generated and propagated along the edge in the X_2 direction. Notably, this mode propagated at a slightly different velocity compared to the incident Mode 1. This velocity difference can be attributed to variations in their dispersion relations (i.e., the lamina rotation for the mode propagating in the X_2 direction is $[(90/0)_2]_s$). Conversely, Mode 2 exhibits a mid-plane symmetrical displacement field primarily in the X_2 directions (shear direction to the plate). Mode 2 was generated by applying displacements perpendicular to the upper edge. **Fig. 4.6** (c) shows the snapshot captured shortly after generating Mode 2. It is found that SH_0 mode was also generated simultaneously and propagated at the same velocity with Mode 2. Lastly, Mode 3 was generated using the same excitation method as Mode 1, with the only difference being a change in the sign of displacements on one side of the laminate, resulting a symmetrical excitation. **Fig. 4.6** (e) shows the generation of Mode 3. It has been observed that Mode 3 shares some common modal properties with the S_0 Lamb wave in the current structure, including the same wavenumber and wave velocity. In this study, edge waves are defined as wave modes with energy highly concentrated in the edge region. The development of the SAFE model ensures that only modes with substantial energy concentration at the edges are preserved (i.e., a high Eta value). Under this concept, Mode 3 aligns with the definition of an edge mode and show potential to detect near-edge damage. Additionally, Mode 3 displays leakage at the excitation frequency, radiating SH_0 to the plate, as predicted by the SAFE method.

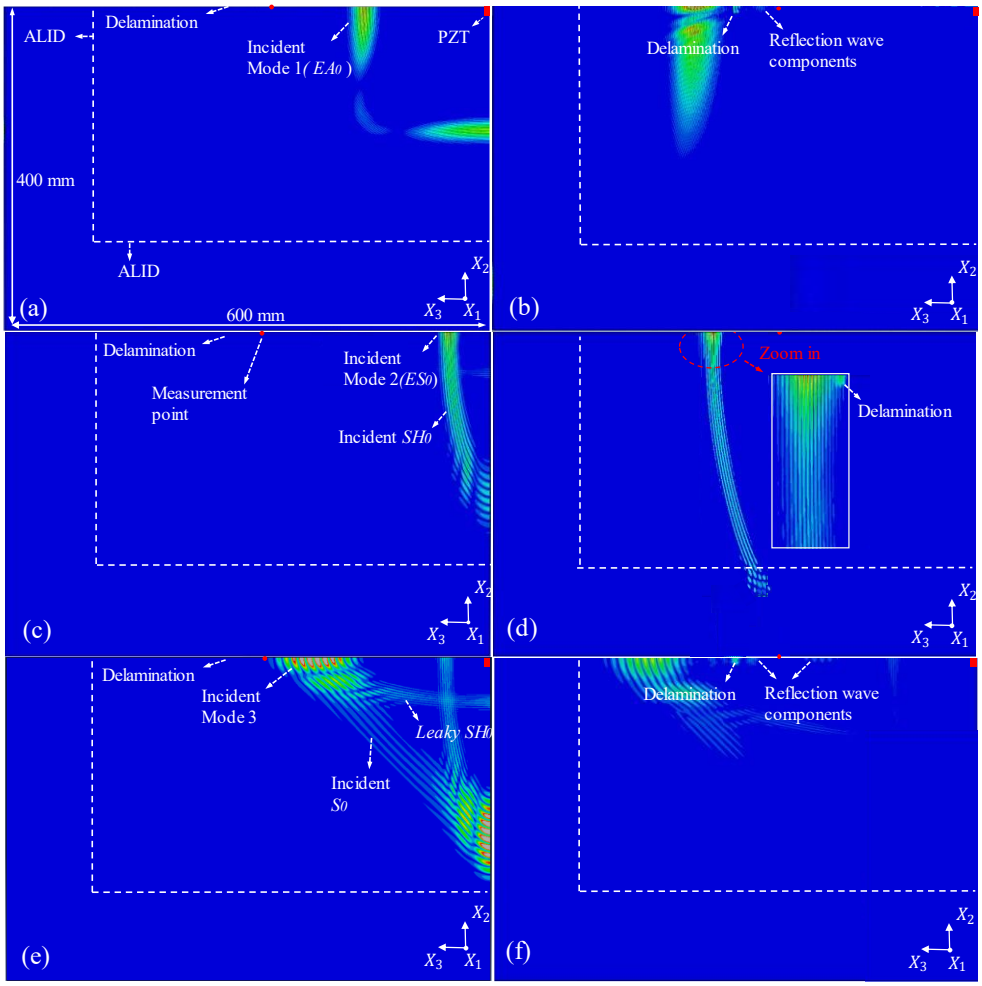

Fig. 4.6. Snapshot for a $[(0/90)_2]_s$ composite laminate with an edge delamination of size D =10 mm located between the second and third layers: (a) shortly after Mode 1 was generated (screenshot taken at 1.05×10^{-4} s), (b) after the interaction of Mode 1 with the damage (screenshot taken at 1.75×10^{-4} s); (c) shortly after Mode 2 was generated (screenshot at 0.26×10^{-4} s), (d) after the interaction of Mode 2 with the damage (screenshot taken at 1.41×10^{-4} s); (e) shortly after Mode 3 was generated (screenshot taken at 3.27×10^{-4} s), (f) after the interaction of Mode 3 with the damage(screenshot taken at 5.06×10^{-4} s). The colour code represents the relative magnitude of total displacement, with blue indicating low and red indicating high displacement.

4.3.2. Model verification

Before commencing damage detection studies, an intact model was utilized to validate the outcomes of SAFE methods. The wavenumbers of three modes at 350kHz were validated using a 2D discrete Fourier transform (DFT) method. A total of 30 measurement points, each spaced by 1 mm apart, were defined along the upper edge of the composite laminate. The first measurement point was defined at 200mm away from the excitation source. For Mode 1 and Mode 3, out-of-plane displacements (U_3) were recorded at these measurement points, while for Mode 2, displacement in the shear direction (U_2) were recorded. The results of the 2D-DFT are illustrated in **Fig. 4.7**(a) to (c), demonstrating a good agreement between the two results. Additionally, the group velocity for each mode was calculated within the selected frequency ranges. The group velocity was calculated by dividing the distance of each measurement point by the time difference of arrival. Time-domain data from the first 15 measurement points were employed to compute the group velocity, and the average value was used to represent the final result. The results are shown in **Fig. 4.7** (d). For Mode 1 and Mode 2, the difference between FE results and SAFE results falls within a 5% interval, while for Mode 3, the difference is within a 12% interval. This discrepancy in Mode 3 can be attributed to its slight dispersion at the chosen frequency range.

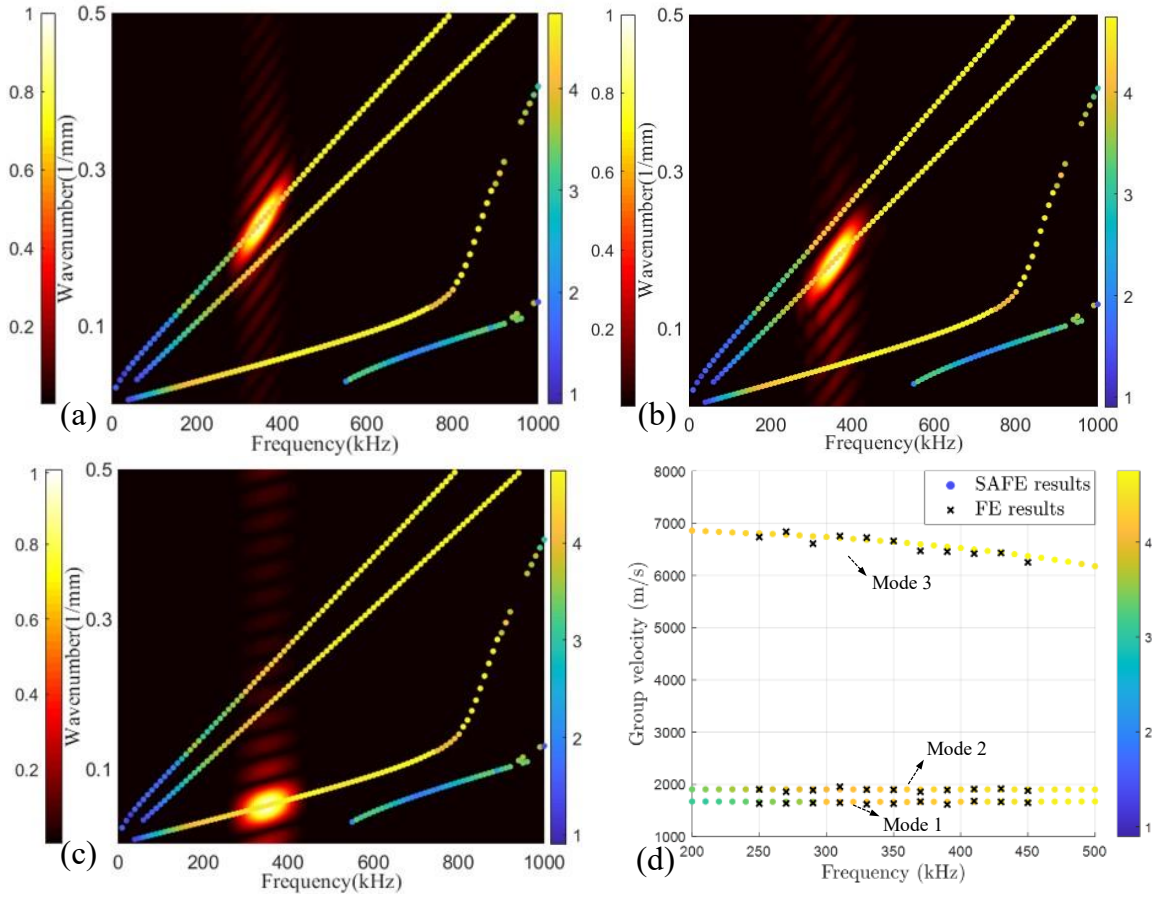

Fig. 4.7. FE 2D-DFT plot and the SAFE dispersion curve for (a) Mode 1, (b) Mode 2, and (c) Mode 3. (d) FE validation of group velocity for Mode1 to Mode 3.

4.3.3. Reflection ratios of EA_0 and ES_0

The sensitivity of the three wave modes in detecting edge delamination damage was assessed through the analysis the magnitude of reflection waves generating from the delamination. Various scenarios were examined, considering different delamination locations and sizes. Delamination was simulated by removing the tie constraint in the delamination region, which is positioned at 290 mm the edge from the excitation source along X_3 direction. A

reflection measurement point was defined at 50 mm ahead from the damage. The delamination was assumed to have a square shape with length of D mm.

Firstly, reflection waves were measured for delamination located at different layers. A delamination size of $D = 10$ mm was considered, which is commonly used in delamination detection studies [32]. An excitation frequency of 350 kHz was chosen for all three modes. At this frequency, the η value for all three modes is around 4. Mode 1 and Mode 2 have a wavelength of around 5mm, with Mode 2 having a slightly longer wavelength than Mode 1. Mode 3 has a wavelength around 20mm. Hence, the size of the damage is considerable, exceeding half of the wavelengths of all three wave modes. **Fig. 4.6** (b), (d) and (f) show typical screenshots illustrating the interaction of incident wave with the delamination located between the second and the third layers, corresponding to Mode1, Mode2, and Mode 3, respectively. The layers were systematically numbered, with the first layer being the closest layer to the measurement point. The figures show that the reflection wave components can contain both flexural and in-plane wave components, suggesting potential mode conversion at the delamination for both Mode 1 and Mode 3. Conversely, little to no reflection wave was observed for Mode 2, which has a dominated displacement in X_2 direction. The reflection ratios were calculated by dividing the magnitude of the reflection wave by that of the incident wave, and the results are presented in **Fig. 4.8** (a). The results indicate that the highest reflection ratios for both Mode 1 and Mode 3 occurred when the delamination is positioned between the first and second layers, resulting a reflection ratio around 0.4. As the delamination moves further from the measurement points, the reflection decreases, yielding reflection ratios ranging from 0.1 to 0.2 for both Mode 1 and Mode 3. Additionally, it was discovered that Mode 2 exhibits low sensitivity to delamination damage, with its reflection ratios remaining close to zero across all scenarios.

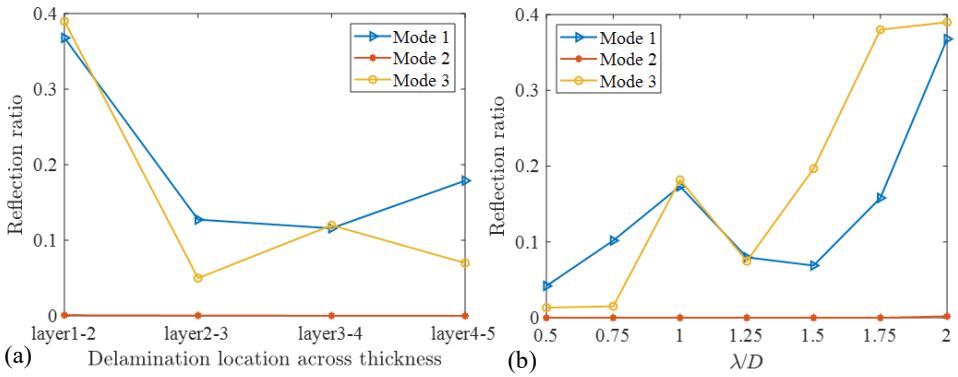

Fig. 4.8. Reflection ratio for (a) $D=10$mm edge delamination located at different layers across thickness, (b) varying delamination sizes located between the first and the second layers.

Furthermore, reflection ratios were determined for varying delamination sizes located between the first and second layers. The delamination length (D) is expressed in regard to the wavelength (λ) of each of the incident wave at an excitation frequency of 350 kHz. The reflection ratio was determined for D=0.5 λ to 2 λ with a step of 0.25 λ, and the results are shown in the **Fig. 4.8** (b). The results for both Mode 1 and Mode 3 show a similar pattern that the reflection ratio increases with increasing edge delamination size. However, a noticeable drop occurs at $\lambda/D = 1.25$, potentially attribute to interference among different reflection components. The reflection ratio of Mode 1 is larger than that of Mode 3 when λ/D is less than one wavelength, yet the reverse is observed when λ/D exceeds one wavelength, with Mode 3 displaying a greater reflection ratio.

4.4. Experiments

4.4.1. Experimental setup

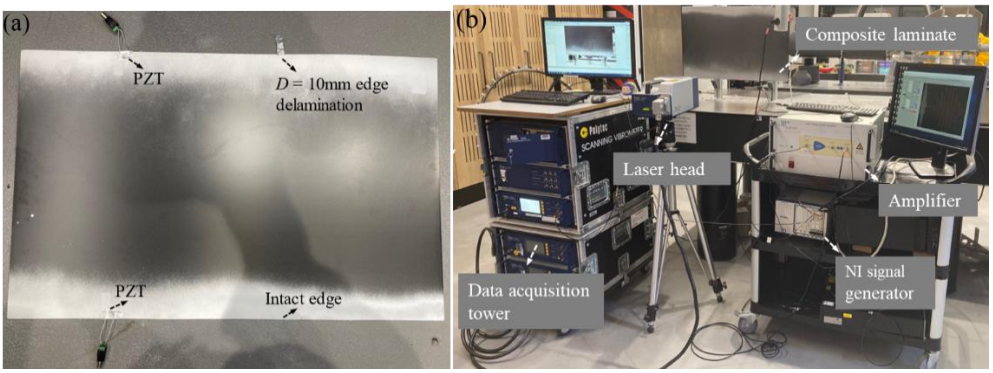

Fig. 4.9. Photograph of (a) the composite specimen and (b) experimental setup

Two identical composite laminates, each consisting of 8 plies of T300/M914 lamina with $[(0/90)_2]_s$ stacking sequence, were manufactured. These composite laminates have a thickness of 1.6mm. The dimensions of the specimens were 850mm in length and 500mm in width. During the manufacturing process, delamination damage with a size of D =10mm was created at one edge of both specimens. This was accomplished by inserting thin Teflon films between the second and third layers. The opposite edge of both specimens was left intact. Photographs of one of the specimens and the experimental setup are shown in **Fig. 4.9** (a) and (b), respectively. One specimen was employed to measure the reflection ratio of Mode 1, while the other was utilized to measure Mode 3. They were generated using different types of PZT. The excitation of Mode 2 requires displacements perpendicular to the edge. This was achieved by a PZT attached to the top surface of the edge [33] or by a transducer and a wedge clamped to the edge [25] in previous studies. However, it's worth noting that the specimens used in those studies were considerably thicker than the one in this study. It was found that performing both methods on the specimen proved unfeasible due to its thickness is much

smaller than the size of the PZT. Consequently, the experimental study focuses solely on the generation and measurement of Mode 1 and Mode 3.

Mode 1 was generated utilizing a surface-bonded rectangular 2 mm × 12 mm × 6 mm PZT (Ferroperm Pz27). Mode 3 was generated through a 10mm diameter and 0.5mm thick piezoceramic disc (Ferroperm Pz27). **Fig. 4.9** (b) shows the experimental setup. The signal was initially generated by NI signal module (PXIE-5122), and its voltage was amplified to 200 volts using a Ciprian amplifier before being directed to the PZT. The excitation signal for Mode a and Mode 3 was a 7-cycle narrow-band Hann windowed pulse with a centre frequency of 350 kHz. The out-of-plane displacement of the propagating waves were subsequently captured using a 1D laser Doppler vibrometer and fed into the data acquisition system. The sampling frequency was configured at 12.54 MHz with 500-sample averaging. Additionally, a low-pass filter gated at 800kHz was applied to enhance signal quality. Edges of the specimens were coated with aluminium base reflective paint (CRC) to improve the reflective properties.

4.4.2. Experimental results

Before commencing damage detection studies, the SAFE results were validated against the experiment results using a 2D-DFTmethod. Both Mode 1 and Mode 3 were validated by repeating the same process on the two specimens. A total of 30 measurement points, each spaced by 3mm, were defined along the wave propagation direction at the intact edge for both specimens. It was determined that the number of measurement points was sufficient to achieve good resolution in the space domain for the 2D-DFT contour. The measurement points were positioned as closed to the edge as possible because the energy concentration of the edge wave is highest at the edge. Out-of-plane displacements were recorded at these measurement points using the 1D laser Doppler vibrometer. The excitation center frequency was 350kHz for both

Mode 1 and Mode 3, which is the same as in FE study. The validation results obtained through 2D-DFT are shown in **Fig. 4.10** (a) for Mode 1 and **Fig. 4.10** (b) for Mode 3. The 2D-DFT results show good agreements between the experimental and the SAFE results, with only the incident waves being recorded at these measurement points.

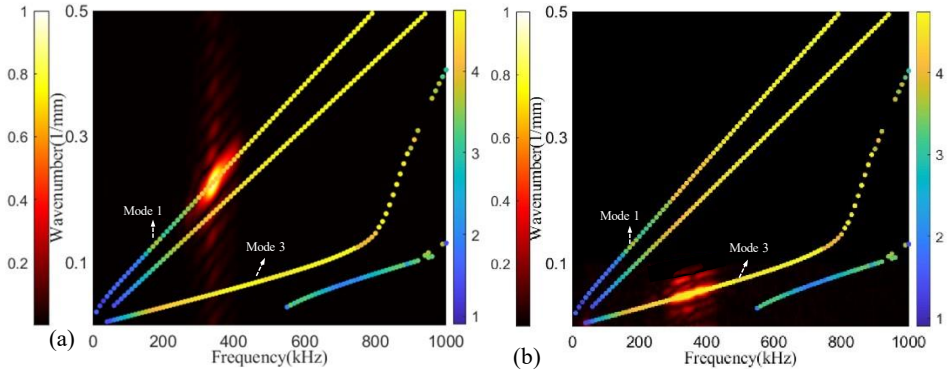

Fig. 4.10. Experimental 2D-DFT plot and the SAFE results for (a) Mode 1 and (b) Mode 3.

Group velocity of Mode 1 and Mode 3 at the interested frequencies were also measured using the time domain data collected at five measurements points along the wave propagation direction, each spaced by 3mm. The group velocity results are shown in **Fig. 4.11** (a) for excitation frequencies from 250 kHz to 450 kHz with a step of 20 kHz. The measurement procedure was replicated three times, and an error bar was used to illustrate the variation among different measurements. The experimental results were observed to closely matched the SAFE results, with a maximum variation of less than 12% between them. The minor discrepancy may be attributed to the small angle effect when scanning measurement points with the laser. Attenuation of Mode 1 and Mode 3 at 350 kHz were also measured at 19 measurements points located from 500mm to 590mm away from the excitation source. Since Mode 1 and Mode 3 were generated by different types of PZT on separate specimens, the amplifier voltage was calibrated for each measurement to ensure that the amplitudes of

Mode 1 and Mode 3 at the first measurement point were identical. The attenuation results are shown in **Fig. 4.11** (b), and both waves have the same amplitude of around 3×10^{-9} m at the first measurement point. It was found that Mode 3 decays faster than Mode 1 at the excitation frequency. While the leakage of Mode 3 can be one factor contributing to its faster decay of wave magnitude, material damping, and dispersive effects may also play a role. Notably, the group velocity curve of Mode 3 is not as flat as that of Mode 1 at the excitation frequency. Hence, Mode 3 can be more dispersive than Mode 1 at the excitation frequency.

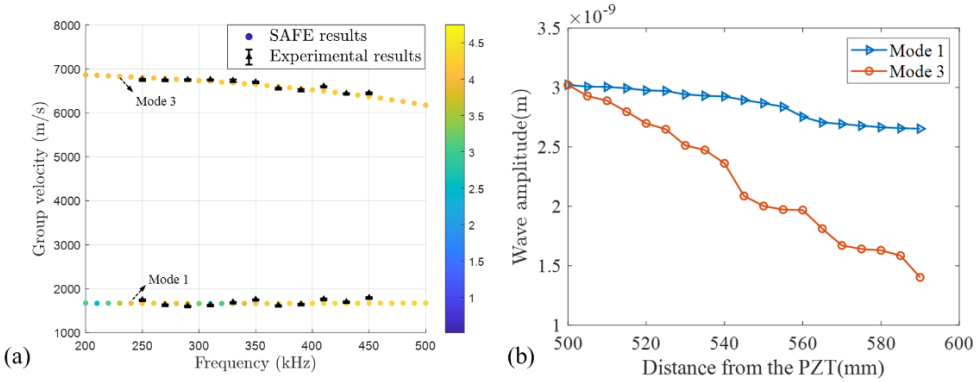

Fig. 4.11. (a) Experimental validation of group velocity for Mode1 and Mode 3. (b) Experimental attenuation results for Mode 1 and Mode 3 at 350kHz.

Reflection waves for both Mode1 and Mode 3 were measured at a reflection measurement point located 50mm ahead of the edge delamination damage. The excitation signal employed was a 7-cycle narrow-band Hann windowed pulse with a centre frequency of 350 kHz. The measurement location and the excitation signal were defined consistently with the FE study. The time-domain data measured at the reflection location for incident Mode 3 is shown in **Fig. 4.12**(a). The reflection ratios of Mode 1 and Mode 3 at the interested frequencies were obtained and are shown in **Fig. 4.12** (b). The arrival time of incident wave and reflection wave were accurately predicted by the FE simulation. Both experimental and FE results in **Fig. 4.12** (b) show an increasing trend in the reflection ratio as the frequency increases. However,

discrepancies in the magnitude and waveform of the reflection wave between two results are presented. The following factors can attribute to the observed discrepancies: 1) The delamination in the specimen was induced by pre-inserting thin Teflon films into the composite laminates. However, the FE model did not account for these thin Teflon films. 2) Although thin Teflon films were pre-inserted into the specimen, it's possible that during the resin curing process, weak bonding was partially formed at the delamination region. Consequently, the actual size of the delamination can be different to the designated size. The presence of delamination can be visually observed at the specimen's edge, although obtaining precise size of the delamination remains challenging.

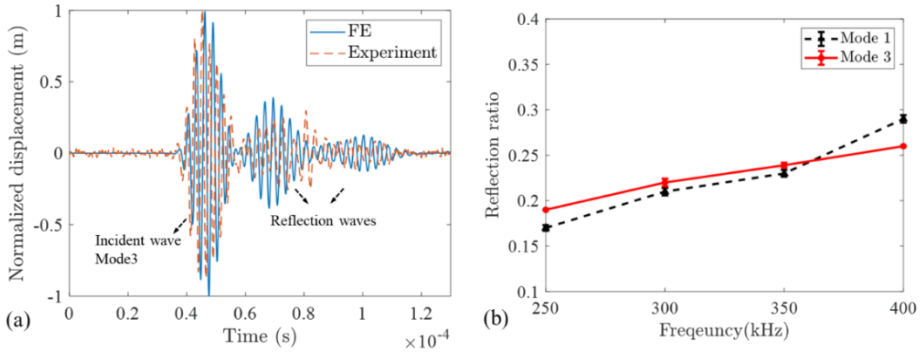

Fig. 4.12. (a) FE and experimental time domain data for an edge delamination damage of D = 10mm. (b) Reflection ratios of Mode 1 and Mode 3 at different frequencies

4.5. Conclusions

This study explored the feasibility of detecting edge delamination in a 1.6mm $[(0/90)_2]_s$ composite laminate using edge waves The existence of edge waves on the composite laminates was confirmed through modal studies using the SAFE-PML method. These edge waves can be distinguished from other modes due to their significant energy concentration at the plate edge. Three modes, labelled Mode 1 to Mode 3 in this study, were identified within the

calculated frequency ranges, and their modeshapes were investigated. Unlike edge waves in elastic materials, it was found that the energy distribution at the edges of the composite laminates can be greatly influenced by the stacking sequence of the laminae. In addition, a dispersion curve for edge waves in a composite laminate with $[0/45/90/-45]_s$ stacking sequence is also provided. It was found that in the $[0/45/90/-45]_s$ composite laminates, the dispersion curves of edge waves and plate waves exhibit substantial differences. Conversely, in the $[(0/90)_2]_s$ composite laminates, the dispersion curves of edge waves closely resemble those of plate waves.

Subsequently, the study assessed the feasibility of detecting edge delamination in the $[(0/90)_2]_s$ composite laminates for Mode 1 to Mode 3, using 3D FE analysis. The 3D FE analysis investigated the methods of wave excitation and the sensitivity of the wave to different sizes of edge delamination. The results indicated that Mode 1 and Mode 3 exhibited higher sensitivity compared to Mode 2 in detecting delamination. This can be due to the fact that Mode 1 and Mode 3 have a dominant displacement field in u_1 and u_3, whereas Mode 2 has a dominant displacement field in u_2 (shear direction to the plate). An experimental study was conducted to validate the dispersion curves obtained through the SAFE method. Furthermore, a damage detection experiment was carried out to identify edge delamination using Mode 1 and Mode 3 under a pulse-echo configuration. The findings in this study have provided a deeper understanding of the behaviour of edge waves in composite laminates and have demonstrated great potential for damage detection applications in composite laminate using edge waves.

4.6. CRediT authorship contribution statement

Jinhang Wu: Conceptualization, Methodology, Writing – original draft. **Chang Jiang**: Methodology, Advising, Writing – original draft. **Ching Tai Ng**: Supervision, Writing – review & editing. **Han Fang**: Supervision, Advising

4.7. Declaration of Competing Interest

The authors declare no conflict of interest.

4.8. Data availability

Data will be made available on request.

4.9. Acknowledgement

This work was funded by the Australian Research Council (ARC) under grant number DP210103307 and LP210100415. The authors are grateful for this support.

4.10. Appendix A. Edge waves in a quasi-isotropic composite laminate

A common $[0/45/90/-45]_s$ quasi-isotropic composite laminate is modelled. The model remains consistent with the one shown in **Fig. 4.1**, except for the application of different stacking sequence to the laminae as required. The same filtering algorithm was applied to the model. **Fig. 4.13** (a) shows the filtered wavenumber solutions, revealing the presence of ES_0 (labelled as Mode 4) near the SH_0 dispersion curve. However, substantial disparities are noticeable in their dispersion curves, and EA_0 is notably absent. Other modes have been identified, however their η values are significantly lower than that of ES_0, and they exhibit more substantial attenuation as shown in **Fig. 4.13** (b). A typical modeshapes of ES_0 at 400 kHz is given in **Fig. 4.13** (c). When compared to the modeshapes shown in **Fig. 4.4** (b) (i.e., ES_0 at 400 kHz in a composite with $[(0/90)_2]_s$ stacking sequence), it's observed that this mode exhibits a larger u_1

component at the edge tip. In summary, it is concluded that the stacking sequence of the laminae can significantly influence the dispersion characteristics of edge waves. As shown in **Fig. 4.13** (a), the dispersion curve of ES_0 notably deviates from SH_0, which differs from previous results in **Fig. 4.2** (a).

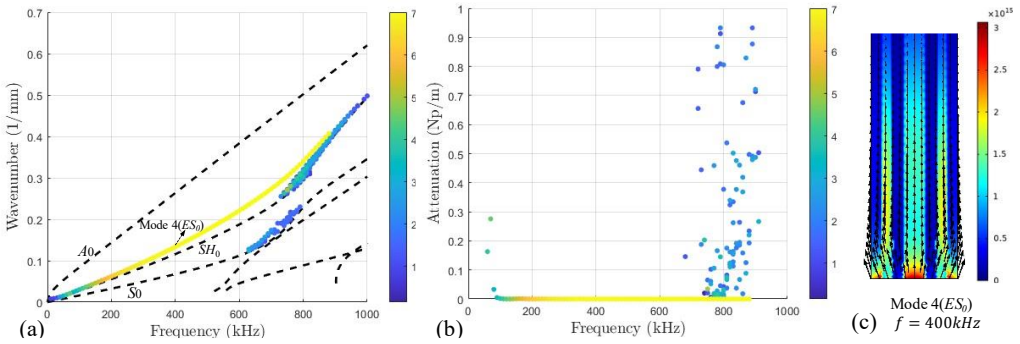

Fig. 4.13. Dispersion curves for a 1.6mm [0/45/90/-45]s T300/M914 composite laminate along 0° direction (scatter plot: edge waves calculated from SAFE, line plot: Lamb and shear horizontal modes) (a) frequency-wavenumber, (b) frequency-attenuation, (c) modeshapes of Mode 4. Colour bar and arrows have the same meaning as **Fig. 4.3**.

4.11. References

1. Allen, J.C.P. and C.T. Ng, *Damage detection in composite laminates using nonlinear guided wave mixing.* Composite Structures, 2023. **311**: p. 116805.
2. Mittelstedt, C., et al., *Free-edge effects in composite laminates—A review of recent developments 2005–2020.* Applied Mechanics Reviews, 2022. **74**(1): p. 010801.
3. Malhotra, A., F. Guild, and M. Pavier, *Edge impact to composite laminates: experiments and simulations.* Journal of materials science, 2008. **43**: p. 6661-6667.
4. Hervin, F., L. Maio, and P. Fromme, *Guided wave scattering at a delamination in a quasi-isotropic composite laminate: Experiment and simulation.* Composite Structures, 2021. **275**: p. 114406.

5. Munian, R.K., D.R. Mahapatra, and S. Gopalakrishnan, *Ultrasonic guided wave scattering due to delamination in curved composite structures.* Composite Structures, 2020. **239**: p. 111987.
6. Zhang, H., et al., *Delamination damage imaging method of CFRP composite laminate plates based on the sensitive guided wave mode.* Composite Structures, 2023. **306**: p. 116571.
7. Sohn, H., et al., *Delamination detection in composites through guided wave field image processing.* Composites science and technology, 2011. **71**(9): p. 1250-1256.
8. Soleimanpour, R., C.-T. Ng, and C.H. Wang, *Higher harmonic generation of guided waves at delaminations in laminated composite beams.* Structural Health Monitoring, 2017. **16**(4): p. 400-417.
9. Soleimanpour, R. and C.-T. Ng, *Locating delaminations in laminated composite beams using nonlinear guided waves.* Engineering Structures, 2017. **131**: p. 207-219.
10. Su, Z., L. Ye, and Y. Lu, *Guided Lamb waves for identification of damage in composite structures: A review.* Journal of sound and vibration, 2006. **295**(3-5): p. 753-780.
11. Lawrie, J.B. and J. Kaplunov, *Edge waves and resonance on elastic structures: An overview.* Mathematics and Mechanics of solids, 2012. **17**(1): p. 4-16.
12. Krushynska, A., *Flexural edge waves in semi-infinite elastic plates.* Journal of Sound and Vibration, 2011. **330**(9): p. 1964-1976.
13. Zernov, V. and J. Kaplunov, *Three-dimensional edge waves in plates.* Proceedings of the Royal Society A: Mathematical, Physical and Engineering Sciences, 2008. **464**(2090): p. 301-318.
14. Rekatsinas, C., N. Chrysochoidis, and D. Saravanos, *Investigation of critical delamination characteristics in composite plates combining cubic spline piezo-layerwise mechanics and time domain spectral finite elements.* Wave Motion, 2021. **106**: p. 102752.
15. Lonkar, K. and F.-K. Chang, *Modeling of piezo-induced ultrasonic wave propagation in composite structures using layered solid spectral element.* Structural Health Monitoring, 2014. **13**(1): p. 50-67.
16. Li, F., et al., *Wave propagation analysis in composite laminates containing a delamination using a three-dimensional spectral element method.* Mathematical Problems in Engineering, 2012. **2012**.
17. Zuo, P. and Z. Fan, *Modal properties of elastic surface waves in the presence of material anisotropy and prestress.* Journal of Sound and Vibration, 2020. **485**: p. 115588.
18. Zhu, H., C.T. Ng, and A. Kotousov, *Fatigue crack detection in edges of thin-walled structures with corners using the fundamental mode of edge waves.* Ultrasonics, 2023. **132**: p. 106995.
19. Yu, X., R. Qin, and M. Deng, *New insights into topographically feature guided waves (FGW) propagation in non-uniform elastic waveguides.* Wave Motion, 2022. **109**: p. 102866.

20. Corcoran, J., et al., *A guided wave inspection technique for wedge features.* IEEE Transactions on Ultrasonics, Ferroelectrics, and Frequency Control, 2019. **67**(5): p. 997-1008.
21. Hughes, J.M., et al., *The fundamental ultrasonic edge wave mode: Propagation characteristics and potential for distant damage detection.* Ultrasonics, 2021. **114**: p. 106369.
22. Chu, J.Y.H. and C.R. Courtney, *The detection of impact damage to the edges of CFRP plates using extensional ultrasonic edge waves.* Journal of Nondestructive Evaluation, 2021. **40**(4): p. 88.
23. *COMSOL, User's Guide and Introduction, COMSOL MULTIPHYSICS,*. Available from: http://www.comsol.com/.
24. Zuo, P. and Z. Fan, *SAFE-PML approach for modal study of waveguides with arbitrary cross sections immersed in inviscid fluid.* Journal of Sound and Vibration, 2017. **406**: p. 181-196.
25. Hughes, J.M., et al., *Damage detection with the fundamental mode of edge waves.* Structural Health Monitoring, 2021. **20**(1): p. 74-83.
26. Wilde, M.V., M.V. Golub, and A.A. Eremin, *Experimental observation of theoretically predicted spectrum of edge waves in a thick elastic plate with facets.* Ultrasonics, 2019. **98**: p. 88-93.
27. Yu, X., et al., *Feature guided wave inspection of bond line defects between a stiffener and a composite plate.* NDT & E International, 2017. **89**: p. 44-55.
28. Wu, J., et al., *Damage detection in the T-welded joint using Rayleigh-like feature guided wave.* NDT & E International, 2023. **135**: p. 102806.
29. Fan, Z. and M. Lowe, *Interaction of weld-guided waves with defects.* NDT & E International, 2012. **47**: p. 124-133.
30. Yu, X., et al., *Shear horizontal feature guided ultrasonic waves in plate structures with 90 transverse bends.* Ultrasonics, 2016. **65**: p. 370-379.
31. Rajagopal, P., et al., *On the use of absorbing layers to simulate the propagation of elastic waves in unbounded isotropic media using commercially available finite element packages.* Ndt & e international, 2012. **51**: p. 30-40.
32. Ng, C.-T. and M. Veidt, *Scattering of the fundamental anti-symmetric Lamb wave at delaminations in composite laminates.* The Journal of the Acoustical Society of America, 2011. **129**(3): p. 1288-1296.
33. Vien, B.S., L.R.F. Rose, and W.K. Chiu, *Experimental and computational studies on the scattering of an edge-guided wave by a hidden crack on a racecourse shaped hole.* Materials, 2017. **10**(7): p. 732.

5. Conclusions

5.1. Summary and Contributions

This thesis has investigated the damage detection capabilities of guided waves (GWs) in structural elements that present challenges in detection, including those containing specific structural features or exhibiting material anisotropy. The study systematically explores the wave modes existing in these structural features and investigates GW propagation characteristics in commonly used anisotropic materials like timber and composite laminates. In Chapter 1, fundamental concepts related to GW-based damage detection are introduced. The significance of GW methods in structural health monitoring is highlighted. The chapter includes literature reviews summarizing challenges of GW damage detection in structural elements containing irregular features or exhibiting material anisotropy.

In Chapter 2 (paper 1), this thesis focuses on GWs in a steel T-welded joint. A Rayleigh-like feature guided wave (FGW) has been identified propagating along the T-welded joint. The energy of this wave is notably concentrated around the joint areas, allowing it to travel extended along the joint with little attenuation. This characteristic makes it potentially valuable for the inspection of common weld defects along T-welded joints. To distinguish this FGW from other modal solutions, a novel filtering algorithm has been introduced. This algorithm takes into consideration both the concentration of energy and the attenuation of the wave. The high sensitivity of this identified FGW for detecting typical weld cracks is exemplified by the high amplitudes of reflection waves from the weld cracks, which have been experimentally validated. The proposed study paves the way for monitoring weld defects along T-welded joints using GWs.

From Chapter 3 (paper 2) onwards, this thesis focuses on GWs in anisotropic structural elements, including those containing structural features. In Chapter 3, GWs have been proposed for detecting internal damage in a structural timber member. The timber member is modelled as a transversely isotropic material, showing good agreement with the results of a verified experiment. The excitation frequency is chosen so that the wavelength of the incident wave is larger than minor natural defects like cracks but comparable to the size of internal damage. The proposed study revealed that low-frequency fundamental anti-symmetric modes show good potential for damage detection in timber members, offering long propagation distances and good sensitivity compared to conventional timber inspection methods such as bulk wave methods.

In Chapter 4 (paper 3), the thesis delves into the study of edge waves propagating along the edges of anisotropic composite laminates. The study investigates the dispersion relations of edge waves on composite laminates with different stacking sequences. Numerical results are used to compare the displacement fields and mode shapes between the edge waves at the edges of composite laminates and those in isotropic materials. It is found that the fibre direction substantially affects the energy concentration of in-plane dominated wave modes but has relatively minor effects on out-of-plane dominated wave modes. Furthermore, the study explores the sensitivity of identified edge waves in detecting typical edge delamination in composite laminates. The results enhance the understanding of edge wave behaviours in anisotropic edges, specifically the edges of composite laminates.

In summary, this thesis has explored the potentials of GWs in structural elements containing structural features and material anisotropy. The research demonstrates that the GW techniques can effectively detect typical damages within these structures, including weld defects in T-welded joints, internal damages in timber, and edge delamination of composite laminates.

5.2. Recommendations

This thesis explores GWs in structural elements possesses typical structural features or material anisotropy. The recommendations for future work are outlined below.

1. The proposed FGW study on a T-welded joint focuses on linear wave characteristics. Future research could extend this study to explore the nonlinear wave phenomena of FGWs, such as the material nonlinearity induced by cycled fatigue loadings. Utilizing nonlinear techniques not only enables the detection of early degradation in material properties but also eliminates the need for baseline signal data.

2. In real-world scenarios, T-weld joints can be subjected to prestress conditions. To address this, further studies can investigate the behaviour of FGWs in T-weld joints under the influence of acoustoelastic effects.

3. Structural timber elements often have thicker dimensions than the specimens used in the presented study. Rayleigh surface waves are deemed more suitable for damage detection in thick objects. Exploring the propagation characteristics of Rayleigh surface waves in thick timber members could be valuable for future research

4. Timber can obtain natural malformations such as annual growth rings, knots, and cracks. These defects can be sources to generate reflection waves. To address the high variability in timber damage detection, combining GW techniques with machine learning approaches in future studies could be beneficial.

5. The material properties of timber are moisture-dependent, which can affect wave parameters such as attenuation and wave speeds. Further research can investigate the effects of moisture on these parameters. Additionally, numerical studies can be developed to simulate material damping for timber under different moisture conditions.
6. For edge waves propagates in composite laminates, further study is recommended to investigate the nonlinear edge wave phenomena. Studies such as contact acoustic nonlinearity at edge delamination with an incident wave of antisymmetric edge modes could provide valuable insights.